

AD A169281

LEVEL

(9)

Contract N00019-79-C-0347

103-077

IMPACT RESPONSE CHARACTERISTICS OF POLYMERIC MATERIALS

W.B. Hillig
Corporate Research and Development
General Electric Company
Schenectady, N.Y. 12301

DTIC
SELECTE
JAN 6 1982
H
D

(12) 98

November 1981

Final Report for Period 27 April 1979 to 30 April 1981

Approved for Public Release -- Distribution Unlimited

Prepared for
NAVAL AIR SYSTEMS COMMAND
Department of the Navy
Washington, D.C. 20361

406 617

SRD-81-081

82 01 04 024

(8)

Unclassified

SECURITY CLASSIFICATION OF THIS PAGE (When Data Entered)

REPORT DOCUMENTATION PAGE		READ INSTRUCTIONS BEFORE COMPLETING FORM
1. REPORT NUMBER AD- A109281	2. GOVT ACCESSION NO.	3. RECIPIENT'S CATALOG NUMBER
4. TITLE (and Subtitle) Dynamic Impact Response Behavior of Polymeric Materials (III)		5. TYPE OF REPORT & PERIOD COVERED Final Report 79 April 27 to 80 April 30
		6. PERFORMING ORG. REPORT NUMBER SRD-81-081 ✓
7. AUTHOR(s) William B. Hillig		8. CONTRACT OR GRANT NUMBER(s) N00019-79-C-0347 <i>new</i> 7
9. PERFORMING ORGANIZATION NAME AND ADDRESS General Electric Company Corporate Research and Development P.O. Box 8, Schenectady, NY 12301		10. PROGRAM ELEMENT, PROJECT, TASK AREA & WORK UNIT NUMBERS
11. CONTROLLING OFFICE NAME AND ADDRESS Commander Naval Air Systems Command AIR-5163D4 Washington, DC 20361		12. REPORT DATE November 1981
		13. NUMBER OF PAGES 83
14. MONITORING AGENCY NAME & ADDRESS (if different from Controlling Office)		15. SECURITY CLASS. (of this report) Unclassified
		15a. DECLASSIFICATION/DOWNGRADING SCHEDULE
16. DISTRIBUTION STATEMENT (of this Report) Approved for Public Release - Distribution Unlimited		
17. DISTRIBUTION STATEMENT (of the abstract entered in Block 20, if different from Report) DTIC JAN 6 1982 D		
18. SUPPLEMENTARY NOTES H		
19. KEY WORDS (Continue on reverse side if necessary and identify by block number) Hopkinson Bar, Ballistic Impact, Impact Damage of Polymer, Relaxation of Polymers		
20. ABSTRACT (Continue on reverse side if necessary and identify by block number) This report describes the concluding work on a series of studies concerned with determining, understanding, and trying to predict the behavior of polymethylmethacrylate (PMMA) and polycarbonate (PC) under impact. In the present work the impact velocity was extended to 2.1, 125, and 220 m/s using a 4.5 mm steel ball as the projectile. Because of dispersion effects the pulse detected using an instrumented Hopkinson impact bar was markedly distorted. A new semi-empirical procedure for correcting the pulse was developed that overcame difficulties encountered in the theoretical methods.		

DD FORM 1 JAN 73 1473

EDITION OF 1 NOV 65 IS OBSOLETE

Unclassified

SECURITY CLASSIFICATION OF THIS PAGE (When Data Entered)

Unclassified

SECURITY CLASSIFICATION OF THIS PAGE(When Data Entered)

Analysis of the data showed that the deduced Young's modulus of PMMA slowly increases with increasing impact velocity. However, the derived modulus of PC decreases by a factor of five when the impact velocity was increased from 2.1 to 220 m/s. This decrease in stiffness is unexpected and anomalous, but is beneficial to reducing the potential for impact damage. A theoretically-based model was formulated to "predict" the impact response of the two materials from their elastic modulus, densification properties, and stress-relaxation laws. This modified spring/dashpot model allows the response of the polymers to be continuously varied between series-like and parallel-like. The PMMA was found to require a predominantly series-like mode description, whereas the PC response was more parallel-like. The instrumented Hopkinson impact bar method and analysis procedures have now been developed to the point where they could be extended to a much wider range of polymers and impact conditions to yield scientifically interesting and technologically useful information about polymer behavior under concentrated, rapidly applied loads.

Unclassified

SECURITY CLASSIFICATION OF THIS PAGE(When Data Entered)

ABSTRACT

This report describes the concluding work on a series of studies concerned with determining, understanding, and trying to predict the behavior of polymethylmethacrylate (PMMA) and polycarbonate (PC) under impact. In the present work the impact velocity was extended to 2.1, 125, and 220 m/s using a 4.5 mm steel ball as the projectile. Because of dispersion effects the pulse detected using an instrumented Hopkinson impact bar was markedly distorted. A new semi-empirical procedure for correcting the pulse was developed that overcame difficulties encountered in the theoretical methods. Analysis of the data showed that the deduced Young's modulus of PMMA slowly increases with increasing impact velocity. However, the derived modulus of PC decreases by a factor of five when the impact velocity was increased from 2.1 to 220 m/s. This decrease in stiffness is unexpected and anomalous, but is beneficial to reducing the potential for impact damage. A theoretically-based model was formulated to "predict" the impact response of the two materials from their elastic modulus, densification properties, and stress-relaxation laws. This modified spring/dashpot model allows the response of the polymers to be continuously varied between series-like and parallel-like. The PMMA was found to require a predominantly series-like mode description, whereas the PC response was more parallel-like. The instrumented Hopkinson impact bar method and analysis procedures have now been developed to the point where they could be extended to a much wider range of polymers and impact conditions, to yield scientifically interesting and technologically useful information about polymer behavior under concentrated, rapidly applied loads.

Accession For	
NTIS GRA&I	<input checked="checked" type="checkbox"/>
DTIC TAB	<input type="checkbox"/>
Unannounced	<input type="checkbox"/>
Justification	
By	
Distribution/	
Availability Codes	
1 2 3 4 5 6 7 8 9 10	
A	

SUMMARY

This work concludes a series of studies on the impact response of two representative polymers: polymethylmethacrylate (PMMA) and polycarbonate (PC). The goals of this present effort were (1) to measure the impact pulse produced when these polymers are struck at velocities up to the highest value feasible using a compressed gas gun, (2) to develop a means of analyzing that pulse data so as to reveal the response of the material to the impact, and (3) to develop a model of the expected response derived from other basic property information.

An instrumented Hopkinson impact bar was used to detect the impact force as a function of time. Careful consideration and study was given to the selection of the bar material and geometry. Poor acoustic matching with the specimen can result in multiple reflections at the test specimen/bar interface which confuse and delay the signal as it enters the bar. Also the dependence of sound velocity on frequency (dispersion) in the bar material can markedly distort the measured signal. After several trials, PMMA was selected as the best compromise bar material. Digitally recorded signals were obtained of the pulses produced by impacts of a 4.5 mm steel ball against PC and PMMA targets at velocities of nominally 2.1, 125, and 220 m/s. Reproducibility between replicate experiments was excellent.

The pulse data required computational processing because of the distortion due to dispersion. The theoretical techniques for doing this were inadequate. Identification of the first arrival of the impact signal at the sensor, and some basis for defining its initial shape, are essential to translating the pulse information into such terms as the reaction force versus penetration depth. Several attacks were made to solve the mathematically difficult problem of computing the change in shape of the leading edge of a pulse as it travels down the bar. A semi-empirical, semi-theoretical solution was found by careful examination of the data. Using this procedure, the experimental pulses were corrected for distortion, and the materials response could be computed.

The results showed that PMMA behaves much as expected on the basis of our prior work at much smaller penetration velocities. The derived apparent Young's modulus increased perceptibly with increasing impact velocity being 3.6, 4.25, and 4.4 GPa at 2.1, 127, and 219 m/s impact velocities, respectively. In contrast PC behaved anomalously, having computed modulus values of 1.4, 0.4, and 0.3 at 2.1, 125, and 221 m/s, respectively. The decrease in modulus with increasing velocity is contrary to usual theoretical expectation and reverses the trend observed in our prior work at lower penetration velocities. Whereas PMMA first developed radial cracks at the highest impact velocities, PC remained visibly undamaged except for the impact crater.

A theoretical visco-elastic model was produced for "predicting" the impact pulse from the Young's modulus, the densification volume ratios, and the stress relaxation parameters. The model also provides for a continuously variable material behavior ranging from a series-like to a parallel-like coupling between the elastic and viscous components of a spring/dashpot representation. The calculated pulse for the PMMA material could be made to approximate the experimental response by considering this material to behave in a series-like manner. The calculated pulse for PC suggested a more nearly parallel-like behavior, but could not be made to fit the experimental results without varying the type of behavior during the course of the impact. This model is suggestive of the important parameters affecting the impact response. However, it contains many approximations and requires critical testing.

TABLE OF CONTENTS

Section	Page
1. INTRODUCTION.....	1
1.1 Review of Prior Work	1
1.1.1 Prior Work Using Mechanical Test Machines.....	2
1.1.2 Prior Work Using the Instrumented Impact Bar Methods ..	5
1.2 Objectives of the Present Study	7
2. OVERVIEW OF PRESENT WORK	9
2.1 Correction of Pulse Shapes Using Transfer Functions	9
2.2 Theoretical Studies of the Behavior of the Pulse Leading Edge	10
2.3 Impact Bar Dispersion and Acoustic Impedance Matching Considerations	11
2.4 Experimental Impact Measurements	12
2.5 Analysis of Experimental Results.....	12
2.6 Semi-Empirical Approach to Pulse Shape Correction	13
2.7 Derived Material Response Behavior	14
2.8 Modelling of the Material Behavior	14
3. MATERIALS AND SPECIMEN PREPARATION	15
3.1 Polymethylmethacrylate	15
3.2 Polycarbonate	15
3.3 Inorganic Glass	15
3.4 Silicon Carbide	15
4. IMPACT BAR STUDIES	16
4.1 Impact Measurements Using Vitreous Silica Bar	16
4.2 Use of Vitreous Silica as a Striker	17
4.3 Impact Measurements Using the PMMA Bar	17
5. CORRECTION OF IMPACT PULSE DATA FOR DISPERSION	18
5.1 Detection and Characterization of the Leading Edge	18
5.1.1 Vitreous Silica Bars	18
5.1.2 PMAA Impact Bar	18
5.1.2.1 Vitreous Silica Bar Collision with PMMA Bar	18
5.1.2.2 Pendulum Impacts.....	19
5.1.2.3 Gas Gun Projectile Impacts	19
5.2 Propagation Velocity	19
5.3 Analytical Representation of Overall Pulse	20
5.4 Pulse Correction Methodology	21
5.4.1 Conceptual Basis	21
5.4.2 Operational Procedure.....	23
5.5 Results of Pulse Correction Procedure.....	25

TABLE OF CONTENTS (Cont'd)

6.	DERIVED RESPONSE OF PMMA AND PC TO FREE FLIGHT IMPACTS	28
	6.1 Analysis of PMMA Data	28
	6.2 Analysis of PC Data	29
	6.3 Discussion of Results	30
7.	VISCO-ELASTIC MODEL OF POLYMER IMPACT BEHAVIOR	31
	7.1 Details of the Model	31
	7.2 The Time Dependence of the Fluidity	33
	7.3 Discussion of Input Data and Procedure	35
	7.4 Computational Results	36
8.	DISCUSSION AND CONCLUSIONS	38
	8.1 Discussion of Measurement and Analysis Procedures	38
	8.2 Discussion of the PC and PMMA Results	39
	8.3 Results of Model Calculations	39
9.	ACKNOWLEDGMENT	41
10.	REFERENCES	42
11.	APPENDIX	43
	11.1 Conversion of Impact Pulse Data into Force-Time and Energy-Time Relationships	43

1. INTRODUCTION

The response of a structural polymer to a concentrated load such as a potentially damaging impact hit is both practically and technically important. This report represents the conclusion of a series of studies of the various phenomena that result from impact encounters of polymers with small hard bodies. The long term goal has been to gain scientific understanding which in turn can contribute to: (1) the evolution of polymers having improved impact resistance, (2) the diagnosis of impact-related failure, and (3) improved techniques or criteria for characterizing materials with respect to their impact resistance.

The approach has been to study impact under conditions that closely resemble normal experience while at the same time trying to simplify and idealize the experiments so as to facilitate fundamentally meaningful measurements, analyses and modelling of the material processes occurring at the site of the impact. Accordingly the conceptual ideal has been the impact of hard spheres against the free surface of a well-characterized semi-infinite polymeric solid. To approximate this ideal we have focussed on two widely studied standard commercial structural polymers, viz. polycarbonate (PC), and polymethylmethacrylate (PMMA). Thick specimens of these materials have been used to simulate the semi-infinite aspects, and the hard spheres consisted of steel ball bearings.

In our preceding studies⁽¹⁻⁶⁾ these materials have been investigated at impact velocities ranging over 9 1/2 decades from 0.08 $\mu\text{m/s}$ to 220 m/s. Covering such a velocity span has required several kinds of instrumentation. Part of our challenge has been to establish concordance between the various measurement methods. Mechanical test machines using conventional load cells to measure the reaction force were convenient for penetration at constant velocity. At the other extreme free flight ballistic impacts were achieved using a compressed gas gun to propel the projectile. The material response in this case is sensed from the sonic impact pulse imparted to a Hopkinson impact bar. Translating the pulse information into materials response information is much more complicated in the case of free flight impacts than for the case of slow encounters using mechanical test machines. The experimental work of the present concluding study has been devoted to the impact bar measurements over the velocity range 2.1 to 220 m/s.

Throughout this series the observations of greatest interest have included (1) the material reaction force as a function of penetration depth and time, (2) the stress relaxation and strain recovery processes occurring during and upon halting the penetration, (3) the relative contributions to the deformation processes by elastic, anelastic, and viscous responses, (4) densification beneath the indentation crater, and (5) cracking. Finally, a technical objective has been to synthesize a model that "explains" the impact response in basic terms that reflect structural transformation and transport processes in the polymers.

Because this report is the final one in this series, a somewhat extended review of the prior work is included to provide perspective of the long range technical goals, challenges, and concerns as well as of the major accomplishments, conclusions, and insights. This review also provides a background for the present studies.

1.1 Review of Prior Work

Originally we expected PC and PMMA to behave like linear visco-elastic materials at small strains. Later, our experimental results indicated either that linear visco-elasticity model does not apply, or that its range of usefulness is imperceptively nar-

row. Other results indicated a much richer set of phenomena are involved. At the start the work was done mainly by driving the spherical bodies into the polymers at constant speed over the velocity range accessible through the use of screw-driven and hydraulic mechanical test machines. This was followed by a completely different kind of measurement technique in which the spheres were propelled against the polymers and the response measurements were made using Hopkinson impact bar methods. This introduced an entirely new set of problems that had to be overcome.

1.1.1 Prior Work Using Mechanical Test Machines

The linear visco-elastic extension of the classical Hertz analysis for the pressing of spherical elastic bodies into other elastic bodies, provides a framework for modelling the early stages of the indentation/impact process. The Hertz elastic analysis gives the following relationship for the dependence of the penetration depth x on the applied force P :

$$P = [4E_0\sqrt{R}/3(1 - \nu^2)]x^{3/2} \quad (\text{Eq. 1.1})$$

$$= K_0x^{3/2}$$

where E_0 is Young's modulus, R is the radius of the sphere, ν is the Poisson ratio, and K_0 is the quantity in brackets. If the material is linearly visco-elastic it is convenient to introduce the concept of the relaxation modulus $E(t)$ defined as the stress (at time t) divided by a fixed strain applied instantaneously at $t = 0$. For such a material the equation corresponding to Eq. 1 is:

$$P(t) = \frac{K_0}{E_0} \int_0^t E(t - t') \frac{dx^{3/2}}{dt'} dt' \quad (\text{Eq. 1.2})$$

Note that if $E(t)$ is time independent, then $E(t) = E_0$, so that the two equations are identical. It is possible to invert Eq. 2 by the method of Laplace transforms as discussed in Ref. 1, to compute $E(t)$. At constant penetration velocity u , time can be replaced by x/u . In order to compute $E(t)$, the force must be measured as a function of x and preferable expressed analytically in terms that are convenient for Laplace transformation. The following form was found⁽²⁾ to describe the data very well both at small and large penetration depths.

$$P(x) = K_0x^{3/2}\phi(x) \quad (\text{Eq. 1.3})$$

where

$$\phi(x) = [1 + Ax + B_1e^{-c_1x} + B_2(1 + \alpha x)e^{-c_2x}] / (1 + B_1 + B_2) \quad (\text{Eq. 1.4})$$

in which the various constants are to be determined from experimental data. The justification for assuming linear visco-elasticity derived from the fact that the elastic Hertz analysis shows that under a ball, although the load is concentrated, the stress is initially infinitesimal.

In order to be relevant to impacts at high velocity, it is necessary to determine $E(t)$ for times as short as about $1 \mu\text{s}$. This implies that the load $P(t)$ must reach a sensible level in this time interval, but this was not possible using the screw-driven mechanical test machines. However, because the force-penetration behavior was not strongly velocity dependent, it seemed possible that the short time behavior could be deduced by

extrapolation from the data for longer times. Accordingly, measurements were made over as wide a range of indentation velocities as practicable. An electro-hydraulic test machine^(2,3) extended the velocity maximum to about 2.5 m/s allowing data to be obtained over a 7 1/2 decade range of velocity.

For penetration depths greater than about 1/10 of the sphere radius, the observed force increased essentially linearly with depth in all cases. Over this wide range of penetration velocities there was a 150% increase in slope for the PMMA material but less than half of this increase for PC. In fact for the latter material the slope was virtually constant for velocities between 8 $\mu\text{m/s}$ and 800 $\mu\text{m/s}$. Slope is related to stiffness and is a measure of $E(t)$ behavior.

The premise of this preceding work was that these results could define an effective relaxation modulus. The term "effective" is used because by extending the computation into the range of large penetration depths, the visco-elasticity might not remain linear. Nevertheless this $E(t)$ function would not only serve as a useful characterization of the polymer but might be used to predict the impact response.

The variation of stiffness with increasing penetration rate is qualitatively consistent with the general behavior of relaxation moduli, which are monotonically decreasing functions of time, i.e., the shorter the time, the stiffer the material response. However, the absolute magnitude of the stiffness was several-fold less than that computed from ultrasonic measurements of the elastic modulus of PC and PMMA. Hence, with increasing penetration velocity the stiffness was expected to increase to a level consistent with the sonic results. However, unless the velocity dependence increased markedly, the measurements suggested that this would require many more decades increase of velocity.

It gradually became clear that the relaxation modulus approach was inadequate. First, there was no penetration range in which linear visco-elastic behavior was experimentally evident. Second, even with wide range of experimental data, no clear limiting trends with further increase in velocity could be detected in the various parameters in the $\phi(x)$ function which suggest how they would behave as time approached zero. Third, the specimens after and during the penetration process displayed a sharply defined "frozen-in" densified zone that develops at the site of the impact. This zone remains on unloading. However, both the zone, and the indentation crater disappear when the polymers are heated to their glass-transition temperatures. Hence, the flow that occurs during the indentation process retains a memory. This behavior lies outside of the scope of a simple visco-elastic model. Finally, when the rate of penetration was abruptly changed, unusual history-dependent transient responses were observed. The rate constants for the transients were found to be very nearly proportional to the penetration velocity just prior to stopping the indenter. For example, if the penetration was abruptly stopped, the rate of load relaxation was found to be proportional to the velocity at which the penetration had been produced. Thus, the reason for the apparent insensitivity of the force-penetration behavior to velocity during the constant penetration velocity experiments was apparently not that the polymer was strain-rate insensitive. Rather, there was an underlying marked strain-rate sensitivity which was masked by the simultaneous, nearly compensating stress-relaxation.^(3,4)

The observed densification⁽³⁾ was about 0.2% for the case of PMMA, and manifested itself as an optically distinct, spheroidal region having somewhat the appearance of a glass bead embedded in the polymer. The major diameter of the region was approximately coincident with the bottom of the spherical indentation. The volume of the

"disturbed" zone is about 6.2 times the volume displaced by the indenter in the case of PC, and about 3.6 times the volume for PMMA. Interpreting this zone formation as plastic yielding lead to an estimated yield strain of about 0.08 and 0.05 for PMMA and PC, respectively, corresponding to yield stress of about 200 MPa (29 KSI) for both materials. However, other estimates lead to lower yield strains and stresses. By following the formation of the disturbed zone in PC using motion pictures, it was found that the zone develops almost from the first instant of contact.

Load relaxation as well as creep-recovery were studied at several penetration rates, and penetration depths for both polymers. The load relaxation was found⁽³⁾ to obey a law having the unusual form:

$$P(t) = P(0)(1 + At)^{-B} \quad (\text{Eq. 1.5})$$

in which the time t is measured relative to the instant of stopping the penetration; A and B are experimental constants, which depend on the details of the penetration history. For both PMMA and PC the constant A was found to be nearly proportional to velocity, whereas the B term was much more weakly dependent on this parameter. In purely elastic materials the product AB must vanish. The data gave no indication of such a tendency with increasing penetration velocity.

The above relaxation law is inconsistent with the concept of intrinsic independent molecular relaxation processes. However, by formulating a relatively simple cooperative molecular model,⁽⁴⁾ it was possible to account not just for the form of the law but also the dependence of A on penetration velocity. Briefly the model proposes that (1) the fluidity of the polymer is increased by disentangling the polymer chains, (2) the disentanglement process results from the stretching or flow of the polymer and becomes easier as the unsnarling progresses, (3) the polymer spontaneously reentangles at a rate proportional to its fluidity. Thus, for any given strain rate there should be a dynamically equilibrated state of disentanglement, which in turn fixes the fluidity. Changing the strain rate leads to transient responses, qualitatively in accordance with experience.

In most of the work the standard ball diameter was 4.5 mm. However, a few measurements were made using pointed indenters of various cone angles. In other experiments the use of spheres of various sizes provided additional insight into the impact process.

For a fixed penetration velocity the force can be related to the penetration depth and ball radius by the empirical equation:

$$P = kX^m R^n \quad (\text{Eq. 1.6})$$

in which k is a constant having the dimensions of an elastic modulus. Dimensional analysis requires that $m + n = 2$. As noted above m is approximately 1.5 at small depths but tends towards 1 at larger depths. Measurements at various ball sizes showed n to be 0.3-0.4 at small depths and 0.4-0.6 at large depths. At large penetration depths the dimensional requirements on n and m are violated, indicating that the phenomenological description is incomplete. For example, diameter also has a significant effect on the relaxation processes through its effect on the A and B parameters in equation 1.5.

1.1.2 Prior Work Using the Instrumented Impact Bar Methods

In the experiments at higher velocities, propelling projectiles in free flight against the target materials adds an additional degree of realism to the experimentation. On the other hand the measurements become more indirect, since the time dependence of velocity is no longer independently controllable. Load cells can no longer be used to measure the reaction force when the rate of load generates appreciable inertial forces in the sensor system. With free impacts the pulse duration can typically be of the order of 0.1 ms or less. Under these impulse conditions measurements are generally made instead using an impact bar. The target material is located on the end of the suspended bar, where it is struck by a projectile. The bar is made to be sufficiently long that the resulting pulse can be completely generated and acoustically transmitted down the bar, before interference from its reflection from the other end of the bar. The signal is detected by a suitable strain gage or other sensor located as close to the source as possible to minimize distortion, yet far enough distant from the struck end so that the pulse can be assumed to be propagating as a plane wave. In our case the strain gages were mounted about 6 bar diameters from the end. Measurement of the impact momentum, the velocity of the projectile and if possible its rebound velocity, are needed for subsequent analysis.

The impact bar technique has long been widely used to study material behavior at high strain rates. However, more conventionally a known shock or step force is initially applied uniformly over the entire cross-section of the specimen. The bar itself often serves as the specimen and usually the aim is to determine the mechanical properties of the materials under plane strain or plane stress condition. In the present case, we wish to study the effect of a concentrated impact force of initially unknown magnitude or time dependence. Because the pulse is essentially generated by a point source, it propagates initially as a spherical wave. Hence, in order to analyze the pulse in terms of plane waves, it is necessary to locate the sensors some distance from the specimen.

If sound velocity were constant, independent of frequency or wavelength, a pulse would propagate without change of shape and the pulse detected at the sensors would faithfully reproduce the impact event. The pulse corresponding to the impact event can be analyzed to compute the inferred penetration depth, energy absorption, and reaction force. The procedure for doing this is found in the Appendix. Thus, the impact bar data can be converted to that obtained on the mechanical test machines.

However, sound velocity in a bar is not constant, but depends on wavelength or frequency. The theory of the velocity dependence for the case of transient pulses is incomplete. The classical theory of dispersion (velocity variation) considers the interaction between the dimensions of the bar radius and the sound wave length. Materials having high Poisson ratios are more dispersive at high frequency than are those having low Poisson ratios. However, in all materials ultimately the low frequency components travel 60% faster than the high frequency ones. Preliminary calculations show that the range of frequency components comprising impact pulses unavoidably span the most dispersive region. It is this kind of dispersion that is commonly discussed in connection with impact bar methods.

There are other sources of dispersion at the low frequency regime. The sound velocity in a bar is given by $\sqrt{E_0/\rho}$, where E_0 is the Young's modulus and ρ is density. However, in a polymer E_0 itself depends on frequency. (Another manifestation of this dependence is the relaxation modulus). This effect predicts the inverse of the preceding one, namely that high frequencies propagate faster than low frequency ones.

Both the geometric and the molecular mechanisms are usually considered in the context of an infinite wave of some fixed frequency. These analyses forbid wave propagation in a rod at velocities in excess of $\sqrt{E_0/\rho}$. However, in pulses arising from a localized encounter, the strain field is complex, and the transient nature does not satisfy the assumption of an infinite travelling wave. The complicating transient effects are discussed in 2.1, 2.6 and 5.4.

For purposes of our studies if the wrong pulse shape is used to compute the penetration vs depth behavior, as discussed above, the results can be very misleading. The most basic information about the target materials is contained in their response as penetration first starts. Unfortunately, it is the start of the pulse that is most severely affected by dispersion. In order to ensure that corrections for these and other factors have been adequately considered, and because the impact bar instrumentation and technique is less direct than for the case of mechanical test machines, an interim goal has been to validate the impact bar results. The most straightforward approach is to use an ideal elastic material such as glass as the target for which the force-time relationship at the impact site can be computed from elastic theory.

The two studies^(5,6) preceding the current one were largely devoted to (1) finding suitable experimental, theoretical, and analytical approaches to overcoming the dispersion problem, or in rendering it insignificant, and (2) verifying the impact bar results.

An additional factor of concern is the acoustic coupling between the specimens and the impact bar. Mismatch of acoustic impedance* results in only partial transmission of the signal from the specimen into the bar, the remainder being reflected back into the specimen. Thus, large impedance differences trap the pulse. This also can lead to gross discrepancy between the transmitted signal and the instantaneous force-time relationship provided by the impact. The original approach was to make the impact bar out of PMMA, thereby, essentially eliminating the acoustic mismatch problem. The plan for correcting for dispersion was to Fourier-analyze the observed pulse signal. The originating pulse could then be derived by resynthesis after correcting each term for the phase shift induced by the frequency-dependent velocity. The dependency of the velocity on frequency would need to be measured. However, the use of a Fourier series description was shown to lead to artifacts because the pulse is non-periodic. Furthermore, correctly assigning the initial phases and carrying out the phase corrections becomes increasingly uncertain, difficult, and impractical for all except the first ten or so terms.

Other approaches were to use other less-dispersive, elastic bar materials. One of the additional problems with the PMMA bar was that even though impact signal strains in the bar were very small, typically .0003, nevertheless, the strain did not return to its initial unstressed level after passage of the impact pulse. This created difficulties with respect to applying conservation of momentum calibration procedures to the data. Hence, the PMMA bar was replaced by an aluminum one. This had the additional advantage that the impedance of Al closely matches that for glass. The observed pulse obtained with the glass target was very close to the theoretically calculated pulse. Results using SiC as the target gave similar agreement. Hence, the Al bar was considered to be performing satisfactorily, and was used to determine the impact response of PC, PMMA, and cured epoxy specimens by 4.5 mm and 19 mm diameter strikers at impact velocities of 1.8 and 2.9 m/s.

* Acoustic impedance Z is defined as $\sqrt{E_0\rho}$, and the reflection at the boundary between materials 1 and 2 is given by $(Z_1 - Z_2)/(Z_1 + Z_2)$.

These data were examined first using such general shape parameters as the peak strain and the pulse width at half the peak strain value. The amount of energy irreversibly consumed in the impact process was found to increase in the order glass < PMMA < epoxy < PC, and that impacts involving large diameter projectiles are more elastic than for the case of small diameter ones. The data were further analyzed to yield the time vs penetration depth behavior as well as the energy absorbed in the immediate region of the impact. The force vs penetration depth results were reproducible, and were similar to those obtained using the electro-hydraulic test machine. However, the absolute value of the forces was 20-25% lower than the value obtained using the latter equipment. The reason for this discrepancy is not known.

The observed dispersion effects were smaller in the Al bar than in the PMMA bar. Nevertheless they became increasingly detectable as the impacts became more abrupt. In the case of glass and SiC targets the observed pulse seemed to "taper on" over a time span of $2.3 \mu\text{s}$ and $6 \mu\text{s}$ respectively. Inasmuch as impact velocities of $\sim 250 \text{ m/s}$ were planned, during this "taper-on" interval the projectile would travel about 0.5 - 1.0 mm. If this taper-on were interpreted as the actual force behavior it would result in a false computed force-penetration relationship in which the glass or SiC was apparently very soft over the depth range corresponding to this interval as just discussed. This artifact will also occur when the target is polymeric and is impacted at high velocity. Therefore, the problem of dispersion, while rendered innocuous at the relatively low impact velocities remained unresolved with respect to impact velocities achievable using a compressed gas gun.*

Finally, in a parallel series of experiments photographs of the impact of a 4.5 mm steel projectile with PC and PMMA targets were made. Velocities of about 100 and 140 m/s were produced using the gas gun and the pictures were taken with an Ima-Con high speed camera at intervals of $5 \mu\text{s}$ per frame, and the polymer samples were attached to a massive steel block. In the PC material a diffuse densified zone found under the projectile during penetration and became much more distinct after the impact. No cracking occurred. In the case of PMMA, the zone was much more distinct initially but seemed to contract very substantially after impact. Cracking in this case occurred at 140 m/s and initiated at the point of maximum penetration.

1.2 Objectives of the Present Study

The purposes of the present contractual effort were (1) to conduct impact measurements on the PC and PMMA materials at the highest velocities feasible with the gas gun, (2) to find a way to correct the pulse signal so as to reveal the actual force-time history of the impact either by rendering pulse distortion negligible, or by making the necessary corrections, and (3) to bring together the body of information gained to date into a model of the materials properties relevant to impact resistance per se and that distinguished the PC from PMMA.

The prior work provided the foundation for these continuing studies. However, a clear approach to dealing with objective (2) was not evident although some additional clues were available. Extending the work into the higher velocity regime was technically motivated by the fact that in this regime PC exhibits continuing resistance to im-

* The problem of pulse shape distortion due to dispersion has long been recognized. In principle the solution to the problem is contained in the classical theory of (time dependent) continuum mechanics. Formal exact solutions relating to the present problem have been given⁽⁸⁾. These require the evaluation of intractable integrals. Approximate solutions are known which are only valid for long times after the arrival of a pulse. These account for the "ringing" that occurs in the trailing regions. However this writer knows of no solution to the behavior of leading edge as the pulse propagates.

pact fracture, whereas PMMA is finally starting to exhibit brittle cracking. Hence, the most pertinent information is likely to be obtained at these velocities. Furthermore, this range of velocity is of most practical interest to common experience.

The following section provides an in-depth overview of the attack on these objectives. This is then followed by detailed documentation and discussion of those elements directly leading to the resolution of those objectives.

2. OVERVIEW OF PRESENT WORK

Although our prior work served as the foundation, the present study has been more exploratory than expected because the means of analyzing the experimental results had not been resolved. A particularly nagging problem that remained was how to identify the arrival time of the leading edge of the impact signal, and how to determine the shape of the start of the pulse. The experimental and analytical aspects of the work were interdependent because the choice of the bar material and geometry affected the strength and distortion of the pulse signal, which then required correction by the data analysis procedure. The path for resolving these issues contained dead ends along the way. This chapter provides an overview of this study as it proceeded, including those procedures that worked, as well as those having a more will-o'-the-wisp character. The "successful" portions are treated in depth later.

2.1 Correction of Pulse Shapes Using Transfer Functions

Our prior work showed that a Fourier *series* approach to correcting a pulse slope for dispersion is fundamentally inappropriate and inadequate. The correct procedure would be to use a Fourier *integral* representation, but this is intractable. However, another approach widely used in the signal communications field showed promise. This method analyzes pulses in the amplitude-time domain rather than in the amplitude-frequency domain.

In the language of signal communications an input signal given by some time dependence $F(t)$ is introduced into a "channel" (amplifier, transmission line, filter, or other system) from which an output signal $G(t)$ emerges. The properties of the channel are assumed to be fixed and not altered by the signal. The channel can be characterized by its own function $H(t)$, called the transfer function. This concept can be represented schematically as follows:

$$\begin{array}{ccccc} \text{Input Signal} & \rightarrow & [\text{Channel}] & \rightarrow & \text{Output Signal} \\ F(t) & & H(t) & & G(t) \end{array}$$

In our case the input signal is the impact event, the output signal is that observed by the strain gage sensor, and the channel is the impact bar. The way the channel acts on the input signal to yield the output signal is given by:

$$G(t) = \int_0^t F(t-\tau) H(\tau) d\tau \quad (\text{Eq. 2.1})$$

This equation can be solved for $H(t)$ using Laplace transforms if $G(t)$ and $F(t)$ are known. Since the impact bar between the impact site and the sensor location remains constant for any particular impact bar, once $H(t)$ for the bar is determined, it should be applicable to any pulse. Similarly, by inverting Eq. 2.1, one can write:

$$F(t) = \int_0^t G(t-\tau) H_o(\tau) d\tau \quad (\text{Eq. 2.2})$$

where $H_o(t)$ is the transfer function for the inverse process of correcting the output signal to reveal the original signal. This approach is widely used for applications ranging from designing correction filters for high fidelity sound systems, to deciphering electronically scrambled information. The transfer function approach is actually mathematically equivalent and related to the Fourier integral method. When the output data is produced at discrete intervals, the integrals in Eqs. 2.1 and 2.2 are replaced by corresponding summations.

For the present case $F(t)$ can be calculated on the basis of the Hertz elastic theory provided that the target material is a purely elastic material such as glass or silicon carbide. The output function $G(t)$ is the measured pulse as detected by the sensor that corresponds to the calculated pulse. It is useful to think of the transfer function as a kind of memory which reads an incoming signal at some instant but retransmits it out over a period of time with some fixed weighting pattern. This period is expected to be finite in duration ranging over the interval defined by the maximum and minimum sound velocities.

When the start of the observed pulse was used to calculate the transfer functions, the results were found to be very sensitive to the value assumed for the arrival time of the leading edge of the pulse. Other determinations of $H_o(t)$ can be obtained by using other portions of the pulse. The computed transfer function depended on the portion of the pulse selected as well as on the value of the period and the leading edge arrival time. Noise and systematic variations between nominally identical experimental runs also affected $H_o(t)$. To find the best overall representation a computer program was developed that produced an average $H_o(t)$ by scanning a range of data. The period and pulse arrival time could also be systematically varied. That combination of parameters that led to a transfer function that resulted in the least error between the calculated $F(t)$ and the actual $F(t)$ was assumed to lead to the best estimate of $H_o(t)$. The effort then turned to obtaining precise, high reliability data for $G(t)$, for cases where $F(t)$ could be calculated with a similar level of assurance. However, the accurate determination of the leading edge arrival time remained a matter of high priority.

From the start of the effort in the transfer function approach, it was clear that a difficulty would arise if the dependence of $G(t)$ as a power of t were to be greater than that of $F(t)$. This emphasized the importance of the time t which is measured from the start of the input signal, i.e. from the arrival time of the leading edge. If such a power dependence were to occur there could be no mathematical solution to the convolution equation 2.2. Therefore, a physical argument indicates that $G(t)$ cannot have such a greater power dependence in as much as $F(t)$ is in fact the predecessor of $G(t)$. This consideration placed a restriction on the acceptable functional description for the leading edge portion of the pulse. However, this restriction was considered to be helpful rather than a problem because it somewhat constrained the range of possible values for the start of the pulse signal.

As will be discussed later, this resolution of the potential problem appears to be in error. Thus, the use of a transfer function to correct the pulse for dispersion was later abandoned in spite of its apparent theoretical soundness.

2.2 Theoretical Studies of the Behavior of the Pulse Leading Edge

The need for correctly and accurately determining the start of the impact pulse, because spurious effects may result, has already been emphasized. The problem arises because of the difficulty in defining when and how the pulse, (which starts out with zero amplitude and slope) rises from the background noise level. As suggested by Eq. 1.1, the original impact pulse is expected to increase in force and level as about the $3/2$ power of impact time in accordance with the Hertz analysis. Whether this power dependence is preserved as the pulse propagates down the bar was an unanswered question. Determination of the start of the transmitted signal would be greatly simplified if the asymptotic behavior of the leading edge could be theoretically established. Accordingly a study was undertaken to determine the evolution of the leading edge of a pulse that initially is proportional to $t^{3/2}$. The approach was to introduce this initial pulse form into the elasticity equations and to concentrate on the behavior just

at the leading edge. The simplest appropriate equation that incorporates dispersion was given by Love⁽⁷⁾ and is:

$$u_{tt} - K^2 v^2 u_{xxt} = C^2 u_{xx} \quad (\text{Eq. 2.3})$$

where u is displacement, C is the extensional velocity, K is the radius of gyration, v the Poisson ratio, x axial distance and t time.

Attempts to use this equation to solve this problem analytically by power series, Laplace transform, or Fourier analysis methods led to either intractable or discouragingly complex formulations and were abandoned. A finite difference approximation was then used to explore the behavior, assuming initially that the pulse propagated without dispersion, and then correcting the form by successive approximations using the above equation. As the propagation time was made to advance, the computer results at the leading edge became unstable with respect to successive iterations. This instability occurred independently of the refinements used to represent the derivatives or the scale of the difference intervals selected. It has been already be noted that formal solutions⁽⁸⁾ to the present problem, while statable, are very difficult to apply to the leading edge behavior.

The approach that proved to be the most fruitful was a semi-empirical one based on examination of the experimental results in combination with satisfying certain basic physical principles. This is discussed in Section 5.4 after discussing the analysis of the experimental results in Section 5.3.

2.3 Impact Bar Dispersion and Acoustic Impedance Matching Considerations

Although the previous study showed the 2.5 cm O.D. aluminum impact bar to be appreciably less dispersive than the PMMA bar first used, the Al bar was in turn replaced by a 1.25 cm O.D. vitreous silica bar. The smaller diameter was chosen to improve the frequency dependence of the dispersion and to provide greater strain signal output. Vitreous silica was selected to reduce further the dispersion level because of its relatively low Poisson ratio. Furthermore, SiO_2 and Pyrex glass specimen targets are very well matched acoustically. All of these factors are favorable for the determination of the characteristic transfer function of the SiO_2 bar material. However, the acoustic impedance match with polymeric target specimens is poor.

The choice of the ideal impact bar for use with polymer target materials presents a mild dilemma. If a polymer bar is used, the acoustic coupling is good, but the dispersion effects are relatively severe. If a SiO_2 or Al bar is used, the acoustic coupling is poor (an increasing problem as the impact velocity increases) but the dispersion is less. Correction for acoustic mismatch is done by the use of a convolution procedure as in the case of the transfer function correction. Both the acoustic impedance and the acoustic reverberation time as determined by the sound velocity depend on the appropriate elastic modulus and density of the material.

The resolution to this Hobson's choice was effected through the following stratagem. First, a glass target mounted on the SiO_2 rod was impacted to enable the transfer function for this rod to be determined. A hemisphere of glass was then substituted for the glass specimen. The SiO_2 impact bar, suspended by fine wires in the manner of a pendulum, was mounted in tandem with a similarly suspended PMMA impact bar, onto which a PMMA specimen was mounted. The SiO_2 bar was then displaced axially away from the other bar and released so that when it swung, the two bars impacted end on. The impact signal was read from each bar. Since one impact event generated the pulse in the two bars, the two observed signals, when properly

corrected, must be identical. The pulse in the SiO_2 bar was corrected by means of its previously determined transfer function. This corrected signal, in combination with the observed signal in the PMMA bar now provided the required information to compute transfer function in the PMMA bar. Thus, the complications due to impedance mismatch effects have been eliminated in both bars. Having now (apparently) achieved a clean determination of the transfer function in the PMMA bar, that now became the preferred bar. This choice was also predicated on the difficulties that would be experienced in correcting the data for reflection if the SiO_2 bar were used. The reverberation time would be about $12 \mu\text{s}$ in a 12 mm thick specimen. Neither this time nor the reflectivity would remain constant because of the intrinsic dispersion of the polymer materials. Since pulses of the order of only $100 \mu\text{s}$ duration were anticipated in the high velocity impacts, these characteristics would be very unfavorable.

2.4 Experimental Impact Measurements

The calibrated PMMA bar, was used in subsequent impact measurements using PMMA and PC target specimens. Measurements were first made in which a spherical pendulum bob served as the projectile. This arrangement paralleled our prior work using the Al bar, and ensured good control of the impact position, and the accurate determination of the impact and rebound velocities. These velocities are needed to compute the momentum and kinetic energy parameters. Momentum can also be determined with less precision from the recoil swing of the suspended impact bar.

In shifting to the compressed gas gun, the projectile velocity was determined from the time interval to interrupt two light beams a known distance apart. The projectile rebound velocity could no longer be measured directly, but had to be inferred from the recoil swing of the impact bar. For this work a second strain gage was added the same distance from the first as the first is from the specimen end of the bar. The two strain gage signals were recorded at a common time base at $0.5 \mu\text{s}$ intervals. This second gage was originally intended to provide a further check on the validity of the previously determined transfer function. Ballistic measurements, using the gas gun, were made in duplicate on PC and PMMA at two different velocity levels using the 4.5 mm ball bearings as the projectiles. Very good reproducibility was experienced between duplicate runs.

2.5 Analysis of Experimental Results

In the cases of impacts using glass and SiC targets, in the ideal dispersionless situation it is valid to invert Eq. 1.1 to yield

$$x = u(t - t_0) = (P/K_0)^{2/3} \quad (\text{Eq. 2.4})$$

in which

$$P = AE\epsilon$$

or

$$t = t_0 + [(AE/K_0)^{2/3}/\epsilon]^{2/3}$$

$$= t_0 + C\epsilon^{2/3}$$

In this relationship P is force, A is the bar cross sectional area, E is Young's modulus,* K_0 the constant in Eq. 1.1, in the impact velocity, C the proportionality constant defined by the equations, ϵ the observed strain, t is the clock reading, and t_0

* Henceforward the subscript will be omitted from the time-independent Young's modulus.

is the clock reading at the time of initial contact. Thus, plotting $\epsilon^{2/3}$ against time leads to a linear relationship, and the intercept with the zero strain axis fixes t_0 . Because of the lack of an a priori theoretical model for the behavior of the leading edge, and because of the restrictions on the functionality of the pulse shape imposed by the transfer function approach, our working hypothesis was that the toe of the pulse should increase at no more than the $3/2$ power of the pulse time. Hence, such a plot should remain useful because the curve at t_0 should be either vertical or have a finite slope.

However, such plots of the new data obtained using the gas gun did not indicate a tendency for the slope to approach the zero strain axis with a finite slope, but rather persisted in tending towards this axis with zero slope. At this point the preconceived condition of Hertz-like behavior of the propagated pulse was relaxed and instead the data was fitted to:

$$t = t_0 + C\epsilon^{1/n} \quad (\text{Eq. 2.5})$$

where n was that exponent that provides the best empirical fit to the data, and C is new proportionality constant. A good fit over a large portion of the start of the pulse was obtained for $n = 4$ for the data from the first gage position and similarly for $n = 6.3$ from the second gage position. This result suggested that more of the start of the pulse was obscured by the zero signal noise than had been realized. These plots allowed a well-defined extrapolation to the zero axis within experimental scatter. Justification that these power functions are physically significant is given in Section 5.4.1. These pulse arrival times could then be used to estimate the velocity at which the leading edge advances. This result was found to be very close to the compressional wave velocity. However, most of the pulse, such as the peak portion travels at a velocity that is characteristic of the extensional wave propagation expected for longitudinal sound propagation in a cylindrical rod.

These velocity results conflict with the expectations of the classical theory of continuous wave propagation in a cylinder discussed in 1.1.2. The classical theory precludes sound propagation in a bar in excess of the extensional velocity. This discrepancy between physical expectation, which is concordant with our results, and the predictions of the classical continuous wave analysis has been noted by Kolsky.⁽⁹⁾

Furthermore, if the correct value of n is 4 or 6.3, then there is no mathematical possibility of finding a transfer function that can work in Eq. 2.2. This conclusion carries the implication that the Fourier integral approach, using the above classical theory for the dispersion correction terms, would have led to erroneous results. These conclusions indicated that an entirely new approach to the dispersion correction problem was required.

2.6 Semi-Empirical Approach to Pulse Shape Correction

A careful examination of the experimental data revealed that n in Eq. 2.5 and propagation velocities of the leading edge and the pulse maximum were constants. The results were independent of the material impacted or the impact velocity. The observed pulses could be empirically fitted from the leading edge to the pulse maximum with little error by an equation of the form:

$$Y = Ax^n - Bx^m \quad (\text{Eq. 2.6})$$

in which Y is the amplitude, x is the time since the first arrival of the pulse, and A , B , n , and m are constants to be determined. The requirement that the peak correspond in magnitude and time with the observed value, and that the exponent n at the leading

edge also match that found, leaves only one adjustable constant to fit the rest of the data. The position of the peak relative to the leading edge is predictable from the two propagation velocities. The dependence of n on position can be inferred in part from the measurements, and in part on theoretical grounds. The latter is based on the following argument. The leading edge propagates faster than the rest of the pulse. This extension can be accommodated by an increase in the power dependence on t with increasing distance travelled. The shape to which a given pulse will evolve as it propagates can be validly determined by convolution. If the transfer function appropriate to this process leads to an increase in the power dependence with increase of propagation distance, then conversely the starting pulse must have had a lesser power dependence. The same transfer function can be assumed to operate over any portion of the bar of the same length. Thus, a fixed change in the power dependence is expected over a fixed distance. In other words the exponent of about 6.3 at the second sensor position, and of about 4 at the first sensor position, is a change of exponent of 2.3. This in turn implies an exponent of about 1.7 at the bar end and 1.5 at the impact site. (This is the value computed using the Hertz elastic model.) Thus, the essence of the transfer function concept has been retained, except that convolution as a mathematical procedure has been supplemented by a more qualitative procedure.

This overall approach to pulse correction is discussed in depth in Section 5.4. By this means the observed pulses were corrected to infer the shape of the initial impact pulse. The corrected pulse was then introduced into the procedures for determining the penetration behavior.

2.7 Derived Material Response Behavior

The corrected pulse data were analyzed to deduce the force-penetration depth, penetration depth-time, and local energy-penetration depth dependences. The results on the PMMA bar using the pendulum impacts largely confirmed the results previously obtained using the Al bar. The new procedure appears to have eliminated the artifacts noted in our previous studies in the high velocity impacts. The results on PMMA using the compressed gas gun appear to be extensions of the data produced using the mechanical test machine, whereas those results on PC indicate an anomalous softening with increasing impact velocity. The results are presented in Section 6.1 and 6.2. Both materials exhibit evidence of load relaxation during the course of the penetration. The peak loads occur prior to reaching the peak penetration depths.

2.8 Modelling of the Material Behavior

A visco-elastic model of the material behavior was developed which incorporates the elements of the model used to explain velocity-dependent relaxation behavior given by Eq. 1.5. The model is aimed at accounting for the observed penetration-time-force inter-relationships, at a better understanding of how the molecular and structural responses are influenced by the initial impact conditions, and at trying to account for the differences between the polymers. The model is developed in terms of a system of elastic responses and velocity-time-dependent viscosity responses. These responses act partly in parallel and partly in series. In PC it appears that the initial response is almost a purely parallel behavior. In PMMA the behavior is about 25% parallel and 75% series.

3. MATERIALS AND SPECIMEN PREPARATION

The PC and PMMA materials were unchanged from those used in the previous study. Specimens were used as cut out of sheet stock, making sure that all burrs were removed. The standard specimen size was 25 mm O.D. \times 12.5 mm. The other target materials are described below.

3.1 Polymethylmethacrylate

Specimens were cut from a single sheet of Type G Plexiglass^R PMMA (produced by Rohm and Haas). Continuing with our former practice, the sheet was marked off in squares for cutting and a record kept so that the original location of each specimen in the sheet could be identified.

3.2 Polycarbonate

The PC resin was manufactured by the General Electric Company and is designated as Lexan^R resin general purpose glazing sheet, Type 9034-112. A single sheet of 12.5 mm thick material was used, and specimens marked, and records kept as for the case of PMMA.

3.3 Inorganic Glass

A sheet of Pyrex^R borosilicate glass (made by Corning Glass Works) 12.5 mm thick was ground into 125 mm diameter disks for use in calibrating the SiO₂ impact bar.

3.4 Silicon Carbide

A piece of fully dense, hot pressed silicon carbide produced by the Norton Co. was ground into a cylinder having a 12.5 mm diameter and a 11.9 mm height. This height corresponds to a calculated acoustic reverberation time of 2 μ s.

4. IMPACT BAR STUDIES

The experimental arrangement of the impact bar is in many respects unchanged from the previous contract study. The main differences are that two new bars were made, one of vitreous silica, the other of PMMA having diameters of 12.5 mm and 25 mm, respectively. The wire strain gages were replaced by semiconductor gages. The resultant improvement in signal strength eliminated the need for pre-amplification of the signal ahead of the Nicolet Model 2090-2 storage oscilloscope.

The specimens were mounted on one end of the 180 cm long instrumented impact bar. The specimen diameters either matched or were less than the bar diameter to avoid reflections at the overhang. The arrangement is shown schematically in Fig. 4A.

Strain gages on the bar connected to a Wheatstone bridge and the output to a digital storage oscilloscope enabled the strain pulse produced by the impact to be recorded. Mathematical processing of the pulse data, using a simplified one-dimensional model for the stress distribution in the impact bar, allows the force, penetration depth, striker velocity, various energy terms and the momentum transfer to be computed. This procedure is given in the Appendix. The polymer PMMA was the final selection as the impact bar material because of its very good acoustic impedance match with the target specimens. Secondly, the small value of its Young's modulus resulted in a large strain for a given force. This was favorable with respect to signal-to-noise considerations.

The bar was supported at two places along its length by two bifilar fine wires in the general shape of a V. This allows the bar to swing freely along its axis, while substantially preventing sidewise displacement. A similar arrangement was used to support the striker. From the amplitude of the swing of the bar after the specimen is impacted by the striker and from the initial position of the striker before its release, the momenta and kinetic energies can be computed. Two striker geometries were used. One was a 19 mm, 28.3 g steel ball. The other was a 42 g steel cylinder with one end in the form of a nose terminating in a 4.5 mm diameter spherical cap. The latter geometry provided continuity with prior indentation work and with the air gun work using 4.5 mm projectiles. This pendulum striker arrangement was convenient for impact velocities up to about 2.5 m/s.

Higher impact velocities were produced by firing a 4.5 mm steel ball from a modified air rifle using a controlled pressure of He as the propellant. The gun was mounted on an I-beam equipped with aiming adjustments as well as with a pair of photocells placed a known distance apart. The velocity of the projectile was determined on an interval timer triggered by the interruption of the light beams aimed at the photocells. Because of degradation of the accuracy of the trajectories at both high and low propellant pressures, the impact velocities were restricted to between 120 and 220 m/s. The projectile was aligned to be coincident with the axis of the bar and the center of the target specimen mounted on the suspended impact bar.

In the case of the gas gun experiments two sets of strain gages were mounted on the PMMA impact bar, one set 15 cm from the end of the bar, and the second set 30 cm from the end. The pulse signals detected by each of the two sets could be recorded simultaneously in separate channels of the oscilloscope.

4.1 Impact Measurements Using Vitreous Silica Bar

The vitreous silica bar was used at the beginning of this study because its unusually small Poisson ratio results in an advantageously small dispersion. Impact measurements were made on Pyrex glass and hot-pressed silicon carbide specimens which were impacted by a 19 mm steel ball bearing at a velocity of 1.77 m/s. Preliminary results

made on specimens having a larger cross section than the bar, when compared with later results showed the importance of using targets that match the cross section of the bar. This is shown in Figs. 4.1A and B.

4.2 Use of Vitreous Silica as a Striker

The small degree of dispersion in the vitreous silica bar made it advantageous for use as a means of calibrating the PMMA bar. For the reasons discussed in Section 2.3 SiO_2 was unsuitable for use as the bar material in combination with polymer targets in high velocity impact experiments. However, by mounting a glass hemisphere on the end of the SiO_2 bar, it could be made into a particularly ideal striker. The strain gage on the SiO_2 bar would sense a relatively distortion-free signal arising from its impact with the target on the PMMA bar. Hence, the pulse as detected in the SiO_2 bar could be directly compared with that detected in the more dispersive PMMA bar. The nominal similarity between the two signals of the same impact event are seen in Fig. 4.2A. Note that the times do not coincide because of the differences in the propagation velocities and in the positions of the gages in the two bars. Note also the more gradual onset of the leading edge signal in the case of the PMMA bar.

4.3 Impact Measurements Using the PMMA Bar

Using the 42.05 g striker that is fitted with a 4.5 mm diameter tip, impact measurements were made in duplicate on PC and PMMA specimen targets. The impact velocity was about 2.1 m/s in all cases. A representative example is given in Fig. 4.3A. There was good agreement between duplicate measurements as shown in the table. The pulses were similar in behavior and appeared to be nearly classical in form. The pulse rose to a maximum and diminished again without crossing the zero strain axis. The only slight irregularity is that the strain level remained positive after the pulse had apparently passed. This may be due to a slight creep of the PMMA impact bar under the pulse load.

A second group of experiments was made using the gas gun to produce the impacts on the PC and PMMA targets. Duplicate experiments were run at nominally 125 and 220 m/s on both PC and PMMA targets. The pulses at the two gage positions were recorded in each case. The duplicate runs gave remarkably similar signals, even including the complex structure of the trailing portion of overall pulse. This can be seen by comparing Fig. 4.3 B with C. The pulse received at the second gage typically had less fine structure and displayed larger, better developed lower frequency oscillations as may be noted by comparing Fig. 4.3 C with D. While the pulse pattern for PC and PMMA were different in detail, they were comparable in general character. This can be verified by comparing Fig. 4.3 B with E. The most noticeable difference is the somewhat longer period for the initial half wave in the case of PC relative to PMMA. Finally, there appeared to be little general effect resulting from increasing the impact velocity from 125 m/s to 220 m/s other than increasing the amplitude of the pulse. This is shown in Fig. 4.3 F relative to B.

5. CORRECTION OF IMPACT PULSE DATA FOR DISPERSION

This is the most crucial portion of the work because of its effect on the calculations that reveal the impact response of the target specimen material. If the force-time relationship at the site of the impact were known exactly, then the force could be used to compute the projectile deceleration and the force-depth relationship could be determined exactly. Thus, the problem is to transform the pulse data observed at a later time and at a position remote from the impact site, into the original pulse shape. For these purposes the correct assignment of the start of the pulse, and the correct quantitative description of the force during the initial stages of the projectile penetration are vital to determining the characteristic visco-elastic properties of the target material. The correct shape of the entire pulse is needed to reveal the relaxation, the maximum penetration and force, the energy absorption processes as well as the rebound response.

The correction procedure is first to concentrate on the leading edge behavior to define its arrival time and shape. Then the overall pulse shape and the rate at which the various regions of the pulse propagate are considered. These differences in the propagation velocity are responsible for the pulse distortion. The quantitative description of the evolution of the shape is then inverted to deduce the shape at a preceding time and location, specifically the time and place of the impact. Second order differences determined earlier in the process are reintroduced as fine adjustments. This completes the correction of the observed pulses.

5.1 Detection and Characterization of the Leading Edge

Leading edge arrival could be observed at three independent sensor locations viz. the SiO_2 bar gage, and the two gages on the PMMA bar. However, because the dispersion in the SiO_2 bar was so small, the start of the pulse was virtually directly observable in the special case of the collision between these two bars.

5.1.1 Vitreous Silica Bars

In the impact of the 191mm steel ball with the Pyrex specimen mounted on the SiO_2 impact bar the conditions for an elastic impact were satisfied. Hence, as previously shown in Eq. 2.4 the $(2/3)$ power of the strain should increase linearly with time starting at the instant of first contact. The plot in Fig. 5.1A for the experimental results of the average of the two duplicate runs show a slight departure near the very start of the impact. The deviation between the extrapolated impact time and the probable actual time is about $1 \mu\text{s}$. This indicates that the signal from this bar can be used without correction to an accuracy of about $1 \mu\text{s}$ for pendulum impacts such as those used in the present experiments.

5.1.2 PMMA Impact Bar

5.1.2.1 Vitreous Silica Bar Collision with PMMA Bar

With the knowledge that the signal from the SiO_2 impact bar is a good representation of the actual impact process, it is interesting to examine the leading edge behavior for this experiment. A representative plot of the $2/3$ power of the observed strain vs time in the PMMA bar is shown in Fig. 5.1 B. Whereas the signal in the SiO_2 is seen to be linear within experimental error, the corresponding curve for the PMMA signal which is linear some distance above the zero strain axis, clearly does not approach the abscissa linearly. The start of the pulse is difficult to define, but cursory examination suggests that it may occur at least $10 \mu\text{s}$ prior to the time suggested by extrapolating the more linear portion back to the abscissa.

However, if the data is represented instead by the empirical Eq. 2.5 then the linear behavior shown in Fig. 5.1 C results for $n = 4$. A duplicate run, not shown, for the two bar impact gives the same linear behavior for this value of n . There is increase in scatter near the zero axis due to the magnification that occurs in small quantities, such as random noise, when their 4th root is extracted. Values of the 4th root less than about 0.08 are attributable to noise. In spite of the long extrapolation to the zero strain axis, the intercept can be defined to $\pm 1 \mu\text{s}$. If this extrapolation is indeed the true arrival time of the pulse, then much of the start of the pulse is obscured by noise before it can be unambiguously detected.

It should be noted that the non-linear portion of the 2/3 power plot as well as much of the linear portion is linearized by the 4th root plot. The band of noise surrounding the zero strain axis, made apparent by the latter plot, is not as evident in the 2/3 power plot.

5.1.2.2 Pendulum Impacts

The start of the pulses for the pendulum impacts of PMMA and PC specimens by the smaller 4.5 mm diameter, 42 g striker has been similarly analyzed. The pulses sensed at the gage 15 cm from the bar end (16.2 cm from the location of the impact), in all cases show a non-linear behavior at small strains when examined by the 2/3 power plot. As before, identification of the start of the pulse is difficult as shown in Figs. 5.1 D-E. However, when the 4th power of strain is plotted instead, an approximately linear behavior is again seen in Figs. 5.1 F-G. The increasing prominence of noise at small strain levels is again evident.

5.1.2.3 Gas Gun Projectile Impacts

The leading edge of the pulse received at the 15 cm gage position for the impacts at 120 and 220 m/s, were similar to those from the pendulum impacts. Representative plots of the 4th root of strain are given in Figs. 5.1 H-I. However, the leading edge signals detected at the second gage, located 30 cm from the end of the bar could only be linearized if 6th root of the strain was used instead. The appropriate root was found by varying the exponent n one unit at a time until a linear curve was obtained. These results in Figs. 5.1 J-K also show the relative prominence of noise is increased even more. This increases the span of the extrapolation needed to define the start of the pulse signal. Consequently, there is greater uncertainty in the extrapolated value. A procedure for refining the estimate of the exponent is given in 5.3.

5.2 Propagation Velocity

In the experiments involving the two bar collision and in the high velocity impact experiments the pulse shape at two bar locations was simultaneously recorded on a common time base. Thus, the propagation velocity can be determined for the leading edge, the pulse maximum, the time of the zero crossing, and for other definable portions of the impact pulses. In the case of the SiO_2 bar the extensional and compressional wave velocities are almost identical being 5,760 and 5,968 m/s, respectively. The gage on the SiO_2 bar was 7.5 cm from the bar end (8.7 cm from the position of the specimen impact). Therefore the propagation time from the impact site to the sensor is about $15.0 \pm 0.5 \mu\text{s}$. Since there was a common time base for the signals in the two bars, subtracting $15 \mu\text{s}$ from the clock reading when the pulse first arrived at the gage in the SiO_2 bar represents the clock reading at the start of the impact. The 4th root plot, discussed above, was then used to estimate the arrival time of the pulse in the PMMA bar at the gage 16.2 cm from the impact site. From this data the propagation velocity in the PMMA bar for the leading edge was calculated to be $2660 \pm 30 \mu\text{s}$. The error represents the variance between two duplicate runs. The very

long duration of the two bar impact pulse precluded making velocity measurements on other parts of the pulse.

A more direct determination of the propagation velocities is possible when the two sensors are located on the same bar and there is again a common time base. In the high velocity impact experiments the pulse arrival times at the first gage position were estimated on the basis of the 4th root plots, while those at the second position 15 cm from the first were estimated on the basis of the 6th root plots. The procedure for determining the velocities is shown schematically in Fig. 5.2 A. The results are given in Table 5A. Note that the velocity results depend mainly on the position within the pulse rather than on how the pulse was initially produced.

Table 5A
CHARACTERISTICS OF PROPAGATION OF IMPACT PULSE BETWEEN
15 cm AND 30 cm SENSOR LOCATIONS ON 2.5 cm DIAMETER PMMA BAR

Pulse Location	Impact Velocity m/s	Propagation Time Between Gages μs		Mean Velocity m/s
		PC Target	PMMA Target	
Leading edge	120	56.85 \pm .25	54.75 \pm .75	2710 \pm 80
	220	54.50 \pm 2.4	55.55 \pm .95	
Half Max. Ht. (Ascending)	120	72.45 \pm .05	72.60 \pm .00	2070 \pm 10
	230	72.40 \pm 1	72.70 \pm .25	
Maximum	110	75.05 \pm .05	74.90 \pm .05	2000 \pm 5
	220	75.10 \pm .1	75.00 \pm .05	
Half Max. Ht. (Descending)	110	75.95 \pm .05	77.12 \pm .03	1960 \pm 15
	220	75.88	76.90 \pm .35	
Zero Crossing	110	78.50 \pm 1.2	77.75 \pm .05	1920 \pm 25
	220	78.00 \pm 0.7	77.80 \pm .05	

5.3 Analytical Representation of Overall Pulse

The total pulse, including the complex oscillations of the tail portion has a very complicated shape. These oscillations are due to internal reflections, dispersion, the excitation of propagation modes other than the simple longitudinal one, and to the later arrival of shear and surface waves. Axial momentum p is calculable from the integral,

$$p(t) = \int_0^t P dt \quad (\text{Eq. 5.1})$$

$$= EA \int_0^t \epsilon dt$$

where P is force, E is the Young's modulus of the bar, A its cross section, ϵ the axial strain in the bar, and t is time. When the integration of the measured strain over time was performed, it was found that the oscillations beyond the first zero crossing very nearly cancel and, therefore, are not involved in the net axial momentum transfer. Hence, we are effectively concerned only with the pulse shape up to the time that the

strain first crosses the abscissa. This results in an enormous simplification of the analysis. In any case, it is this first portion of the pulse that contains most of the information about the material behavior and the impact event.

As discussed in 5.1 and 5.2 the arrival time of the leading edge can be "defined" once the appropriate n is found that results in a linear curve. (The argument for the validity of this procedure for defining the true shape and pulse arrival time is given in 5.4.) Thus, the start of the pulse is given by:

$$\text{strain} = \text{constant} \cdot t^n$$

where t is the time since first arrival of the pulse. Other characteristics of the pulse are its maximum strain $\epsilon(\text{max})$ and the elapsed time $t(\text{max})$ at this point. For convenience we define

$$S = t/t(\text{max}) \quad (\text{Eq. 5.2a})$$

and

$$y = \epsilon/\epsilon(\text{max}) \quad (\text{Eq. 5.2b})$$

Then the following equation has the characteristics of having the proper dependence of strain on time at the start of the pulse, and the proper value and location of the maximum

$$y = \frac{S^n - S^m}{n - m} \quad (\text{Eq. 5.2c})$$

in which m is an adjustable constant, determined by an error minimization in comparison with the actual data. In fact using this equation, which is the normalized form of Eq. 2.6, both n and m can be varied to give the best fit. This results in a corrected estimate for n .

The preceding equation models the high velocity pulse data up to the maximum to within an error of a few per cent absolute, as shown in Fig. 5.3 A, corresponding to about 10% relative. Because of the small variation in propagation velocity noted for the descending portion of the pulse, there is only a small change in shape as the pulse travels. Therefore, this portion of the pulse has not been modeled. Rather the time scale is adjusted according to the pulse position and bar location.

5.4 Pulse Correction Methodology

This section is closely related to 2.1 and 2.6, which are recommended as background. Many of the ideas and basic information were shown schematically in Fig. 5.2 A.

5.4.1 Conceptual Basis

Introduction of a variable exponent into the empirical description of the toe region of an impact pulse, led to the interesting result that at a given sensor position the same exponent was applicable to a wide range of pulses. The exponent was about 4 at the first gage position, and somewhat greater than 6 at the second gage position. These exponents led to consistent, well defined values for the arrival times of the pulses. The value for the propagation velocity of the leading edge based on the data from the two gage positions on the PMMA bar was about 2610 m/s. This result compares closely with the value 2660 m/s found for the two bar impacts using the data from the gage on the SiO₂ bar and that on the PMMA bar. These two velocities

values are remarkably close to 2680 m/s which is the reported longitudinal sonic velocity for PMMA. (The longitudinal velocity represents greatest sonic propagation velocity possible.) The velocities found for the pulse peak and the descending portion more closely approach the reported extensional velocity 1840 m/s. The internal consistency of this body of data is supportive of the hypothesis of an underlying physical basis. The reason that the exponents n should depend on position in the way noted follows from the following plausibility argument.

We assume that the effects of dispersion, whatever their origin, are cumulative and that all parts of the impact bar are equivalent in their dispersion characteristics, and that the effect of dispersion can be determined by convolution. Recalling Eq. 2.1, if $F(t)$ is the original signal, and $G(t)$ is its form after travelling in a dispersive medium, then

$$G(t) = \int_0^t F(\tau) H(t-\tau) d\tau \quad (\text{Eq. 2.1})$$

where H is a function that contains the dispersion characteristics.

Consider the asymptotic representation of the pulse at *small values of elapsed (local) time* to be given by

$$F_{15}(t) = K_{15} t^4 \quad (\text{Eq. 5.3})$$

and

$$F_{30}(t) = K_{30} t^{6.3} \quad (\text{Eq. 5.4})$$

where the subscripts refer to the sensor location in cm and K is a constant. Thus, in the sense just discussed for purposes of Eq. 2.1

$$F(t) = F_{15}(t) \quad (\text{Eq. 5.5})$$

and

$$G(t) = F_{30}(t) \quad (\text{Eq. 5.6})$$

Dropping the proportionality constants one can write

$$F_{30}(t) = F_{15}(t) t^{2.3} \quad (\text{Eq. 5.7})$$

This result would have resulted from convolution provided $H(t)$ proportional to $t^{1.3}$, at least for small t . By inspection one can see that the effect of $H(t)$ is to multiply $F(t)$ by $t^{2.3}$ when the sensor location is moved 15 cm away from the source. This indicates one can write generally

$$G(t) = F(t) t^{2.3} \quad (\text{Eq. 5.8})$$

for any such shift. Conversely this can be written

$$F(t) = G(t) t^{-2.3} \quad (\text{Eq. 5.9})$$

which states that the signal 15 cm towards the source has the functional behavior of the local pulse divided by $t^{2.3}$. Thus, if the signal at the first gage is given by Eq. (5.3), then the signal at the end of the bar is

$$F_0(t) = K_{15} t^4 t^{-2.3} = K_{15} t^{1.7} \quad (\text{Eq. 5.10})$$

However, the impacted surface of the specimen is 1.2 cm from the end of the bar so that the exponent at the site of the impact would be expected to be less than 1.7. It was probably not a coincidence that in the two bar collision experiment, in which the power dependence on t of the initial pulse was 1.5, the pulse observed at the first gage had an exponent of 4. The Hertz elastic model Eq. 1.1 which predicts a 1.5 exponent dependence on penetration depth, is expected to remain approximately valid for visco-elastic materials. Therefore, a constant value of 4 for the exponent n at the 15 cm gage location, and of 6.3 at the 30 cm location is not only predicted but demanded by convolution. This completes the arguments in support of the universality, constancy and validity of the empirically noted pulse behavior.

Although the convolution procedure is valid for computing the subsequent pulse shape (because in this case the process leads in a higher power dependence on t), the inverse is mathematically undefined. Nevertheless, Eq. 5.9 does provide a rationale for deducing at least what the leading edge behavior must have been at some prior time and location. We shall use the principle contained in Eq. 5.9 as one of the foundation elements in transporting a pulse backwards in time, i.e. to correct it for dispersion.

5.4.2 Operational Procedure

The primary assumptions for reconstructing the original pulse from the observed impact pulse data are (1) that the power law description of Eq. 5.2c remains valid for describing the shape of the pulse up to its maximum, (2) that the propagation velocities determine the time shift of the position of the peak relative to the start of the pulse, (3) that the change in the shape of the leading edge is given by the prescribed change in the power dependence on t , and (4) that conservation of momentum defines the amplitude scale of the initial pulse.

Because the dependence of the leading edge shape on t increases by a power of 2.3 for a 15 cm length of bar travel it follows that the power increase is proportional to distance at the rate $\beta = 2.3/15$ per cm. Thus, if the observed initial power dependence at the first sensor is n_{15} then the assumed dependence at the site of the impact, 16.2 cm forward of the sensor is

$$n_0 = n_{15} - \beta \cdot 16.2 \quad (\text{Eq. 5.11})$$

The difference between the propagation velocity at the leading edge v_0 and the pulse maximum v_m leads to a progressive stretching of the pulse. Defining the period $\Lambda(x)$ of the pulse as the interval from the start to the peak at a location x cm from the impact site, then at the first sensor location the period is given by:

$$\Lambda(16.2) = \Lambda(0) + 16.2 \cdot \left(\frac{1}{v_m} - \frac{1}{v_0} \right) \quad (\text{Eq. 5.12a})$$

or

$$\Lambda(0) = \Lambda(16.2) - 16.2 \left(\frac{1}{v_m} - \frac{1}{v_0} \right) \quad (\text{Eq. 5.12b})$$

This new value of the exponent n_0 from Eq. 5.11 is inserted into Eq. 5.2c, in place of n . The corresponding value of m is determined by the two requirements that at the pulse maximum, i.e. $S = 1$, the slope must not only be zero but the curvature (second derivative) must be continuous with that on the descending part of the pulse.

This leads to the relationship

$$\frac{n + m - 1}{\Lambda(16.2)^2} = \frac{n_0 + m_0 - 1}{\Lambda(0)^2} \quad (\text{Eq. 5.13})$$

which in turn defines the value of m_0 to be introduced into Eq. 5.2c. This result assumes that the velocity over the descending slope is nearly constant over its span, so that the change in shape was neglected.

In synthesizing the calculated impact pulse at the specimen surface, the time scale is reintroduced into Eq. 5.2c by use of

$$t = S \cdot \Lambda(0) \quad (\text{Eq. 5.14})$$

The descending portion is then joined to the ascending portion by assuming that the velocity varies linearly between that at the peak and that the zero crossing locations. The error, such as shown in Fig. 5.3A between the modelled portion of the pulse, and the experimental data is added back onto the translated pulse at the new time positions determined by Eq. 5.14. In this way the "fine structure" of the experimental data is preserved. This defines the corrected pulse shape in terms of amplitudes relative to the peak amplitude. The absolute amplitude is fixed by introducing a multiplier into Eq. 5.1 to satisfy the condition of conservation of momentum.

The procedure as outlined is equally applicable to any shift in the pulse detection site. Thus, the pulse data obtained at the second sensor location can be used to compute the pulse shape expected at the first sensor.

Two computer programs were written to perform the pulse correction. The first one was to provide an accurate empirical description of the observed pulse. The second uses that description to "translate" the pulse forward in time and position to the site and time of the impact.

The first program takes the assumed functional form of the data and determines the values of the adjustable parameters which minimize the error between the function and the data. The function used was:

$$y = 0 \text{ for } t \leq t_0$$

$$y = y_{\max} (mS^n - nS^m)/(m - n) \text{ for } t > t_0$$

where

$$S = (t_{\max} - t)/(t_{\max} - t_0)$$

This function is recognizable as Eq. 5.2c in which y is the pulse amplitude, y_{\max} is its maximum value, and t_{\max} is the time at which the maximum occurs. These values are fixed by reference to the data. The computer determines the values of n , m , and the pulse start time t_0 that best fit the data. The procedure requires that initial estimates of n , m , are to be supplied. However, the answers obtained in some cases depended on the initial estimates. Furthermore, a range of combinations of n and m led to equally good fits, as judged by the total RMS error. For example by treating n as a fixed quantity the residual error at the best values of t_0 and m could be determined. This error was relatively unchanged if n was varied by as much as several tenths. A value of $n = 4$ for the data recorded at the 15 cm gage and $n = 5.3$ for the data from the other location appeared to be near the center of gravity of n values that satisfied to

error minimization criterion. These values of n are compatible with those deduced by the graphical scheme based on Eq. 2.5, i.e. finding an inverse power of strain that behaves linearly with time at small strain levels. Furthermore, these values of n are also compatible with $n = 1.5$ at the site of the impact. While this latter condition is not an absolute criterion it was the behavior noted in the two-bar collision experiments. In any case, variations in the exponent of a few tenths in the observed signal are not experimentally significant.

Therefore, the procedure finally adopted was to fix the values of n at 4 and 6.3 for the two gage positions, and to determine the value of m and t_0 by the error minimization procedure.

The second computer program uses these values of t_{\max} , y_{\max} , t_0 , n , and m along with the time t_{00} of the first zero crossing and incorporates them into Eqs. 5.12b, 5.13, 5.14, and then adds back in the residual error terms. This procedure results in the deduced shape of the initial pulse in terms of a peak normalized strain. The absolute strain values are separately determined by application of the conservation of momentum requirement Eq. 5.1 as discussed.

5.5 Results of Pulse Correction Procedure

The procedures described in 5.4 were applied to the pendulum impact data as well as to the gas gun impact data. There were two independent techniques for estimating the arrival time t_0 of the pulse leading edge. The one based on the n th root plotting procedures discussed in 5.1 is designated as $t_{0,g}$ and is determined by graphical extrapolation. The other relies on the best least square error fit to Eq. 5.2c which has also been described and leads to the estimate $t_{0,c}$. Each approach has limitations. Table 5B summarizes the parameters that characterize the pulses as observed prior to correction. There is no pendulum data for the 30 cm gage as that gage had not yet been installed at the time of those measurements. The pulse maximum relative to both $t_{0,g}$ and $t_{0,c}$ are included.

In order to test how well the correction procedure was performing, it was first applied to the data from the 30 cm gage and used to deduce the expected pulse shape at the 15 cm gage position. This deduced translated pulse could then be compared with that experimentally detected by the 15 cm gage. These results are given in Table 5C. Two representative plots which compare the calculated signal with the observed one are given in Figs. 5.5 A and B. These curves are somewhat misleading in that the procedure actually matches the curves at the position of their peaks, whereas in the figures the position of the leading edges are made to coincide. However, this way of plotting emphasizes how well the pulse periods match. It is the period that is especially important to the analysis of the data.

Finally, the pulse data from the 15 cm gage position is translated to the site of the impact by the computational procedure. These results are given in Table 5D. The figures of the corrected pulses are presented in Chapter 6 in conjunction with the computations based on the corrected pulse. Meaningful discussion of the deduced pulse shapes is not possible until the derived responses as a function of penetration depth have been determined.

Table 5B
PARAMETERS CHARACTERIZING OBSERVED PULSE
AT 15 cm AND 30 cm GAGES

Specimen Designation	Specimen Material	Impact Velocity	15 cm gage					30 cm gage				
			$(t^* - t_{o,g})$	$(t^* - t_{o,c})$	$(t_{oo} - t_{o,g})$	n	m	$(t^* - t_{o,g})$	$(t^* - t_{o,c})$	$(t_{oo} - t_{o,g})$	n	m
180P1	PMMA	126.2	33.9	32.17	47.98	4	4.85	53.3	53.0	69.8	6.3	6.35
190P1	PMMA	128.1	33.7	32.35	47.95	4	5.05	54.6	53.4	71.0	6.3	6.50
190P2	PMMA	219.9	34.2	32.26	48.5	4	5.11	52.6	53.2	69.4	6.3	6.36
190P3	PMMA	218.7	33.7	31.17	47.75	4	4.39	54.3	53.0	70.8	6.3	6.30
190C1	PC	124.5	41.1	40.64	55.66	4	7.90	59.8	58.1	76.0	6.3	6.81
190C2	PC	125.9	40.9	40.19	55.77	4	7.82	59.0	56.6	75.4	6.3	6.35
190C3	PC	221.5	42.6	39.78	57.87	4	6.52	65.5	58.0	83.0	6.3	6.48
190C4	PC	219.9	41.95	40.18	56.96	4	7.11	61.3	57.1	77.2	6.3	6.30
827P1	PMMA	2.08	153			4	4					
827P2	PMMA	2.08	154.5			4	4					
827C1	PC	2.08	220			4	4					
827C2	PC	2.08	226			4	4					

t^* = time at pulse maximum

$t_{o,g}$ = pulse arrival time determined graphically

$t_{o,c}$ = pulse arrival time using computer error minimization procedure.

Table 5C
COMPARISON OF OBSERVED PULSE PARAMETERS AT 15 cm GAGE
WITH VALUES COMPUTED FROM DATA AT 30 cm GAGE

Specimen Designation	Pulse Parameters					
	$t^* - t_{o,c}$		$t_{oo} - t_{o,c}$		m	
	Calc.	Obs.	Calc.	Obs.	Calc.	Obs.
180P1	34.1	32.2	46.9	48.0	4.16	4.85
190P1	34.6	32.4	47.5	48.0	4.29	5.05
190P2	34.3	32.3	47.3	48.5	4.18	5.11
190P3	34.1	31.2	47.3	47.8	4.12	5.39
190C1	39.3	40.6	52.7	55.7	4.90	7.90
190C2	37.8	40.2	50.9	55.8	4.46	7.82
190C3	39.2	39.8	53.5	57.9	4.66	6.52
190C4	38.3	40.2	52.2	57.0	4.46	7.11

Table 5D
DEDUCED PULSE PARAMETERS AT SITE OF IMPACT
CALCULATED FROM DATA AT 15 cm GAGE

Specimen Designation	Impact Velocity	Impact Parameters			
		$t^* - t_0$	$t_{90} - t_0$	n	m
180P1	126.2	10.95	20.95	1.5	1.48
190P1	128.1	11.13	21.15	1.5	1.58
190P2	219.9	11.04	21.41	1.5	1.58
190P3	218.7	9.95	20.37	1.5	1.18
190C1	124.5	19.42	30.20	1.5	4.76
190C2	125.9	18.97	29.76	1.5	4.60
190C3	221.5	18.56	30.05	1.5	3.74
190C4	219.9	18.96	30.29	1.5	4.18
827P1	2.08	130.2	-	1.5	7.7
827P2	2.08	131.7	-	1.5	7.7
827C1	2.08	201.4	-	1.5	8.9
827C2	2.08	207.4	-	1.5	8.9

6. DERIVED RESPONSE OF PMMA AND PC TO FREE FLIGHT IMPACTS

The corrected pulses can be kinematically analyzed, using the procedures given in the Appendix to deduce the penetration distance of the projectile into the target as a function of time. Once this relationship is known, computation of the resisting force as function of depth, time, or instantaneous velocity among other qualities can be performed easily. The analysis also allows the energy contained in the propagating pulse to be independently calculated. Thus, by difference the energy that remains local to the impact can be calculated. These results can then be compared with the prior mechanical test machine data, as well as with theoretical and intuitive expectation. The derived results for PMMA and PC follow.

6.1 Analysis of PMMA Data

The analysis of the results of the pendulum impacts at 2.06 m/s and of the gas gun impacts at 125 m/s and 220 m/s are given in Figs. 6.1 A-F. In order to show the degree of reproducibility the results of the duplicate runs are superimposed. Some of the major characteristics are summarized in Table 6A. The circles in Fig. 6.1 B are the values observed at 5 mil (.13 mm) penetration depth in our prior work using the electro-hydraulic test machine at a constant indentation velocity of .25 and of 2.5 m/s. In Fig. 6.1 D and F the curves obtained in this prior work are shown. In addition the force-penetration behavior is shown in Fig. 6.1 G, in which the results for the three velocities are compared. The prior result obtained at the 2.5 m/s using the electro-hydraulic machine are included for reference.

Table 6A
SUMMARY OF IMPACT RESULTS FOR PMMA

Run No.	Velocity m/s	K_0 $10^5 \text{ lb/in.}^{3/2}$	E GPa/m ²	Max Depth		Max Force		% Local Work Recovered
				mils	mm	lbs.	kg	
827P1	2.08	3.65	5.24	6.7	.170	155	70.5	56.1
827P2	2.08	3.52	5.05	6.8	.173	155	70.5	56.0
	2.08	3.59	5.15	6.8	.172	155	70.5	56.1
180P1	126.1	4.30	6.17	37.9	.963	1220	555	26.0
190P1	128.1	4.19	6.01	39.4	1.000	1210	550	24.7
	127.1	4.25	6.09	38.7	0.982	1215	553	25.4
190P2	219.9	3.28	4.71	71.1	1.803	1900	864	14.7
190P3	218.7	5.57	8.00	64.3	1.633	1910	868	14.1
	219.3	4.43	6.36	67.7	1.718	1905	866	14.4

The data and results for the duplicate pendulum impact runs are almost identical. The greatest discrepancy between duplicate runs is for the 220 m/s experiments. The reason for the differences in the latter case is traceable to the 1.09 μs difference in their measured periods (the time interval between the pulse leading edge and the maximum). Such a difference in the measured period is to be expected when one considers that the data is sampled at 0.5 μs intervals and that the start of the observed pulse is buried in the noise signal. This example illustrates the importance of being able to

define the start of the pulse signal. Because the period is much longer in the case of the pendulum impacts, an error of this magnitude has a smaller relative effect.

The force-displacement curves in Figs. 6.1 D and F are bracketed by the prior test machine results at 0.25 and 2.5 m/s, and the present results at 2.08 m/s in Fig. 6.1 B lie below the prior results at the 5 mil penetration check point. The possible significance is discussed in 6.3. Fig. 6.1 G gives little indication of a velocity dependence, within experimental error. This is confirmed in Table 6A, in which the proportionality constant K_0 of Eq. 1.1, and the derived Young's modulus E are displayed. A possible slight trend towards increasing stiffness with increasing velocity is calculated. However, there is a marked decrease with increasing impact velocity in the amount of energy returned to the projectile on rebound from energy that was imparted to specimen in the locale of the impact.

6.2 Analysis of the PC Data

The results for the impact measurements on PC are treated in parallel to those of PMMA and are shown in Figs. 6.2 A-G and in Table 6B. The general features of the two materials are similar. However, in the case of PC there appears to be a progressive decrease in stiffness as the velocity increases. Figure 6.2 B shows that the force at the 5 mil depth value in the pendulum impact measurements at 2.08 m/s is close to that observed using the test machine at 0.25 m/s. Again there is a greater discrepancy relative to the machine result at 2.5 m/s. However, the results for the 125 m/s and the 220 m/s impacts show increasing departure from the machine base line results.

Table 6B
SUMMARY OF IMPACT RESULTS FOR PC

Run No.	Velocity m/s	K_0 $10^5 \text{ lb/in.}^{3/2}$	E GPa/m^2	Max Depth		Max Force		% Local Work Recovered
				mils	mm	lbs.	kg	
827C1	2.08	1.46	2.10	10.3	.262	114	52.5	53.0
827C2	2.08	1.27	1.82	10.9	.277	111	50.5	52.1
	2.08	1.37	1.96	10.6	.270	113	51.2	52.6
190C1	124.5	0.42	0.61	70.6	1.793	877	399	19.8
190C2	125.9	0.44	0.63	70.1	1.781	890	405	18.7
	125.2	0.43	0.62	70.4	1.787	884	402	19.3
190C3	221.5	0.25	0.36	126	3.20	1390	632	10.3
190C4	219.9	0.31	0.45	128	3.25	1400	636	10.9
	220.7	0.28	0.41	127	3.23	1395	634	10.6

This is especially evident in Fig. 6.2G.

The table shows the same trend in the computed values of K_0 and E . In fact the calculated Young's modulus at 220 m/s is almost a factor of 5 less than that of 2 m/s. This decrease of stiffness is reflected in the large calculated maximum penetration depth. Similar to PMMA there is a large decrease in the amount of the local work recovered as the impact velocity is increased. Finally the table also shows the generally good agreement between duplicate runs.

6.3 Discussion of Results

The results show that neither PMMA nor PC show any particular trends towards increased brittleness as should be evidenced by an increase in modulus and a decrease in the viscous/anelastic contribution. The PMMA specimens showed radial crack formation at 220 m/s, but not at 125 m/s. There is nothing evident in the curves to suggest that such a threshold should occur at that location. In fact there is a clear trend with increasing velocity in both polymers to retain increasingly more of the local energy, rather than to release it elastically to the projectile. Hence, instead of non-elastic processes being frozen out as the time scale decreases, these processes appear to be enhanced.

The behavior of PC in actually displaying a decrease of stiffness with increasing impact velocity is even more unexpected. One possibility is that local heating due to the impact may soften the material. However, this can be dismissed as unlikely by the following argument:

The projectile's kinetic energy of which 90% remains with the specimen is 9J at 220 m/s. The penetration is about 3.2 mm so that a crater volume of 0.04 cm^3 is produced and a plastic zone of 10 times this volume results. Thus, the maximum temperature rise over this volume is about 20°C if all of the energy were converted to heat. Even this extreme estimate is not sufficient to heat the PC to its glass transition. Thus, only secondary effects due to a much smaller thermal rise are likely to occur.

Another possibility is that the non-linear stress-relaxation process (see Eq. 1.5) may dominate over the usual expected kinetic dependence. The stress-relaxation model is considered in the next chapter. In any case whereas PMMA is displaying "normal" behavior based on conventional wisdom, PC seems to be behaving anomalously, but in a mode favorable to good impact resistance.

Finally, we consider the possible reasons why our present results give forces at a given depth that are less than those previously measured at 2.7 m/s on the electro-hydraulic equipment. This comparison may indicate a real systematic difference between the two methods such as due to the methods of supporting the specimens. Another possibility is that "ringing" or some other phenomenon in the electro-hydraulic sensing systems may be responsible. At 2.5 m/s that equipment was being used at the upper limit of its capability, where it is known that such complications can begin to have an effect. The data that we had obtained on that machine showed a somewhat larger than expected increase in stiffness when the velocity was increased from 0.25 m/s to 2.5 m/s relative to the data at 0.25 m/s and less. To what extent, if any the source of the discrepancy is attributable to the electro-mechanical machine would have to be resolved by future experimentation. In any case the present results are in good agreement with the prior one at 0.25 m/s. It is also important to keep in mind that velocity is not constant in the present experiments so that the results are not directly comparable. However as Fig. 6.3A shows for the example of the 220 m/s impact velocity using a PC target, the velocity remains constant to within 10% over the first half of the penetration.

7. VISCO-ELASTIC MODEL OF POLYMER IMPACT BEHAVIOR

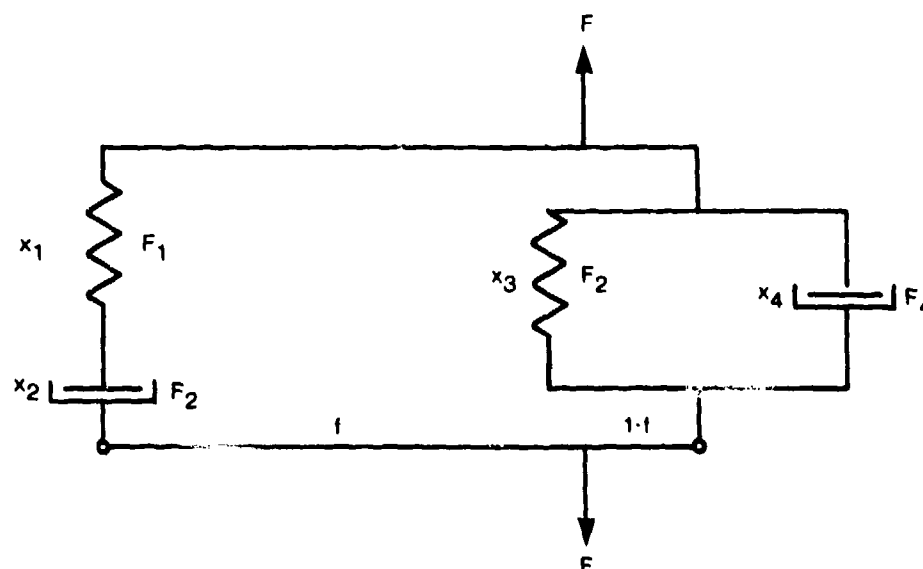
The major features of the polymer response noted in this study indicates (1) the maximum reaction force precedes the maximum penetration depth, (2) the change of load with penetration distance is more pronounced during projectile exit than on entry, (3) the load on exit drops to zero when the penetration depth is an appreciable fraction of the maximum depth, and (4) most of the local energy absorbed by the impact is retained at the time of exit. To this behavior should be added such prior observations as (5) yielding densification occurs during the projectile entry under the impact site, (6) a strain-rate and history-dependent stress relaxation accompanies the strain process, and (7) over many decades of velocity there is a trend towards a net hardening with increased penetration rate. The latter observation appears to have been reversed by PC at penetration rates of about 2 m/s and greater.

Even though the separate phenomena themselves are complex, it is instructive to consider how they may be interrelated. Accordingly a relatively simple conceptual model has been formulated to try to connect the processes (5)-(7) so as to qualitatively predict or explain the present results (1)-(4). The model uses simple mechanisms with the objective of gaining insight into the individual differences in the impact behavior of PC and PMMA.

Briefly the penetration is assumed to result in elastic and viscous deformation. The viscous flow that occurs is ultimately recoverable upon annealing and, therefore, is really an anelastic response. The polymers are conceived as being a collection of intertwined, snarled springs embedded in a viscous matrix. The viscous and the elastic reaction forces to an applied load are partly in parallel and partly in series. As deformation occurs, accompanied by some alignment, the mix of parallel to series response can change. Finally, the viscosity of the matrix itself is history dependent, but is otherwise Newtonian. The resistance to the sphere penetration is partly due to a Stokes-like viscous resistance, and partly to a Hertz elastic response. This leads to a net force vs. penetration relationship which in turn is velocity and time dependent. The details and results are discussed next.

7.1 Details of the Model

The elastic and viscous response is considered to be connected by the spring-dashpot system shown below. This system differs from the more conventional



models in that the left hand series arrangement and the right hand parallel arrangement are connected by a hinged bar so that each sub-system contributes separately to the total response. By placing the compressive load a fractional distance f along the bar, the response will be f parts parallel and $(1-f)$ parts series. The two dashpots represent the viscous response of the same polymeric material, and are, therefore, assumed to behave identically. Similarly the springs are assumed really to be a single spring which in total force is Hertzian with respect to total elastic penetration, but the force is split between the two modes of material behavior.

In following expressions, the subscripts refer to the system element defined by the figure. The subscript zero refers to the quantities as measured at the point of application of the force, i.e. at the projectile. Force is F , displacement x , and the time rate of displacement is given by the superscripted dot notation. The variables are F , x , and \dot{x} at each of the five locations, so that 15 equations are needed to define the values. However, by definition $F_1 = F_2$, $x_3 = x_4$, and $\dot{x}_3 = \dot{x}_4$, and we can consider x_0 and \dot{x}_0 as known, from the solution of the equation of motion for the projectile. Therefore, 10 equations suffice. Designating the dashpot resistance by μ , the spring constant by κ and the fraction parallel by f , these are:

$$\begin{aligned}
 (a) \quad F &= F_1 + F_3 + F_4 \\
 (b) \quad fF_1 &= (1-f)(F_3 + F_4) \\
 (c) \quad x &= (1-f)(x_1 + x_2) + fx_3 \\
 (d) \quad \dot{x} &= (1-f)(\dot{x}_1 + \dot{x}_2) + f\dot{x}_3 \\
 (e) \quad F_2 &= \mu\dot{x}_2 \\
 (f) \quad F_4 &= \mu\dot{x}_4 \\
 (g,h,i) \quad x_i &= \int_0^t \dot{x}_i dt \quad i = 1, 2, 4 \\
 (j) \quad F_1 + F_3 &= \kappa[(1-f)x_1 + fx_3]^{3/2} \\
 (k) \quad F_1 &= \kappa[(1-f)x_1]^{3/2}
 \end{aligned}
 \tag{Eq. 7.1}$$

or

$$\approx \left(\frac{3}{2}\right)\kappa(1-f)x^{1/2}x_1 \text{ for } f \approx 1$$

Equation (a) is simply the balance of forces; (b) is the balance of moments and is needed to satisfy conservation of energy; (c) and (d) are geometric requirements; (e) and (f) are the dashpot responses; (g,h,i) are obvious; (j) represents the force of the non-linear Hertzian spring in which the *total* elastic force is assumed to be determined by the *total* elastic displacement as measured at the ball; (k) is an approximate expression for the series elastic force. The constant κ can be identified with K_0 of Eq. 1.1.

The dashpot constant μ can be defined via the hydrodynamic law for the motion of a sphere through a viscous medium:

$$\text{Force} = 3 Ux\dot{A}/2R\Phi \tag{Eq. 7.2}$$

in which ϕ is fluidity, U the velocity of the sphere of radius R relative to the fluid and A the surface area, and the force is applied in the direction of motion. This equation is valid for portions of a sphere assumed to be in an infinite medium. For the present case, the term R can be interpreted as a boundary layer and will be replaced by the distance from the ball surface to the boundary of the plastic or densified zone. Since μ is force/velocity, and since $A = 2\pi Rx$, Eq. 7.2 can be written as:

$$\mu = 3\pi Rx/\Phi R_2 \quad (\text{Eq. 7.3})$$

where R_2 is the boundary layer thickness. The fluidity is strain-rate dependent and will be treated later.

The computational procedure is to assign the proper material parameters to κ and μ , assume a value of f , given an initial impact velocity. At each time increment an updated value for x , and μ are computed. The above system of equations are solved to finally yield the reaction force at that instant of time. This determines the deceleration and allows the next increment of x to be computed. As this process continues, the projectile stops and changes direction, being propelled by the residual energy in the springs. During this process, the dashpot in the series arm is constantly relaxing, so that this portion of the energy is not recovered. Similarly the dashpot in the parallel arm inhibits the release of energy from its spring so that not all of that stored energy is available to the projectile during its rebound trajectory. It should be noted that this computational scheme is approximate and that the results can exhibit artificial irregularity.

7.2 The Time Dependence of the Fluidity

In our prior work a model was proposed to account for the following experimental load relaxation law

$$F(t) = F(0)(1 + At)^{-B} \quad (\text{Eq. 1.5})$$

This law was observed when the penetration rate was abruptly changed from a constant velocity to zero. In addition, the model qualitatively accounted for the increases and decreases in compliance when the penetration rates were abruptly changed.

The elements of the model are:

1. There is a residual intrinsic fluidity ϕ_0 in the fully annealed, unstrained polymer.
2. Fluidity can be increased by increasing the volume concentration of unpinned sites. The polymer is envisioned as being tangled, and that unsnarling, or freeing the polymer chain allows relative motion to occur.
3. The unpinning is facilitated by straining the polymer, which is expected to align the molecular segments by stretching or shearing.
4. Unpinning is a cooperative process and is made easier by prior unpinning.
5. There is a spontaneous tendency of the molecules to rekink. This is a first order reaction and the rate is proportional to the mobility of the system, i.e. to fluidity.

This results in the following system of equations:

$$\Phi = \Phi_0 + n\phi\zeta \quad (\text{Eq. 7.4})$$

$$\dot{\zeta} = b\epsilon\zeta(1 - \zeta) - c\Phi\zeta \quad (\text{Eq. 7.5})$$

in which n is the volume density of potentially unpinnable sites, ϕ is the fluidity con-

tribution per site, ζ is the fraction of unpinned sites, b is a constant reflecting the efficiency of the unpinning process, c is a rate constant for the decay of the pinned site population, and $\dot{\epsilon}$ is the applied strain rate.

Below the glass transition temperature, one expects ϕ_0 to be very small. Therefore, taking the time derivative of Eq. 7.4 and inserting 7.5 gives

$$\dot{\Phi} = bn\phi\dot{\epsilon}\zeta(1 - \zeta) - cn\phi\zeta^2 \quad (\text{Eq. 7.6a})$$

$$= \alpha\Phi - \beta\Phi^2 \quad (\text{Eq. 7.6b})$$

in which

$$\alpha = b\dot{\epsilon} \quad (\text{Eq. 7.6c})$$

and

$$\beta = c + (b\dot{\epsilon}/n\phi) \quad (\text{Eq. 7.6d})$$

Finally we can relate $\dot{\epsilon}$ to \dot{x}_2 and \dot{x}_3 in the spring-dashpot model of the preceding section, by $\dot{\epsilon}_1 = \dot{x}_1/R_2$.

At steady state $\dot{\Phi} = 0$, or

$$\Phi_{ss} = \alpha/\beta \quad (\text{Eq. 7.7})$$

The values for the constants can be determined from the experimental values observed for the load relaxation law.

For the case of a pure series arrangement, it was previously shown that

$$F = K\epsilon \\ = J\dot{\epsilon}/\Phi$$

in which $K = AE$ and $J = 3A/2$. This finally led to

$$c = 2E/3B$$

in which B and c are the constants in Eq. 1.7, and 7.6d respectively, and E is Young's modulus. It can be shown that as long as the fraction of unpinned sites to pinned sites is small, as is expected to be the case, then the term in parentheses in Eq. 7.6d can be neglected, or

$$\beta \sim 2E/3B \quad (\text{Eq. 7.8})$$

Similarly the prior work showed that under the same approximate conditions,

$$A = \Phi_{ss}c$$

which upon introduction of 7.8 and 7.7 leads to

$$\alpha \sim A, \quad (\text{Eq. 7.9})$$

in which A is an experimentally measured quantity, itself a function of indentation velocity.

These relationships can then be introduced into the computation scheme outlined

in the previous section. In this way, by introducing the dependence of A on velocity, and through the use of Eq. 7.6b, the fluidity is made history and time dependent.

7.3 Discussion of Input Data and Procedure

In order to carry out the computations specific values must be designated for the Young's modulus E , the ratio λ of the densified zone relative to the displaced volume, the values of A and B appropriate for the relaxation law Eq. 1.7, and the fraction f of parallel-like behavior in Eq. 7.1a-j.

Previously, the size of the densified zone in PC was found to be independent of velocity. We assume this is also the case for PMMA. Therefore, those values of λ for PC and PMMA of 3.6 and 6.2 respectively were introduced into the model for the 220 m/s impact by a 4.5 mm steel ball.

In our prior work the observed relaxation behavior was studied in detail using the mechanical test machines. These results showed that B is relatively insensitive to velocity u , whereas A is nearly proportional to u . Therefore, it is convenient to define A_0 as

$$A_0 = A/u$$

where A_0 has the dimensions of an inverse length, but may be a weak function of velocity. Both A_0 and B are functions of depth as well. The values for A_0 and B were obtained for PMMA over a 5 decade span of velocity. However, that range was, nevertheless, 4 decades of velocity below that of our current work. The corresponding data for PC is less complete and exhibits more scatter. However, there appears to be a regular trend in the product (AB) to increase approximately linearly with the logarithm of velocity. Because it is the product AB that defines the steady state fluidity, we somewhat arbitrarily fixed B at the experimental values obtained at low velocities and considered A_0 to be velocity dependent. The values of B used in the computations were

$$B = 0.05 + 0.05\sqrt{X/R} \quad \text{for PMMA}$$

and

$$B = 0.025 + 0.03(X/R) \quad \text{for PC}$$

where the approximate dependence on penetration depth X is taken into account.

The Young's modulus E is also expected to be velocity dependent. One expects a priori that E should increase slowly with increasing velocity to some ultimate upper bound plateau. Apparent values are available from the results of the previous chapter. In the case of PC the velocity dependence of the calculated modulus was anomalous. Therefore, it was of interest to find out if the behavior of PC could be attributable to the velocity dependence of A_0 or to the balance between series and parallel behavior as measured by f .

The approach was to consider λ and B as fixed known quantities, and A_0 , E , and f as quantities to be determined from the experimental pulse data for PC and PMMA.

Ideally, the pulse computed by this model should match the experimental pulse everywhere. In practice, the most important details to be matched are the initial force dependence at the start of the pulse, the magnitude and time position of the peak, and the exit time and exit velocity of the projectile. If f , E , and A_0 remain constant during an impact, the initial force behavior is determined mainly by E . Therefore, there

is little latitude in adjusting the value of the modulus. However, f and A_0 have largely compensating effects on the pulse shape. Increasing f tends to increase the stiffness of the system, to increase the peak force, to shorten the time to reach the maximum and to exit, and usually to increase the exit velocity. Similar effects result from decreasing A_0 . If the peak force is held constant by applying compensating changes in A_0 and f , then the effect of decreasing A_0 is to shift the peak to shorter times, to reduce the maximum penetration depth, to extend the exit time and increase the exit velocity, and to decrease the depth of the impact crater at exit. This array of consequences due to just two parameters A_0 and f is not necessarily compatible with improving the overall match between the modelled result and the experimental values.

7.4 Computational Results

The expected responses of PC and PMMA when impacted by a 4.5 mm steel ball at 220 m/s have been calculated using the preceding model. Some representative "best fits" are given in Table 7A for these two materials, using several combinations of the impact variables. The calculated results in terms of penetration depth, and local energy were plotted in the same manner as were the experimental pulse data in Figs. 7.4 A and B for PC and Figs. 7.4 C and D for PMMA. Comparison with the experimental data is shown. The force-time results for PMMA can be seen to correspond qualitatively with the experimental results, except that the calculated pulse is skewed towards longer times. The calculated pulse shape for PC is similarly skewed but drops precipitously on the descending limb. These curves for PC and PMMA correspond to the columns labelled Case 2 in Table 7A.

The most difficult characteristics to satisfy were the time, velocity, and penetration depth at exit. As the table shows the fit in the case of PC in regard to exit velocity is rather poor. However, the computer program is somewhat unstable in the descending region when f is close to one. Thus, the computed exit velocity is not completely reliable.

The results from the model suggest a rather different behavior between PC and PMMA. The former has a much smaller Young's modulus and exhibits a nearly pure parallel-like behavior with a relatively fluid damping component. The PMMA has a more than 10-fold larger Young's modulus, responds in a series-like fashion but with a more viscous damping component. These differences appeared to persist over all of the variations of the parameters examined to try to match the modelled pulse shape to the experimental data.

If the assumed modulus for PC were increased to a level more like that for PMMA, the fit at the initial stages of penetration was quite poor. However, if f were to be allowed to decrease with increasing time or penetration depth, it may be possible to reproduce the experimental curve. This complicates the model. However, there is no a priori reason to accept or reject this additional degree of freedom.

The model, while conceptually simple, is computationally complex. The computer solution at times is not adequately damped and takes on an oscillatory character or even instability. This could be remedied by developing a better algorithm. The exit depth and velocity were the most difficult properties to try to match, without severely compromising the fit elsewhere.

In the case of PC a fixed value of f does not reproduce the descending region of the pulse well. However, in this case the computer solutions for high parallel contents tend to behave as noted. Until the model is more completely explored it is not clear

whether the problem in fitting the exit values is a weakness of the model itself, or an indication of the complexity of the material behavior. In the case of PMMA the descending region is modelled reasonably well by a single fixed value of f for the entire impact process.

The values of A_0 required to provide the best matches with the data are a factor of 2-5 greater than would be expected from a simple linear extrapolation. (In the case of PC the extrapolated value is about 1500 and for PMMA about 220.) If the values deduced from the model are significant, then these should provide a basis for a priori impact response predictions at both lesser and greater velocities than used in the present examples. This would provide an addition test of the validity and utility of the model.

Table 7A
COMPARISON OF CALCULATED AND OBSERVED PULSES FOR PC AND PMMA
RESULTING FROM IMPACT WITH 4.5 mm STEEL BALL AT 220 m/s

Parameter	PC			PMMA		
	Exptl	Model Case 1	Model Case 2	Exptl	Model Case 1	Model Case 2
Force at 2 μ s (lbs.)	82	130	104	716	690	685
Force at 5 μ s (lbs.)	324	367	330	1460	1580	1460
Max Force (lbs.)	1400	1390	1450	2030	2080	1990
Time at Peak (μ s)	17.6	21	20	9.2	10	10
Max Penetration (Mils)	120	124	121	61.7	63	71
Exit Time μ s	30	32	*	20	21	20.5
Exit Velocity m/s	67	121	*	77	112	86
Depth at Exit (Mils)	113	94	*	50	35	54
A_0 (cm^{-1})	-	3000	10000	-	400	3000
E (GP_a)	-	.52	.55	-	6	8.5
f (fraction parallel)	-	.82	.94	-	0	.25

8. DISCUSSION AND CONCLUSIONS

8.1 Discussion of Measurement and Analysis Procedures

A way to treat pulse data has been developed to deduce the details of the force response as the projectile penetrates the target. Although the methodology is derived from empirical observation, rather than derived from the exact theory, the procedure is consistent with, and in part determined by basic physical requirements. For example, the maximum rate of propagation of a sonic disturbance, enters into the formulation naturally, as does the normal rate of travel of plane waves in a long cylinder and the way the leading edge changes form as it travels.

The elementary theory, which assumes a single characteristic sound velocity, is adequate and useful when the period from the start to the peak of the pulse is long compared with the spread of arrival times of the components travelling at the different velocities. In the case of the 2.5 cm diameter PMMA impact bar used in this study, and the sensor located 6 diameters from the bar end, this time spread, due to the velocity differences, is about 20 μ s. Hence, if in a pulse with a period of ten times this value, this transient was not detected, or was ignored, the pulse could nevertheless be analyzed with less than a 10% error using the elementary theory. Such is the case for impacts of velocities below about 2 m/s. For higher velocities, a procedure such as that described in Section 6, is required.

The experimental measurements are straightforward. Part of the complications due to dispersion could be mitigated by the use of a bar of some other material. In studies of impact on materials other than polymers, this is a recommended choice. However, in the study of impacts on polymers, requirements of good acoustic impedance matching between the bar and the specimen necessitate using a polymeric bar. While increasing the magnitude of the corrections needed to deduce the true originating pulse, these complications remain manageable.

The amount of effort involved, and the way finally established to correct observed pulses of short duration was unexpected in as much as impact bar measurements are a common experimental procedure. Furthermore, the basic equations governing acoustic propagation are known as well as are Maxwell's equations in the area of classical electricity and magnetism. Nevertheless, the solution of the problem of leading edge behavior, is very complex. The functional forms that we observed experimentally are recommended to the theoretician interested in solving this leading edge problem. It may be that the pulse shape found and its mode of propagation are peculiar to the initial and boundary conditions of our particular experiment, in as much as the pulse was initiated essentially at a point on the center of the bar end in the present work.

The observed leading edge transient has the form

$$F(x,t) = Kt^{n+\alpha x} \quad (\text{Eq. 8.1})$$

where x is distance from the site of impact, K , n and α are constants, and t is local time measured from the first arrival of the pulse. This transient was assumed to be accommodated into the overall pulse by the equation

$$F = At^n - Bt^m \quad (\text{Eq. 8.2})$$

This may not be the best representation of the way the transient and the overall pulse geometries are related. A better description would require further investigation. Our justification was the excellent empirical fit found with our observed data. In any case

the deviations from this law were reinserted into the final result. In trying to determine the evolution of the pulse shape, a central assumption and requirement in our analysis was that once the pulse is created, its propagation is only a function of the bar. Thus, any artifacts that the procedure described in 5.4 introduces into the final results, should be independent of the target material or impact dynamics.

8.2 Discussion of the PC and PMMA Results

The impact results of the two materials show distinctly different trends. One may question how well the computed results reflect the true force-time-penetration relationships of the actual impact event. The results for PMMA were largely velocity independent, and were compatible with the prior results obtained on the electro-hydraulic test machine. Those for PC show a progressive softening with increasing velocity. The results for PC and PMMA using the pendulum impact method confirmed the prior test machine results at comparable velocity. In the case of the gas gun impacts the most sensitive factor affecting the results is the value of the computed time period after shifting the pulse. This value is in turn affected by the accuracy with which the period at the gage is determined, and by the velocity values used to effect the shift in shape and position.

The error in determining the period at the gage is mainly due to the error in detecting the position of the leading edge. The graphical procedure and the computer error minimization procedure often led to differences of several μ s. The error minimization was in principle the more objective measure, and was used to refine the graphical estimate. In spite of the high precision of the computed result, its reliability is estimated to be $\pm 1 \mu$ s. Such an error is insufficient to account for anomalous softening deduced from the PC results.

The other factor affecting the calculated shifted pulse period is the difference in the sound propagation velocities. Even if incorrect velocity values were used, they remained unchanged in the analysis process. Therefore, since the pulse period in PMMA is smaller than PC, there would be an even larger artifact produced in the former material. The only remaining possibility, if the softening effect were not real, is that the propagation velocity of the leading edge, or of other parts of the pulse were different for PC than for PMMA. This cannot be disproved, but certainly contradicts the principle that the pulse propagation in the bar depends only on the bar.

In summary, it appears that the increasing impact softening in PC with increasing impact velocity is real. Since elastic modulus is expected to increase with increasing velocity, the conclusion is that the viscous response of PC is becoming more pronounced. This would have a beneficial effect on enhancing the impact damage resistance of PC relative to PMMA.

8.3 Results of Model Calculations

The initial force-penetration behavior of PMMA, as well as the time and depth of the pulse maximum are well approximated by assuming the response to be predominantly a series arrangement of the elastic and viscous flow response. However, the behavior of PC is much more complex. This material is initially much softer than predicted on the basis of the expected continuing tendency of the elastic modulus to increase with increasing velocity. However, with deeper penetration the response stiffens. This can be reconciled with a predominantly parallel elastic-viscous element arrangement in combination with a greater dashpot fluidity.

However, this arrangement results in a very steep descending limit and a small rebound velocity. The response can only be made to conform more with experiment by an increasing shift to an increasingly series-like arrangement. This leads to the concept of PC behaving like an elastic skeleton of which the interstices are filled with a relatively mobile fluid. However as the strain level is increased, the elastic network breaks up. In terms of the model this requires that the parameter f decrease with increasing strain.

Such a mental picture would account for the decreasing modulus with increasing strain-rate (impact velocity) if the fraction of molecules associated with the elastic skeleton were to decrease with increasing strain rate. This is consistent with the time dependent fluidity model, in which we considered an unpinning to control fluidity. The greater the strain rate, the greater the degree of unpinning, according to Eq. 7.4 and 7.5. As long as the fraction ζ of unpinned sites is much less than unity, the unpinning would have no effect on the modulus. However, if ζ becomes large, then the remaining skeleton is weak and a decrease of elastic modulus is expected. According to Eqs. 7.9, and 7.6b, ζ will become large if the relaxation parameter $A = A_0 \times \text{velocity}$ is large. In the case of PC, the best estimates for A_0 were several fold greater than the values for PMMA.

This interpretation, while speculative, provides a possible explanation for the difference in behavior of the two polymers. It also suggests that one of the important variables affecting the resistance of a polymer is the A_0 parameter. Thus, it would be useful to understand in terms of the molecular structure how to modify this property. Finally, the relaxation model and the derivative impact model require considerable critical testing before they can be considered reliable guides to the behavior of real materials.

9. ACKNOWLEDGMENT

Dr. W. P. Minnear has been not only an active collaborator and close consultant in this work but has made many important and creative contributions to the experimental studies. Dr. G. M. Rowe has continued to be most helpful with much of the analytical and theoretical work. In addition, the author has benefited from the conversations and advice from many colleagues at the General Electric Research and Development Center. Finally, special appreciation is extended to Mr. C.F. Bersch for his continuing interest and encouragement during the course of the overall program.

10. REFERENCES

- [1] W. B. Hillig, "Impact Studies of Polymeric Matrices," General Electric CRD Report SRD-73-091, prepared under Contract N00019-72-C-0218 for Naval Air Systems Command, Dept. of the Navy, March 1973.
- [2] W. B. Hillig, "Impact Response Characteristics of Polymeric Matrices," General Electric CRD Report SRD-74-087, prepared under Contract N00019-73-C-0282, *ibid*, September 1974.
- [3] W. B. Hillig, "Impact Response Characteristics of Polymeric Matrices," General Electric CRD Report SRD-75-083, prepared under Contract N00019-74-C-0147, *ibid*, August 1975.
- [4] W. B. Hillig, "Impact Response Characteristics of Polymeric Materials," General Electric CRD Report SRD-76-112, prepared under Contract N00019-75-C-0320, *ibid*, September 1976.
- [5] W. B. Hillig, "Dynamic Impact Response Behavior of Polymeric Materials," General Electric CRD Report SRD-77-134, prepared under Contract N00019-76-C-0330, *ibid*, August 1977.
- [6] W. B. Hillig, "Dynamic Impact Response Behavior of Polymeric Materials (II)," General Electric CRD Report SRD-79-056, prepared under Contract N00019-77-C-0441, *ibid*, March 1979.
- [7] A. E. H. Love, "A Treatise on the Mathematical Theory of Elasticity," Dover (1944) New York, p. 428.
- [8] J. D. Achenbach, "Wave Propagation in Elastic Solids," North Holland Publishing Co., 1973, New York p. 344ff.
- [9] H. Kolsky, "Stress Waves in Solids," Oxford University Press (1953), p. 63ff.

11. APPENDIX

11.1 Conversion of Impact Pulse Data into Force-Time and Energy-Time Relationships

The basis for deducing the force indentation response in the impact event from the impact pulse was discussed in previous reports⁽⁵⁾ and is incorporated here for convenience.

Because the impact occurs over a concentrated area, the compressive acoustic pulse radiates initially as a spherical wave. However, as it travels down the bar, the compressive wave becomes increasingly planar. If the initial impact does not occur on the axis of symmetry of the bar, then flexural modes can be excited in the bar. Furthermore, surface and transverse waves can be expected as well. Thus, the signal detected at the strain gage comprises a complex superposition of waves. In spite of this, the data will be treated as if the strain pulse consisted only of the planar compressive component. This means the analysis will be somewhat in error and that calibration to provide the necessary corrections would be desirable.

For purposes of analysis, it is convenient to refer to the position of the struck end of the bar as the origin of the z axis and the time $t = 0$ as the instant of first contact between the ball and the bar. The ball has a mass m and is assumed to be incompressible.

Deceleration of the spherical projectile results from the local opposing material reaction force which in turn is supported elastically in the impact bar. Hence, the instantaneous deceleration force is $A\sigma(t)$ where A is the cross section of the bar, and σ the area-averaged longitudinal stress. Therefore,

$$m\ddot{z} = -A\sigma(t) \quad (\text{Eq. a})$$

$$= -AE\epsilon(t) \quad (\text{Eq. b})$$

This can be integrated directly to give

$$\dot{z} = - (AE/m) \int_0^t \epsilon dt + v_0 \quad (\text{Eq. c})$$

and

$$z = v_0 t - \frac{AE}{m} \int_0^t \int_0^{t'} \epsilon dt' dt \quad (\text{Eq. d})$$

where E is the Young's modulus of the bar, epsilon is strain, and v_0 is the initial velocity of the projectile. However, the collision causes the impact bar to be elastically compressed. Therefore, the end of the bar is displaced in the direction of the impacting projectile a distance w

$$w = \int_0^z \epsilon dz \quad (\text{Eq. e})$$

$$= c \int_0^t \epsilon dt \quad (\text{Eq. e'})$$

where c is the velocity of sound. Thus, penetration is given by

$$x = z - w \quad (\text{Eq. f})$$

and the velocity of the projectile relative to the end of the bar is given by

$$\dot{x} = \dot{z} - c\epsilon \quad (\text{Eq. g})$$

Assuming the projectile to rebound with a velocity v_f , its change in momentum must equal the momentum imparted to the bar. This is the total time integral of the force (neglecting reflections), or

$$m(v_o - v_f) = AE \int_0^{\infty} \epsilon dt \quad (\text{Eq. h})$$

in which v_o and v_f are the (algebraic) velocities and can have positive or negative values depending on whether the motion is in the direction of the initial impact or its reverse, respectively.

In general the actual measurement of the pulse consists of a strain gage voltage reading as a function of time. This strain is presumably proportional to the strain averaged over the cross section. However, for reasons already discussed, a strain at the gage itself may depart from the average strain. Assuming the average planar strain ϵ is simply proportional to the observed strain ϵ_g at the gage, i.e., $\epsilon = \beta \epsilon_g$, we can write for the correction factor β using Eq. (h)

$$\beta = m(v_o - v_f) / (AE \int_0^{\infty} \epsilon_g dt) \quad (\text{Eq. i})$$

The factor β ensures that conservation of momentum is preserved. Wherever epsilon appears in the preceding equations, this should be replaced by $\beta \epsilon_g$. Thus, in principle, the striker velocity \dot{z} , penetration velocity \dot{x} , penetration depth, resisting force, and other related quantities can be computed from the impact pulse.

Energy is distributed within the specimen and the bar in several ways. Some of the energy is localized near the site of the impact, e.g., that expended in the non-recoverable (anelastic, plastic, viscous) deformation process. There is also a local elastic energy stored in the impact region that subsequently is transferred back to the striker when it rebounds. Finally, there is both a distributed kinetic and potential energy associated with the pulse as it moves along the impact bar. This later energy can be computed as it develops with time. The elastic potential energy is given by

$$\begin{aligned} U_1 &= \int (\text{strain energy/unit volume}) d(\text{volume}) \\ &= \frac{1}{2} A E c \int_0^t \epsilon^2 dt \end{aligned} \quad (\text{Eq. j})$$

From the principle of equipartition of energy, this also equals the kinetic energy of the pulse so that the aggregate distributed energy associated with the pulse is

$$U = A E c \int_0^t \epsilon^2 dt \quad (\text{Eq. j'})$$

This energy is trapped in the bar, and excites the bar vibrationally, ultimately ending up a heat.

The kinetic energy of the striker can be determined as a function of time. However, we have found no simple way as yet of computing the amount of recoverable energy as a function of time during the course of the collision. The final irreversible work performed on the specimen, of course, is simply the initial kinetic energy of the striker, less its recoil kinetic energy and the pulse energy U .

Determination of the various penetration, velocity, energy, and correction quantities requires evaluation of the integrals $\int \epsilon dt$, $\int \int \epsilon dt dt$, $\int \epsilon^2 dt$. Once the strain is available in digitized form, the evaluations are straightforward using standard computer techniques. The uncertainties arise primarily from the impact pulse itself. In

principle, the pulse should rise from a base line, representing the zero strain condition and should then return to the same base when the striker, upon rebound, breaks contact with the target. However, this idealized situation is usually not observed. Procedures for the non-ideal real pulses were discussed in 5.4.

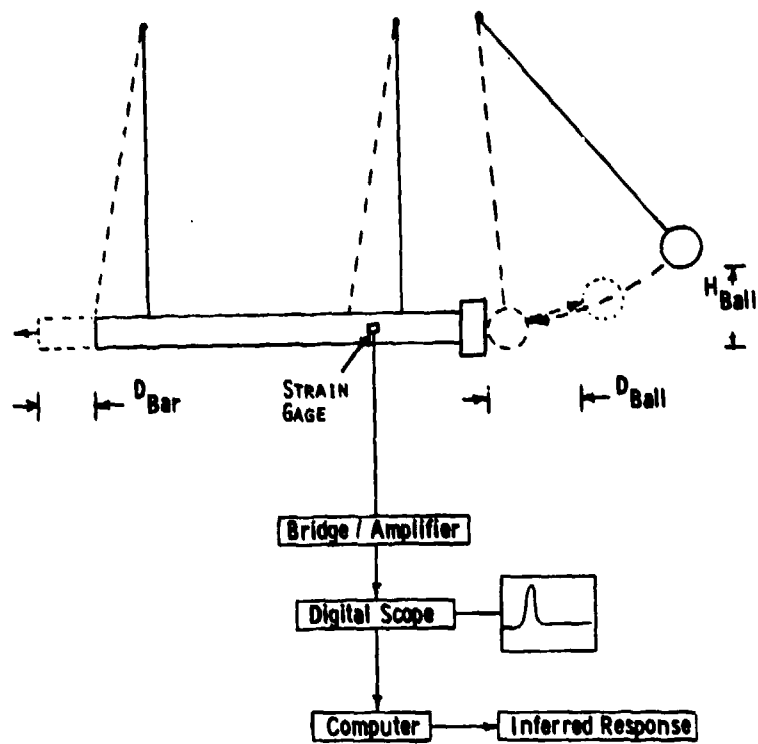


Fig. 4A. Schematic representation of impact bar.

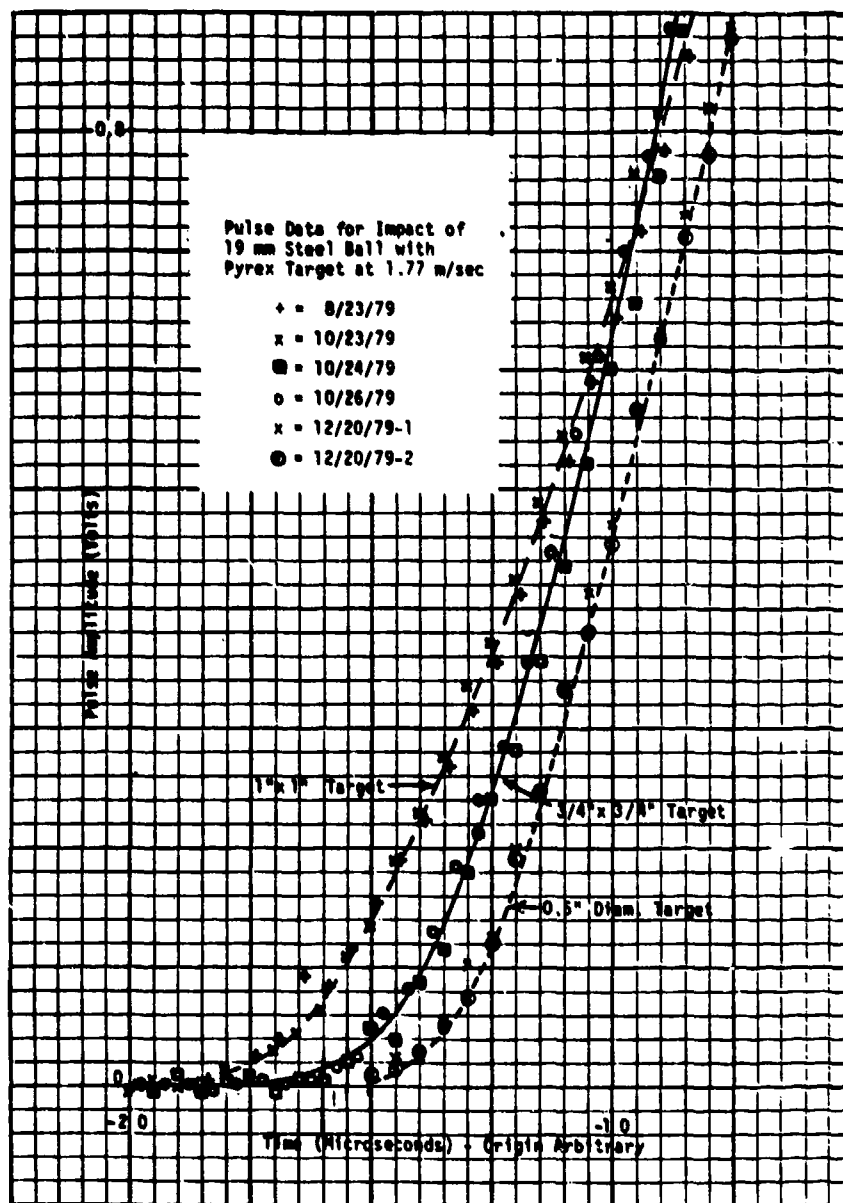


Fig. 4.1A. Effect of size of Pyrex target used with 0.5" SiO₂ bar.

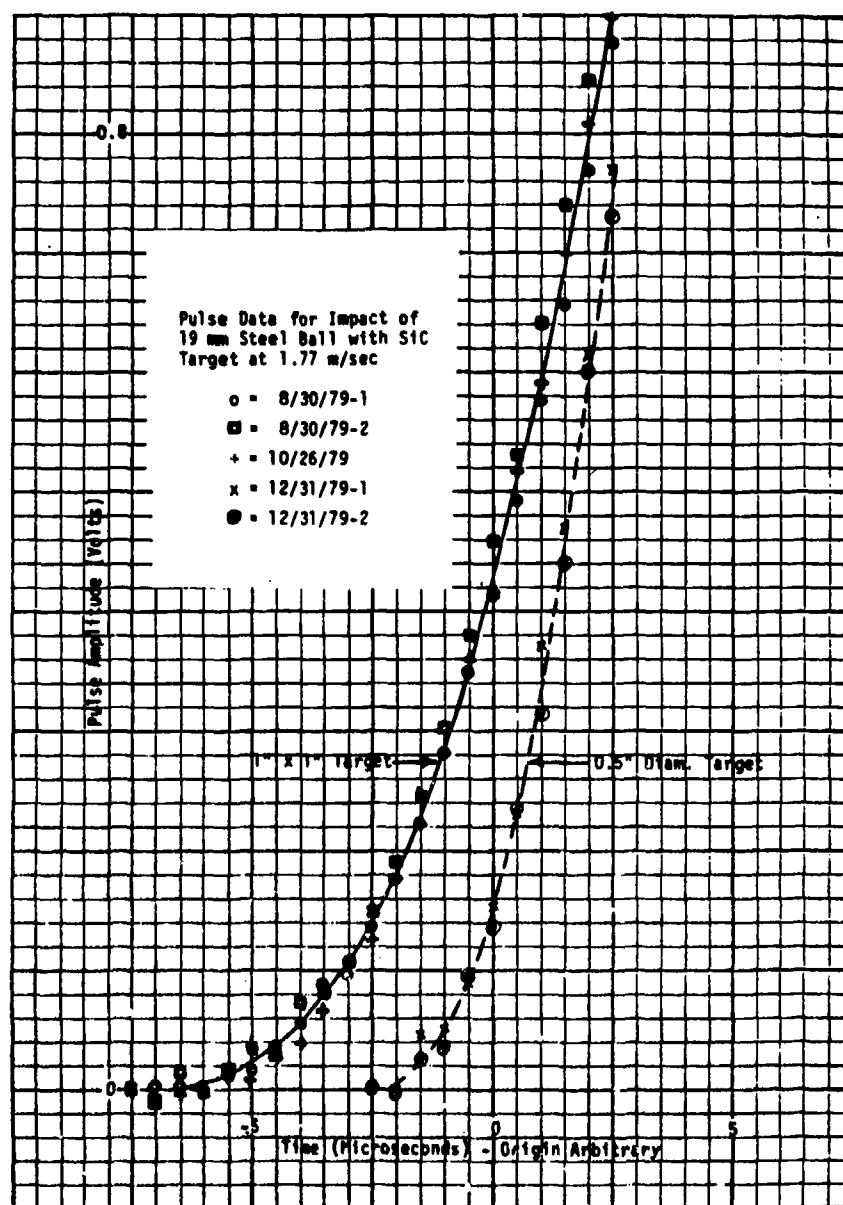


Fig. 4.1B. Effect of size of SiC target used with 0.5" SiO₂ bar.

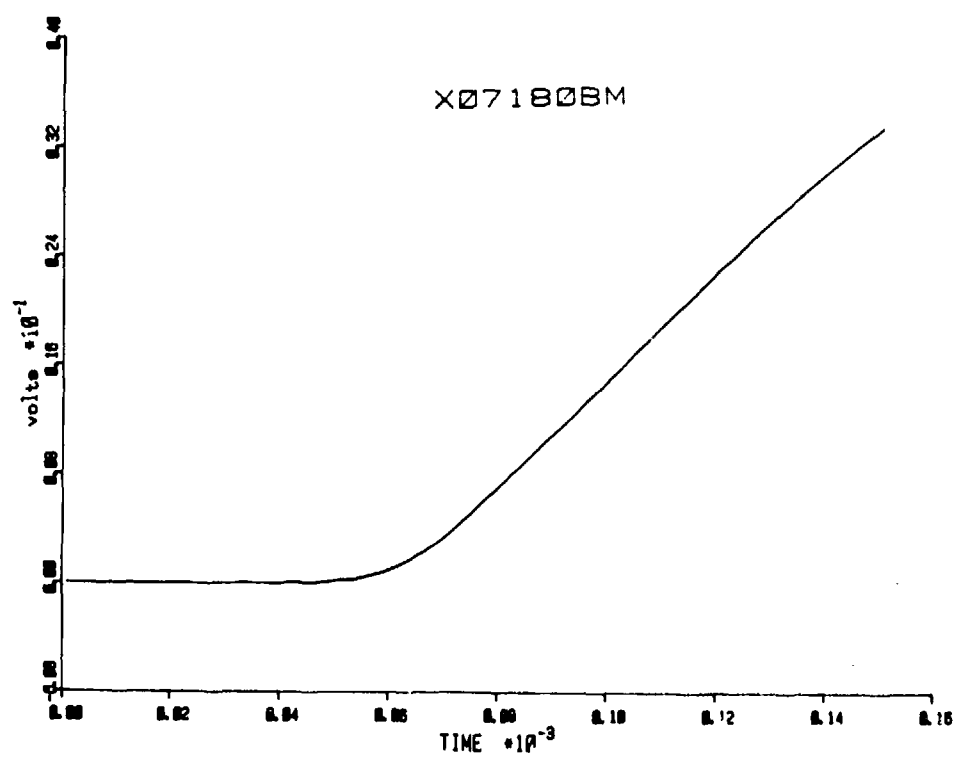
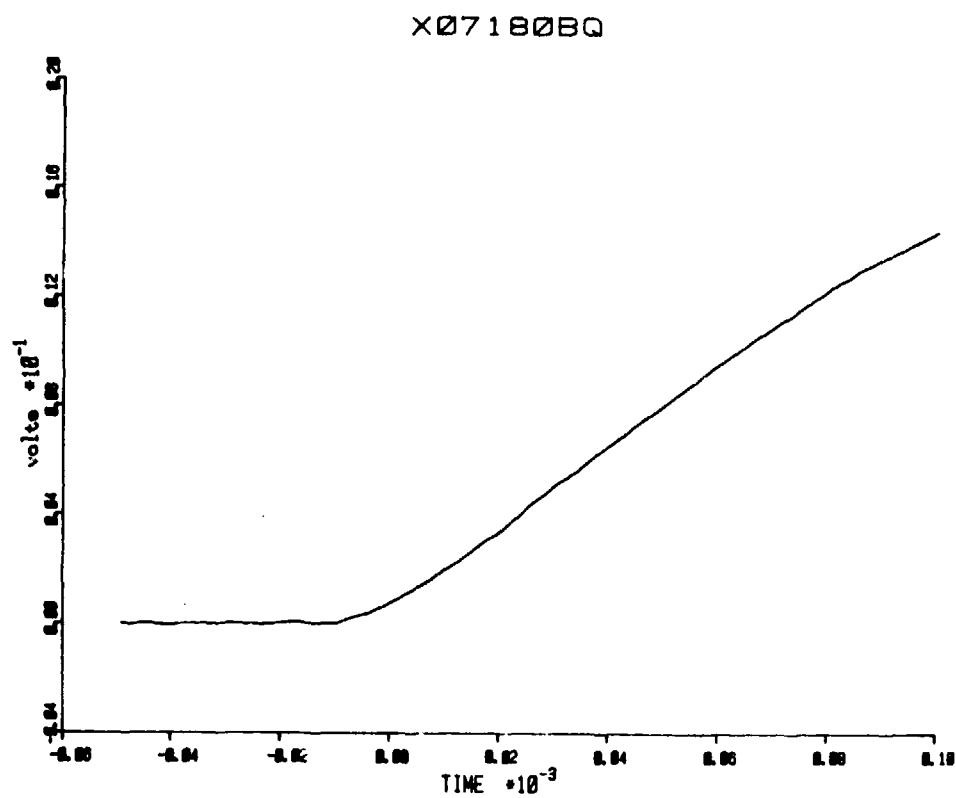


Fig. 4.2A. End-on impact of SiO_2 bar against PMMA bar. X07180BQ is pulse in SiO_2 bar. X07180BM is pulse in PMMA bar.

P08270P2

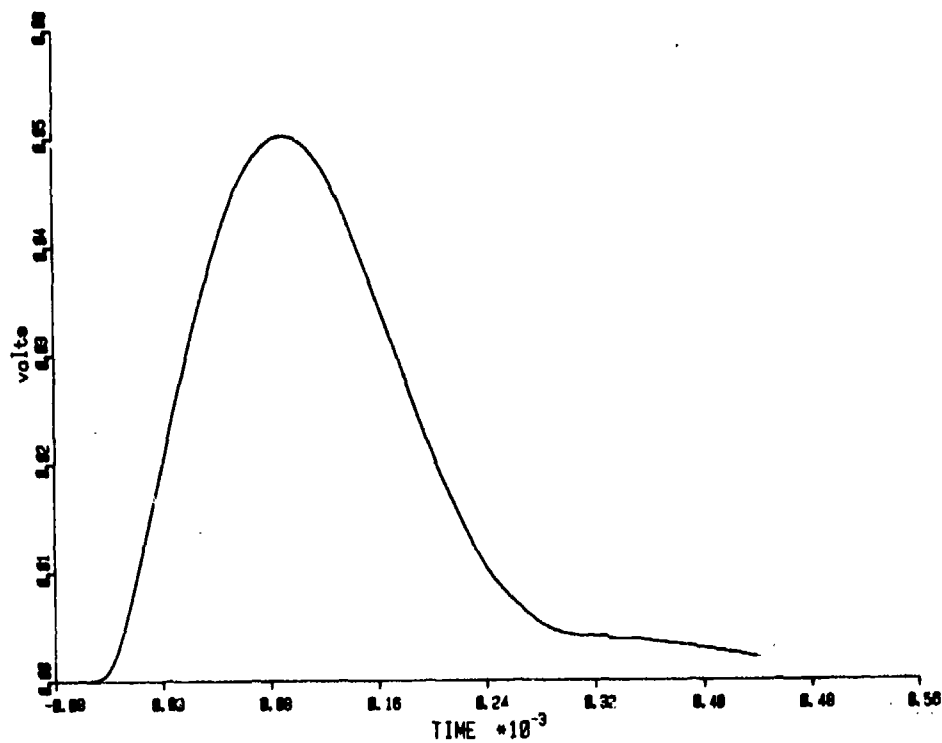


Fig. 4.3A. Impact of 4.5 mm 42 g projectile with PMMA target on PMMA bar at 2.1 m/s.

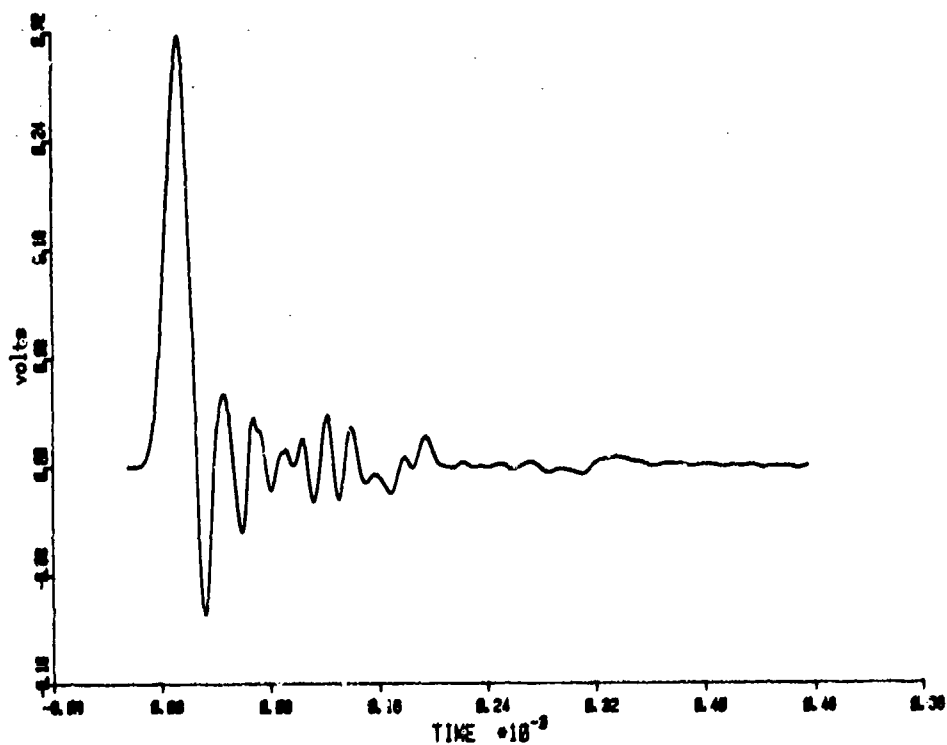


Fig. 4.3B. Pulse due to impact of 4.5 mm steel ball with PMMA target at 126.2 m/s as detected at 15 cm gage, Run 1.

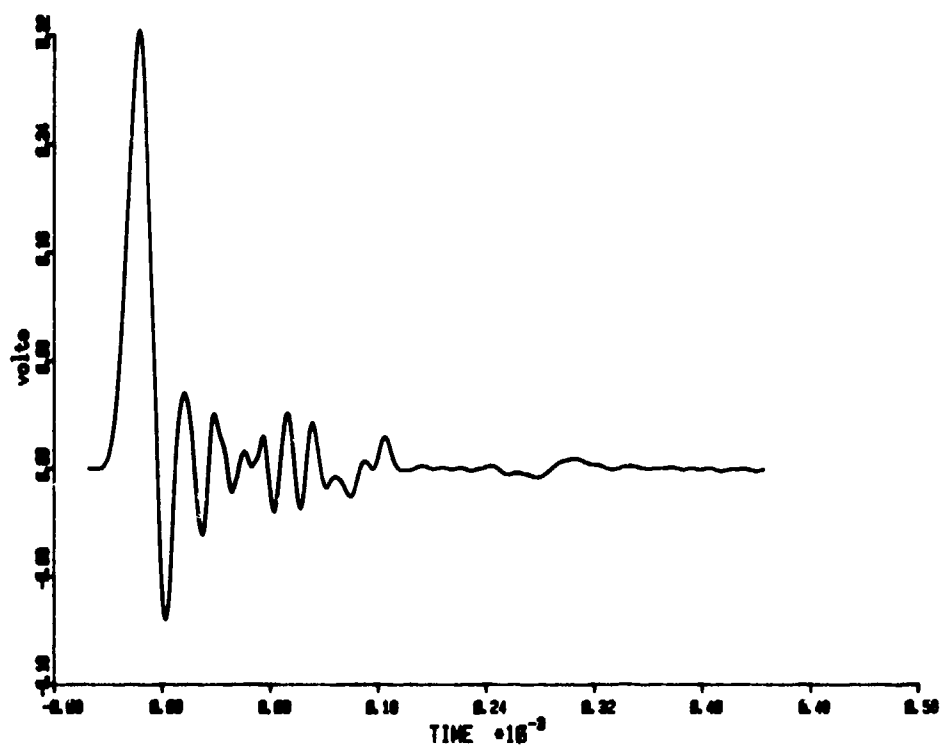


Fig. 4.3C. Pulse due to impact of 4.5 mm steel ball with PMMA target at 128.1 m/s as detected at 15 cm gage, Run 2.

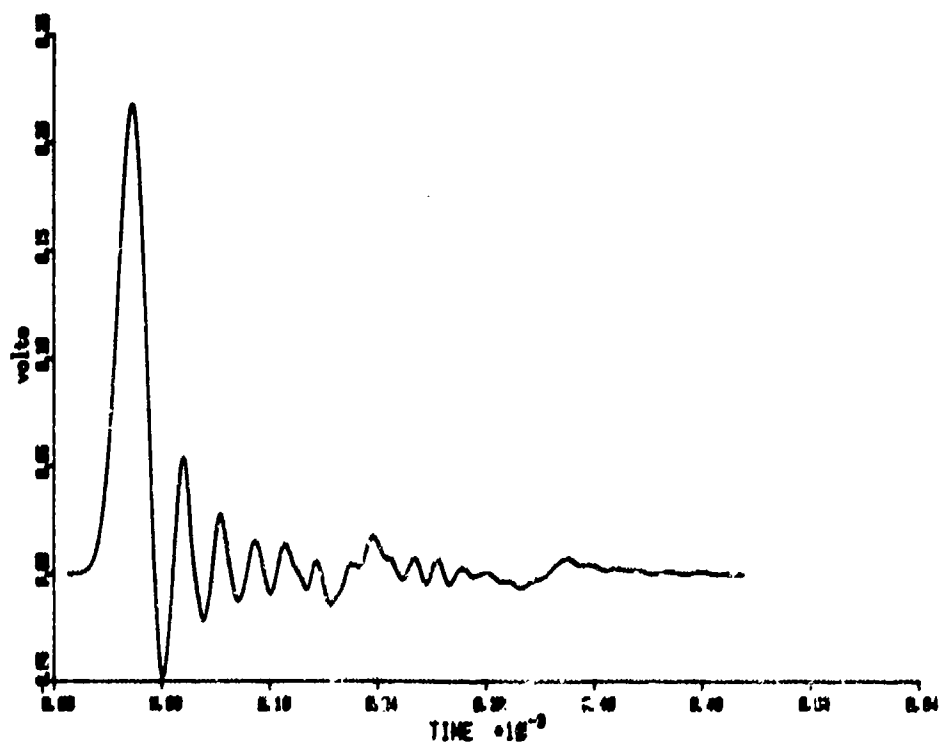


Fig. 4.3D. Pulse due to impact of 4.5 mm steel ball with PMMA target at 126.2 m/s as detected at 36 cm gage, Run 1.

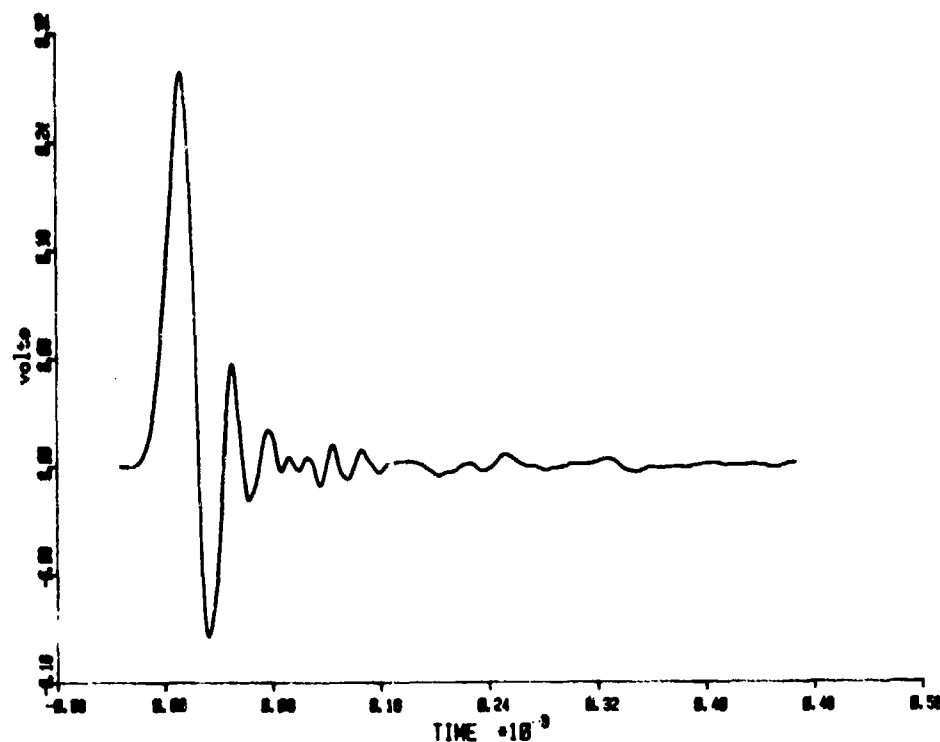


Fig. 4.3E. Pulse due to impact of 4.5 mm steel ball with PC target at 124.5 m/s as detected at 15 cm gage, Run 1.

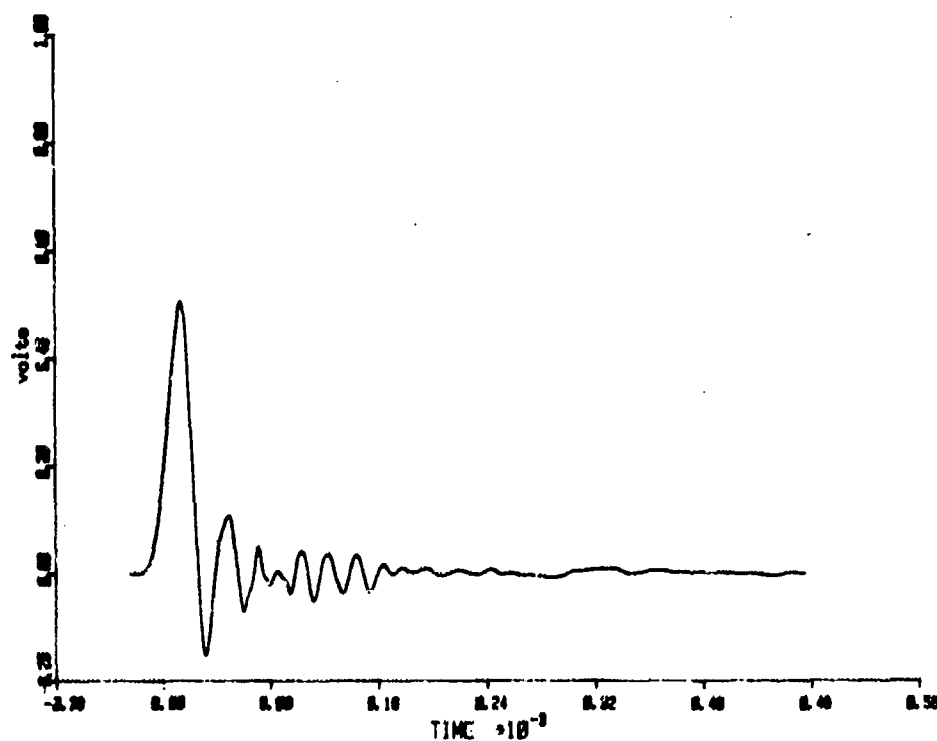


Fig. 4.3F. Pulse due to impact of 4.5 mm steel ball with PMMA target at 219.9 m/s as detected at 15 cm gage, Run 1.

AVE. Q PULSE/X07180

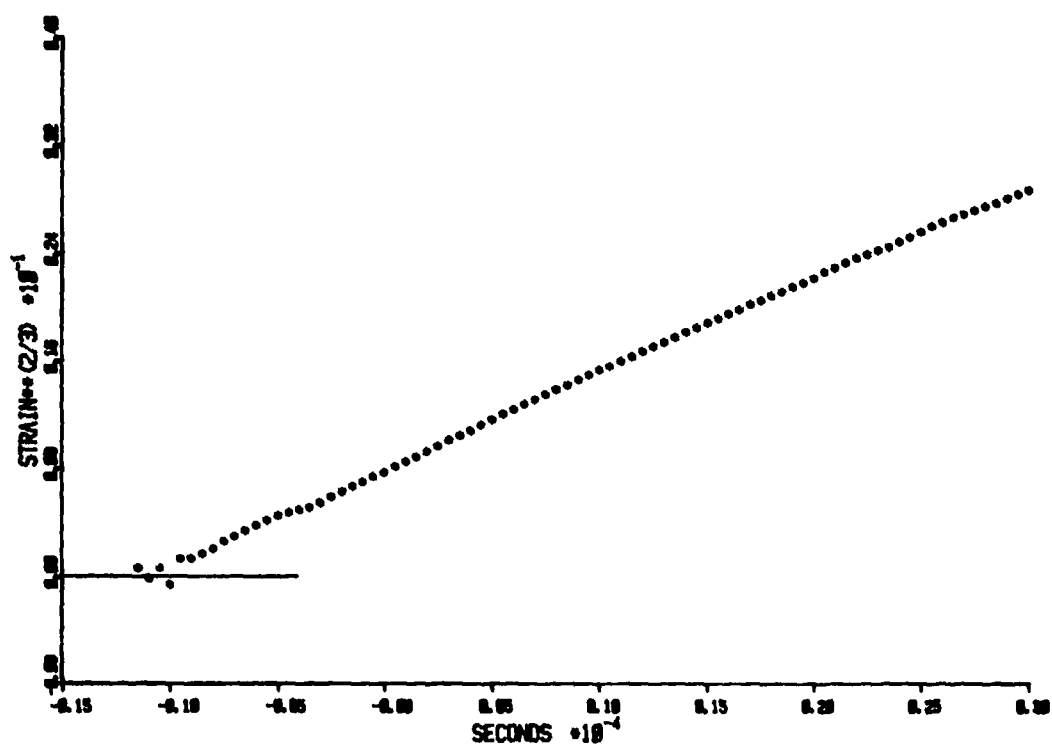


Fig. 5.1A. Plot showing linear behavior of $2/3$ power of strain as a function of time averaged data obtained in SiO_2 bar from replicate runs of end-on impacts between SiO_2 and PMMA bars.

X07180BM

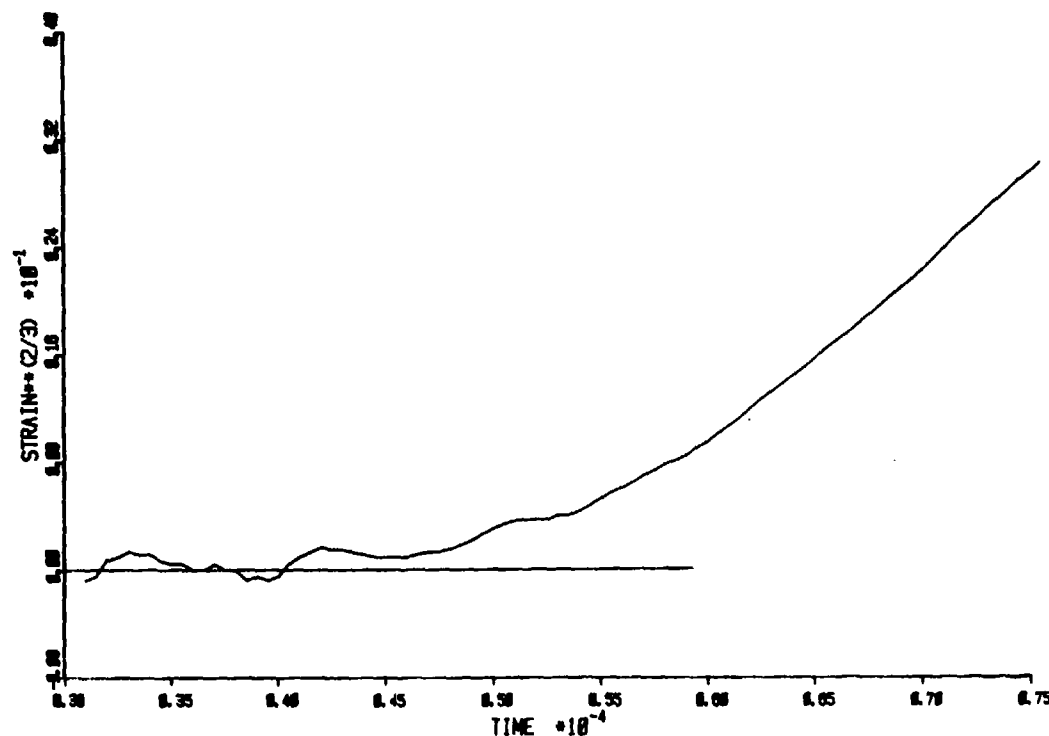


Fig. 5.1B Plot showing lack of linear behavior of 2/3 power of strain as a function of time of averaged data obtained in PMMA bar from replicate runs of end-on impacts between SiO_2 and PMMA bars.

AVE. M PULSE/X07180

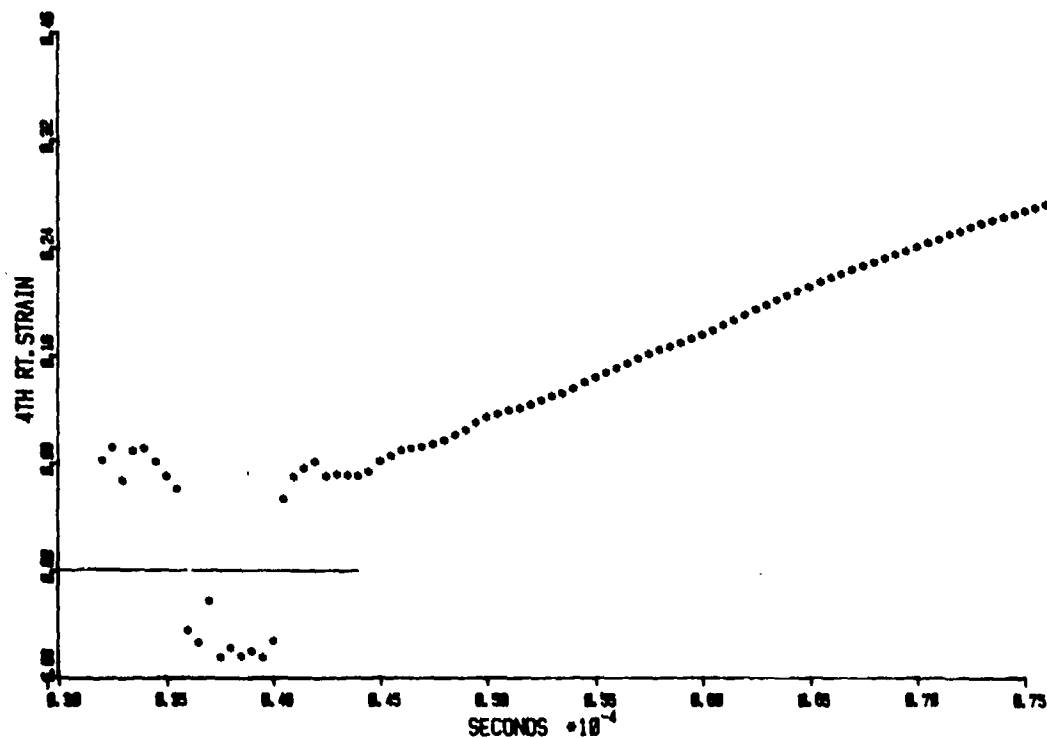


Fig. 5.1C. Plot showing linear behavior of 1/4 power of strain as a function of time of averaged data obtained in PMMA bar from replicate runs of end-on impacts between SiO_2 and PMMA bars.

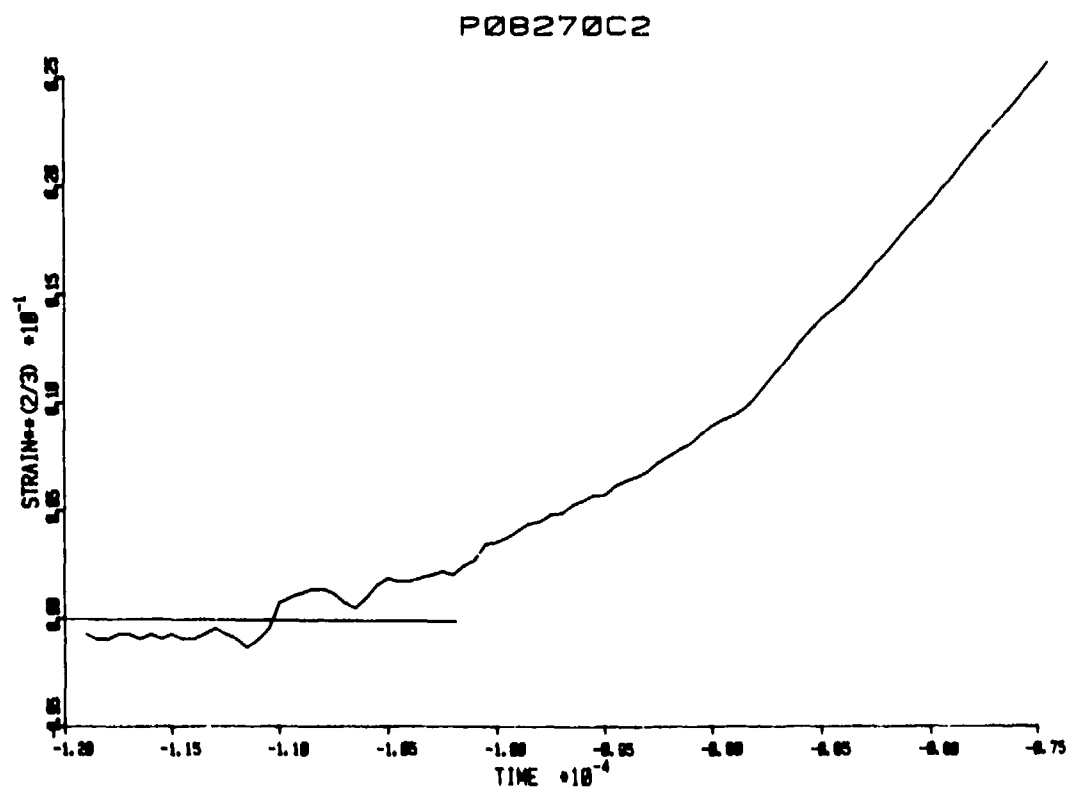
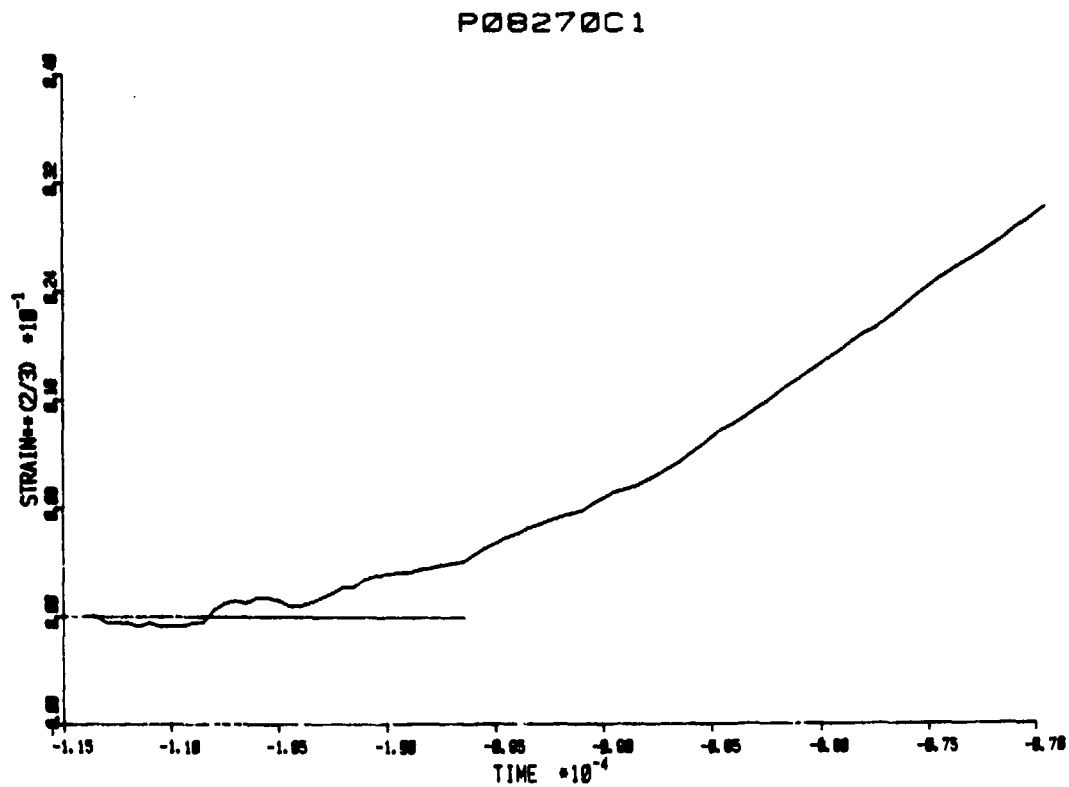
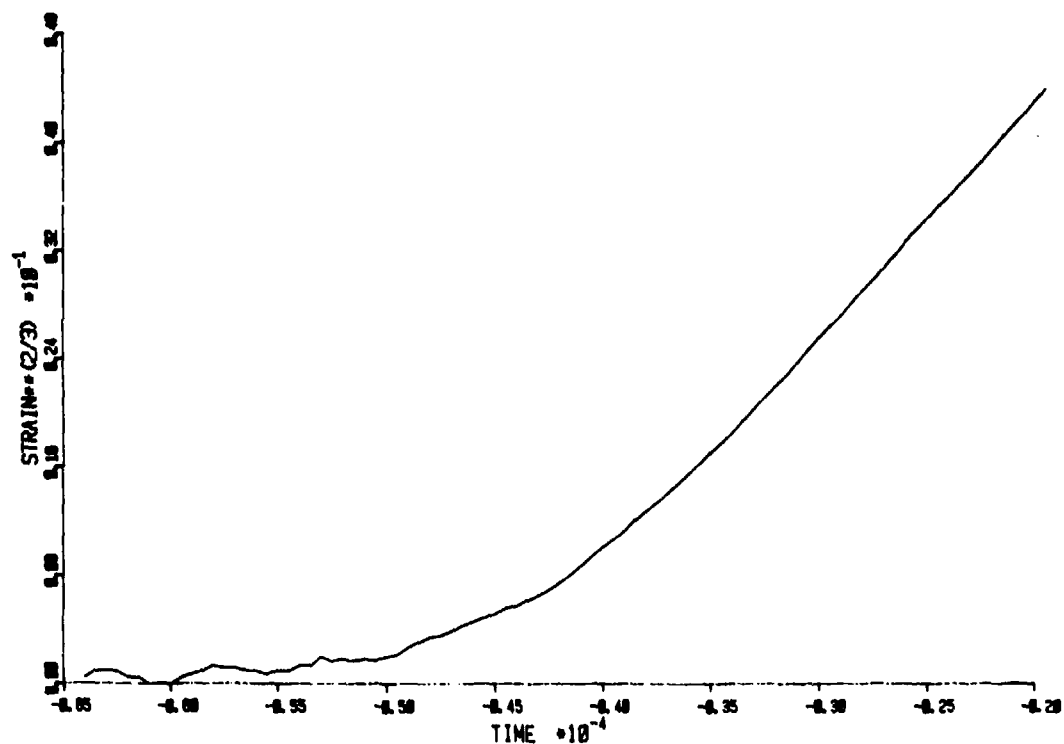


Fig. 5.1D. Plot showing lack of linear behavior of $2/3$ power of strain vs time in a signal due to impact of a 4.5 mm diameter, 42 g striker against a PC specimen on a PMMA bar at 2.1 m/s P08270C1 and P08270C2 are replicate runs.

P08270P2



P08270P1

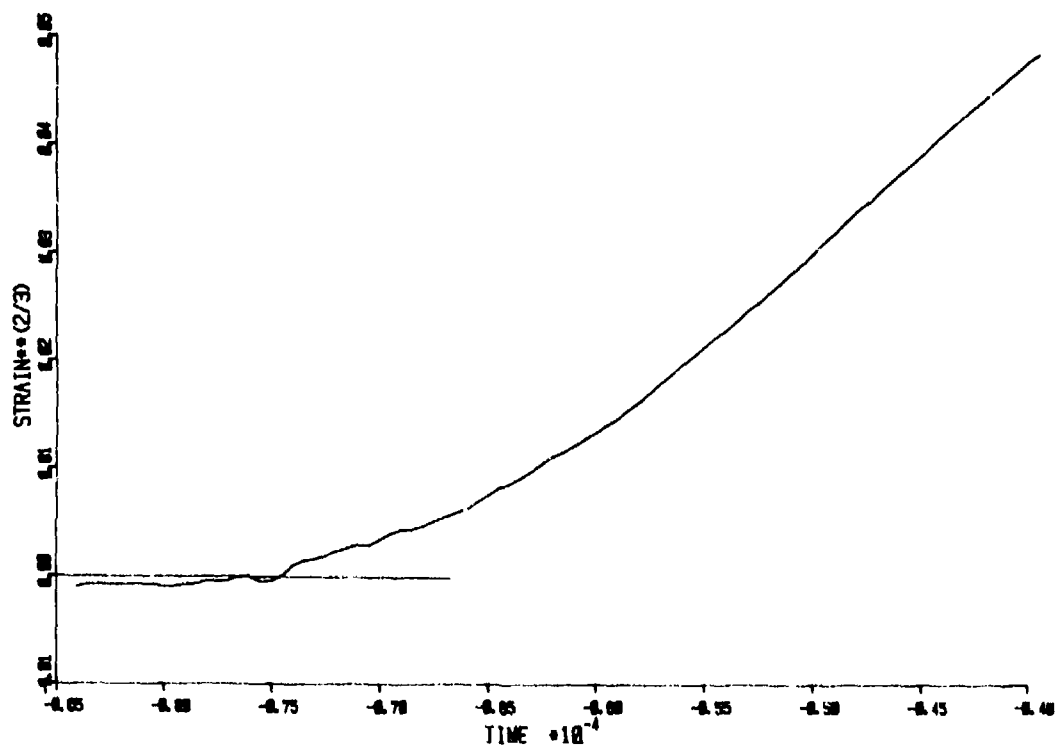


Fig. 5.1E. Plot showing lack of linear behavior of 2/3 power of strain vs time in a signal due to impact of a 4.5 mm diameter, 42 g striker against a PMMA specimen on a PMMA bar of 2.1 m/s. P08270P1 and P08270P2 are replicate runs.

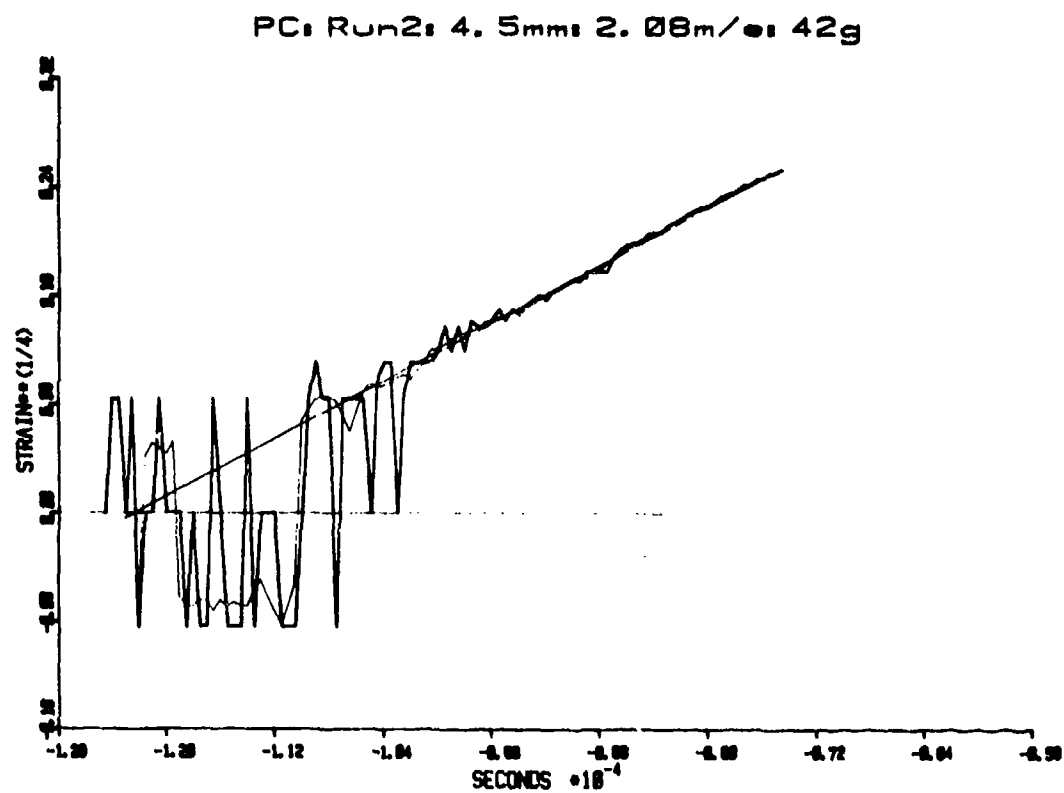
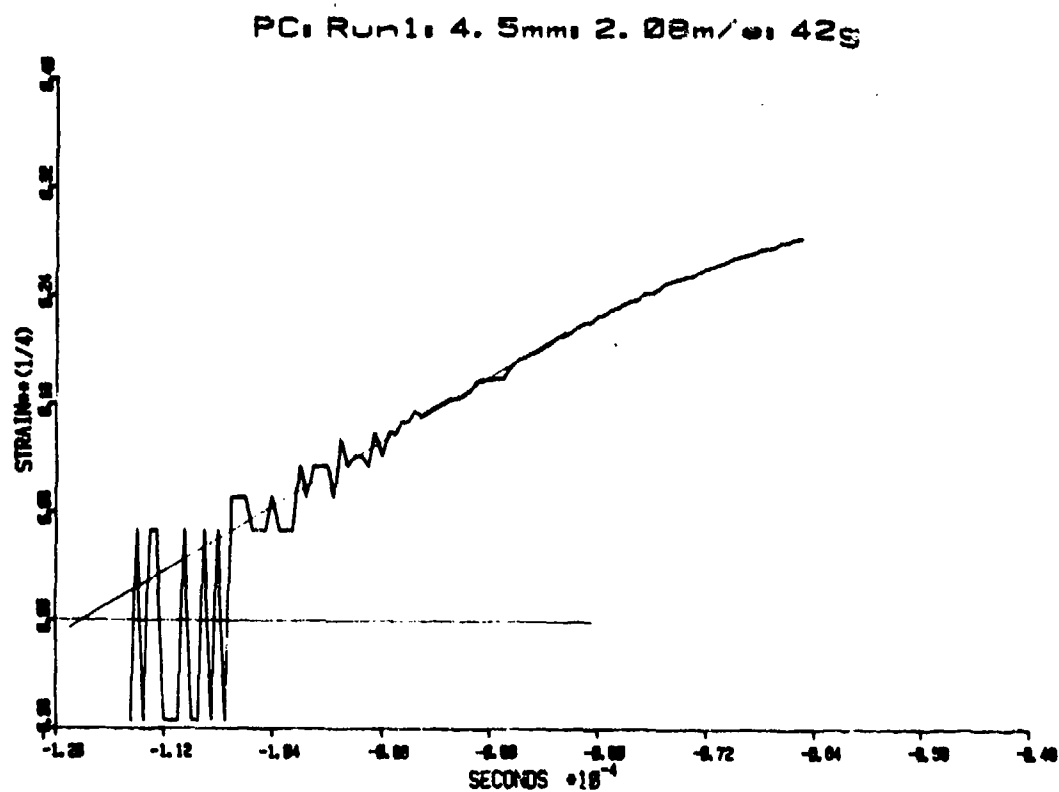
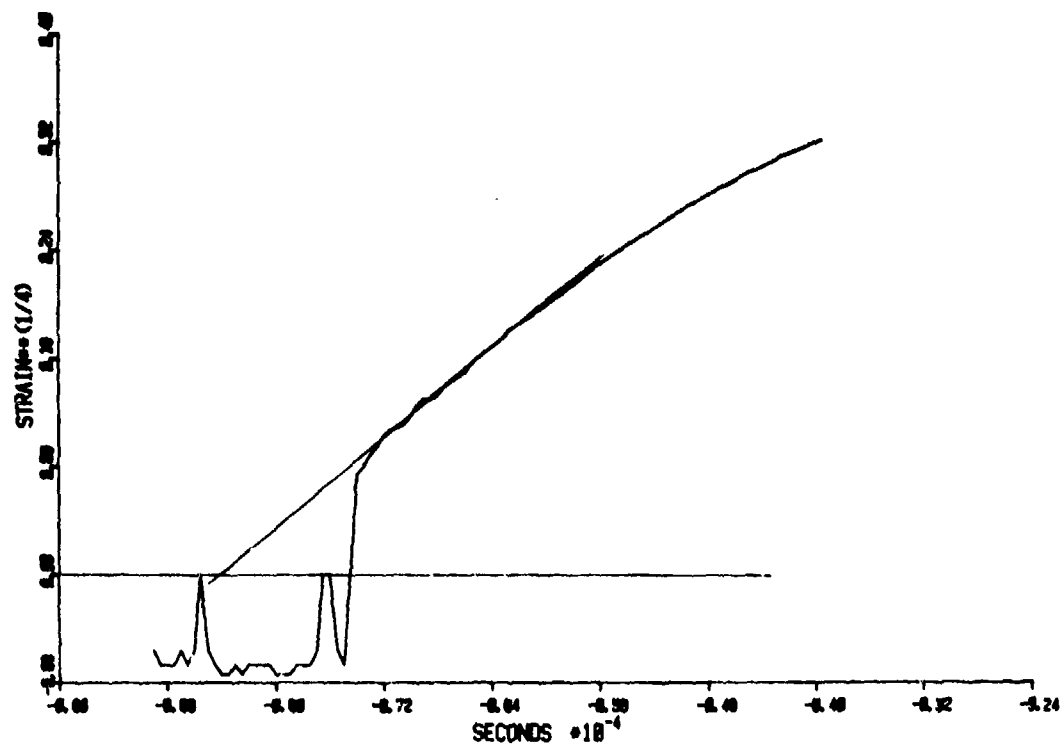


Fig. 5.1F. Plot showing linear behavior of 1/4 power of strain vs time in a signal due to impact of a 4.5 mm diameter, 42 g striker against a PC specimen on a PMMA bar at 2.1 m/s.

PMMA: Run1: 4.5mm: 2.08m/s



PMMA: Run1: 4.5mm*2.08m/s

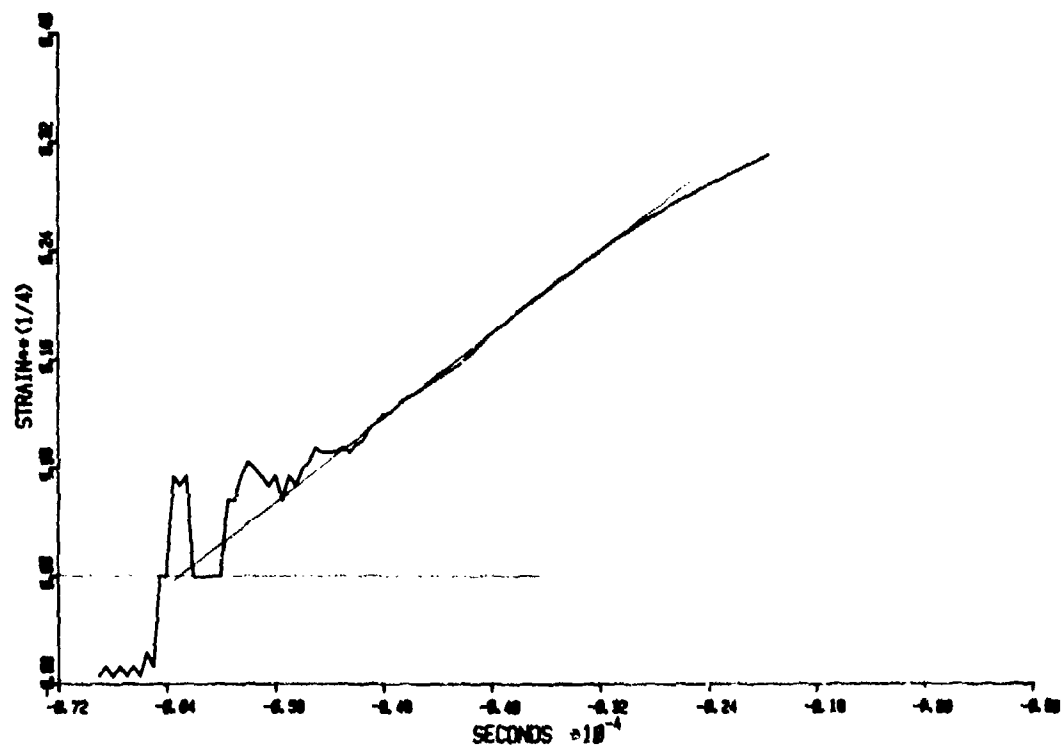


Fig. 5.1G. Plot showing linear behavior of 1/4 power of strain vs time in a signal due to impact of a 4.5 mm diameter, 42 g striker against a PMMA specimen on a PMMA bar at 2.1 m/s.

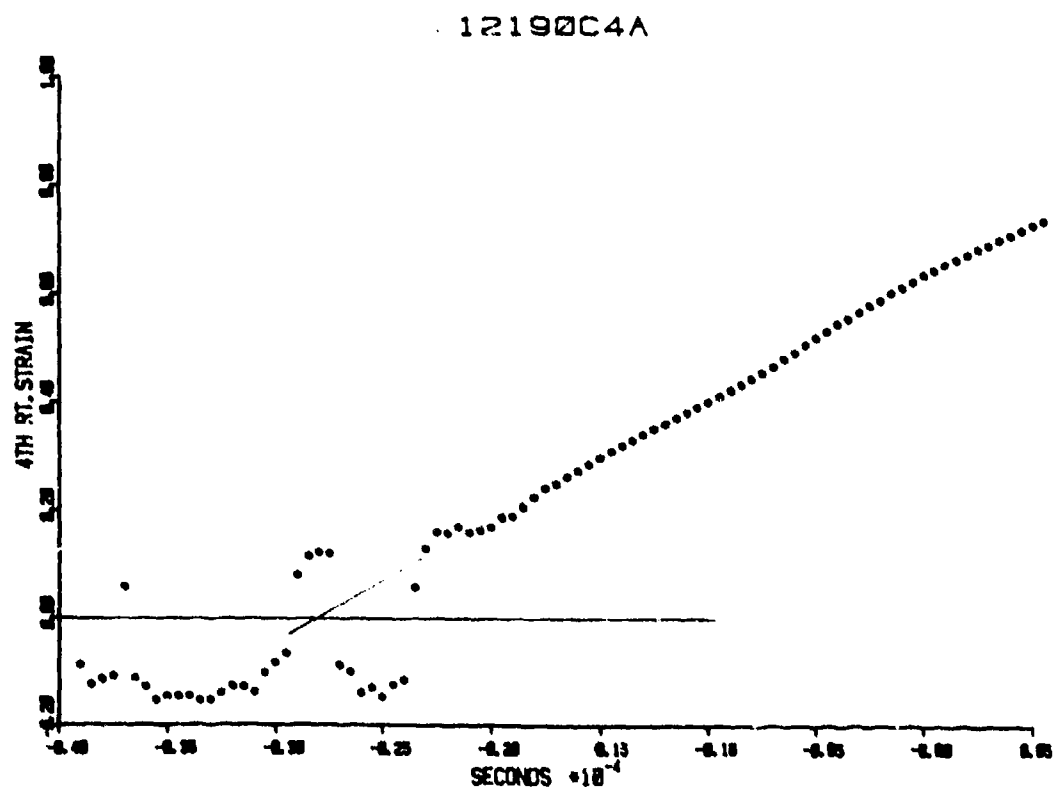
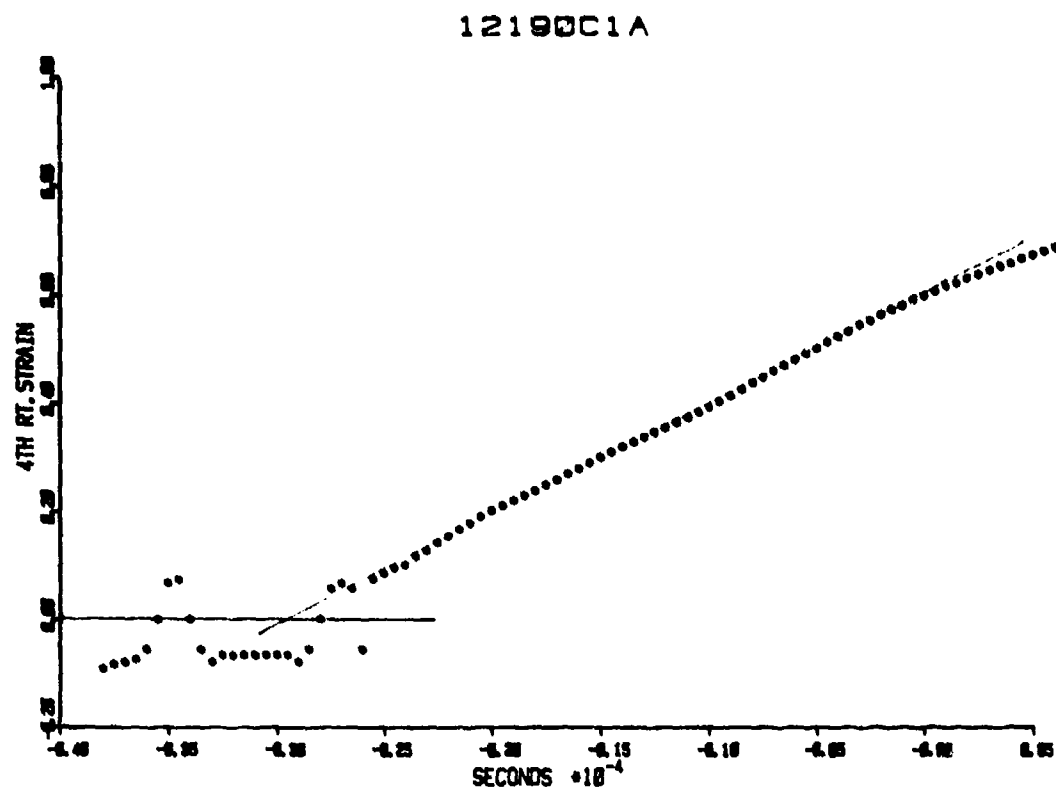


Fig. 5.1H. Plot showing linear behavior of $1/4$ power of strain vs time due to impact of a 4.5 mm, .37 g steel ball against a PC specimen on a PMMA bar as detected at 15 cm gage. Impact velocity in 12190C1A was 124.5 m/s. Impact velocity in 12190C4A was 219.9 m/s.

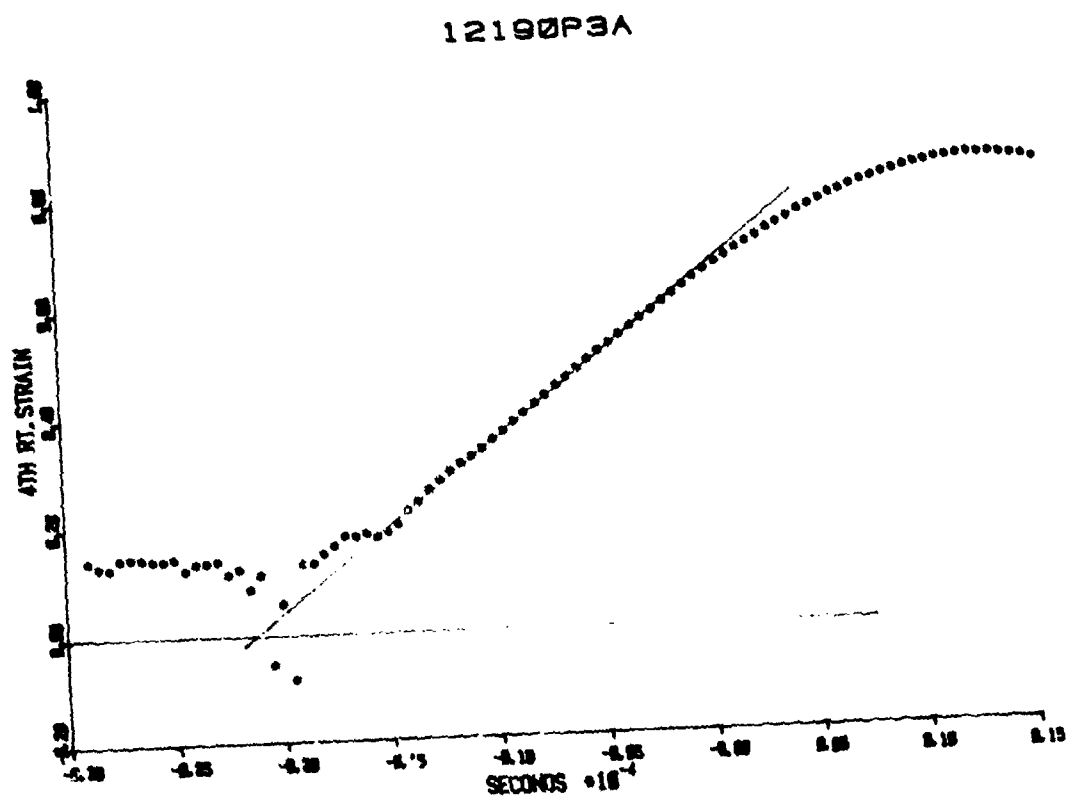
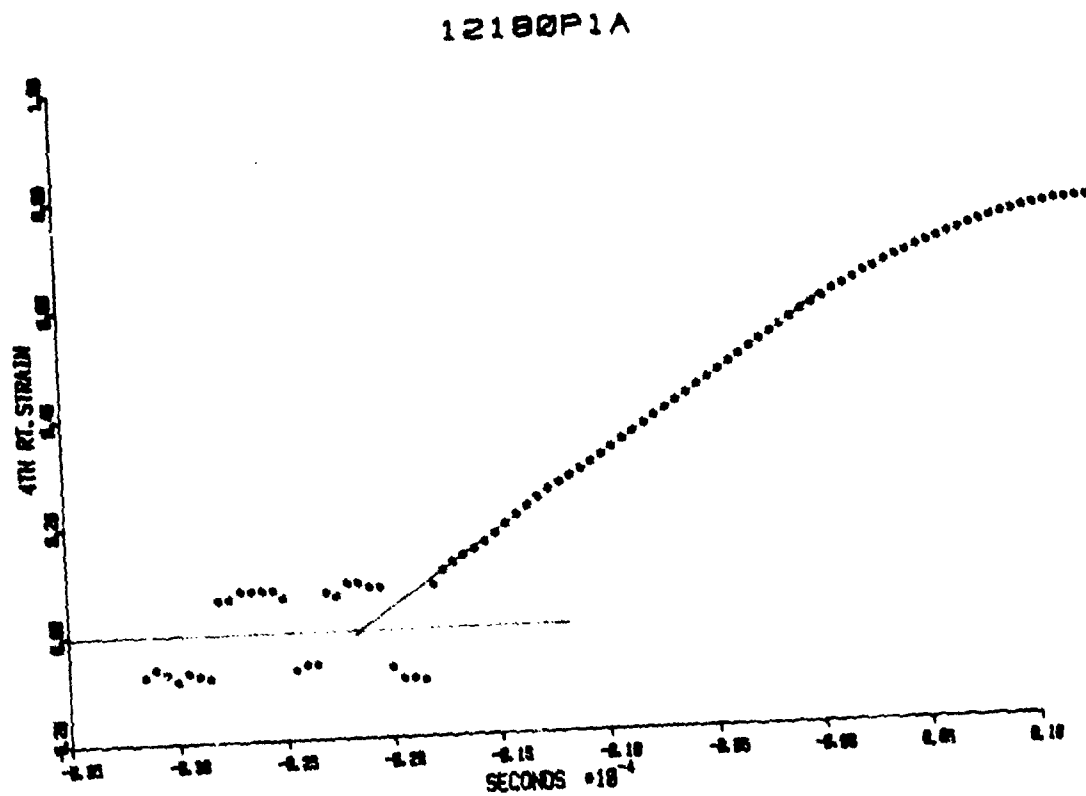


Fig. 5.11. Plot showing linear behavior of 1/4 power of strain vs time due to impact of a 4.5 mm, .37 g steel ball against a PMMA specimen on a PMMA bar as detected at 15 cm gage. Impact velocity in 12180P1A was 126.2 m/s. Impact velocity in 12190P3A was 218.7 m/s.

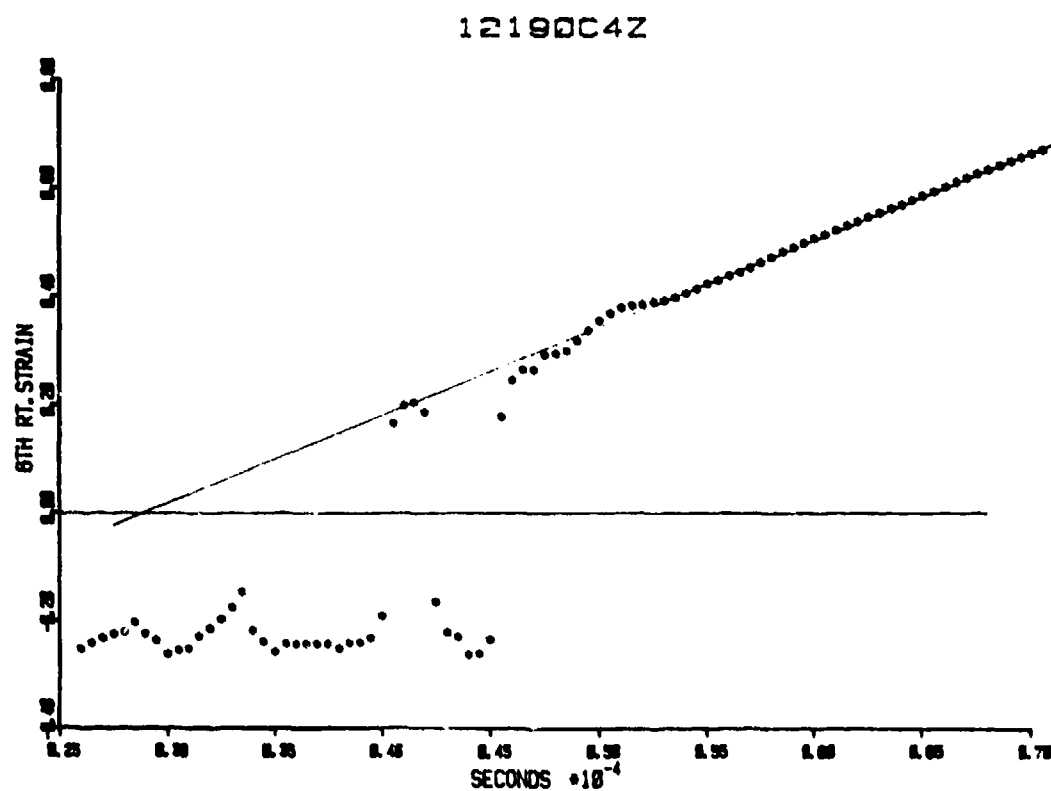
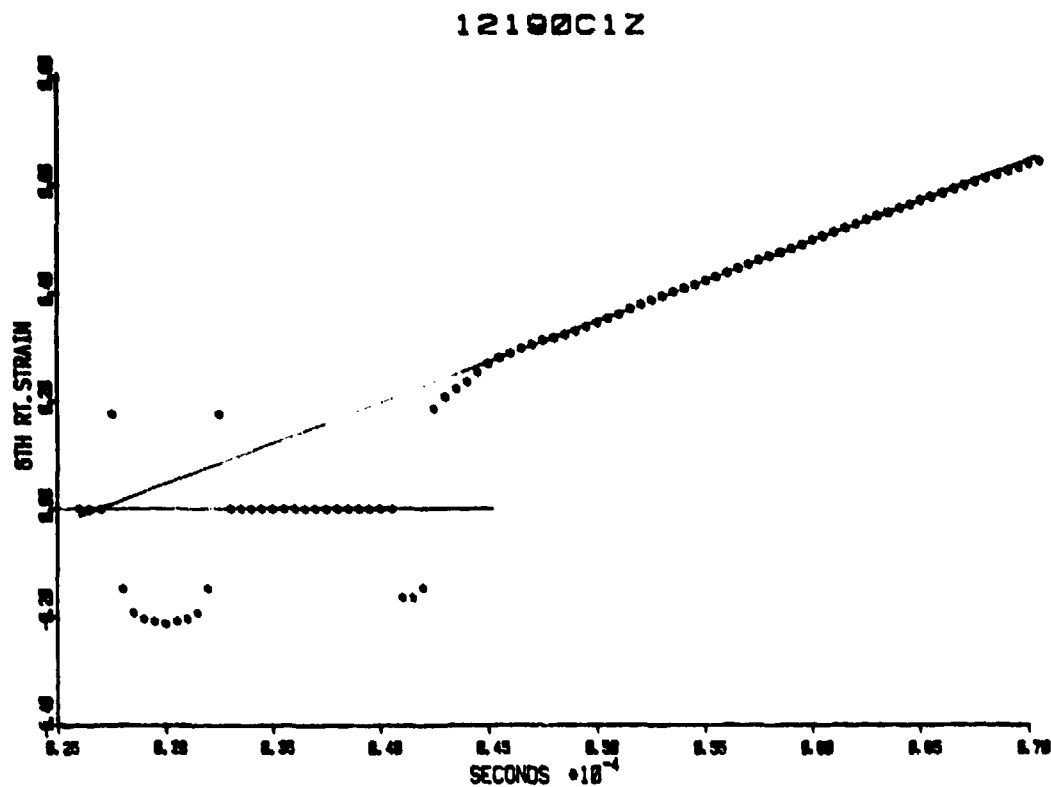


Fig. 5.1J. Plot showing linear behavior of 1/6 power of strain vs time due to impact of a 4.5 mm, .37 g steel ball against a PC specimen on PMMA bar, as detected at 30 cm gage. Impact velocity in 12190C1Z was 124.5 m/s. Impact velocity in 12190C4Z was 219.9 m/s.

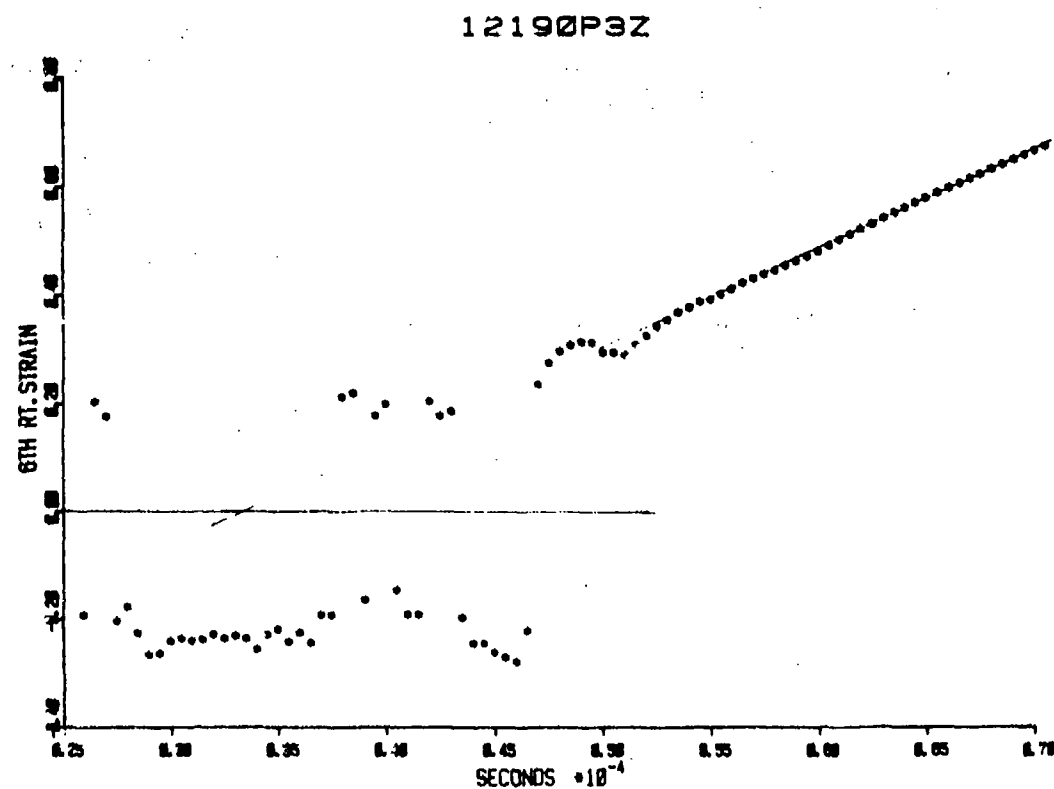
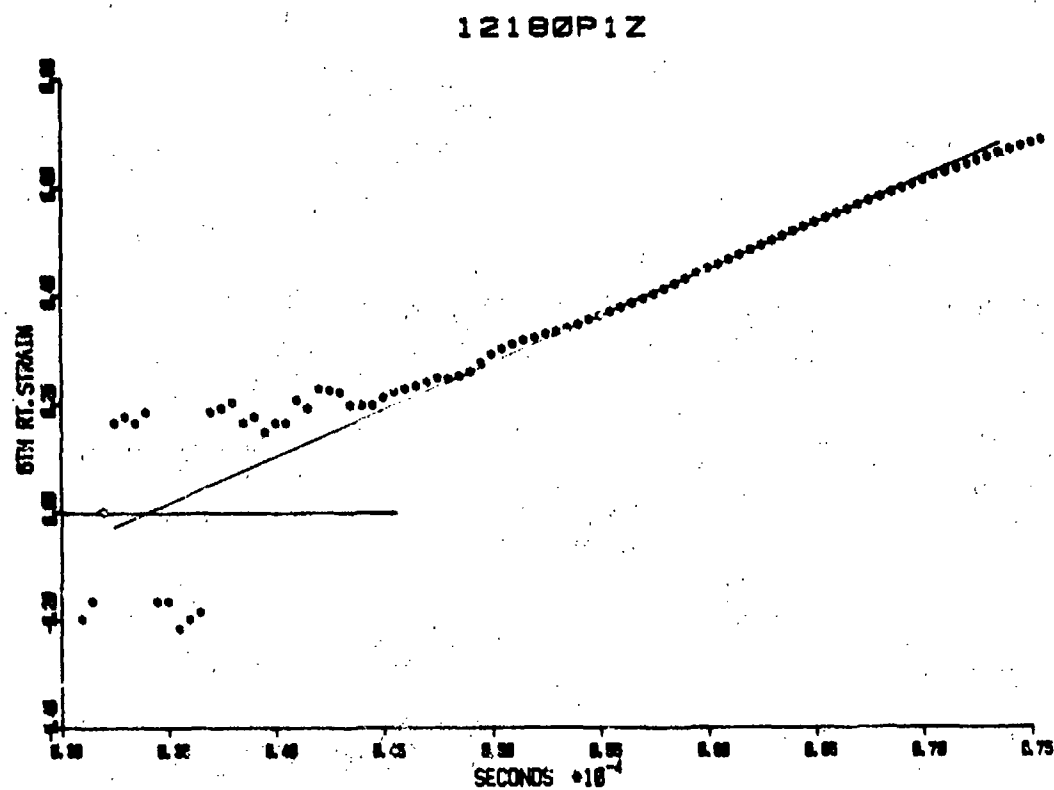
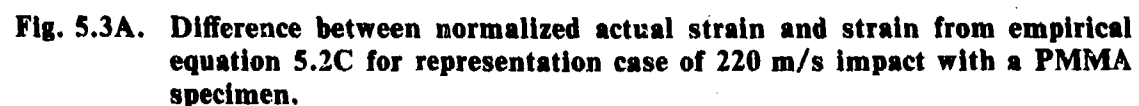
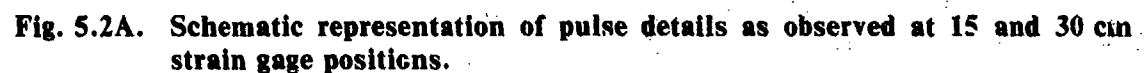


Fig. 5.1K. Plot showing linear behavior of 1/6 power of strain vs time due to impact of a 4.5 mm .37 g steel ball against a PMMA specimen on a PMMA bar, as detected at 30 cm gage. Impact velocity in 12180P1Z was 126.2 m/s. Impact velocity in 12190C4A was 218.7 m/s.



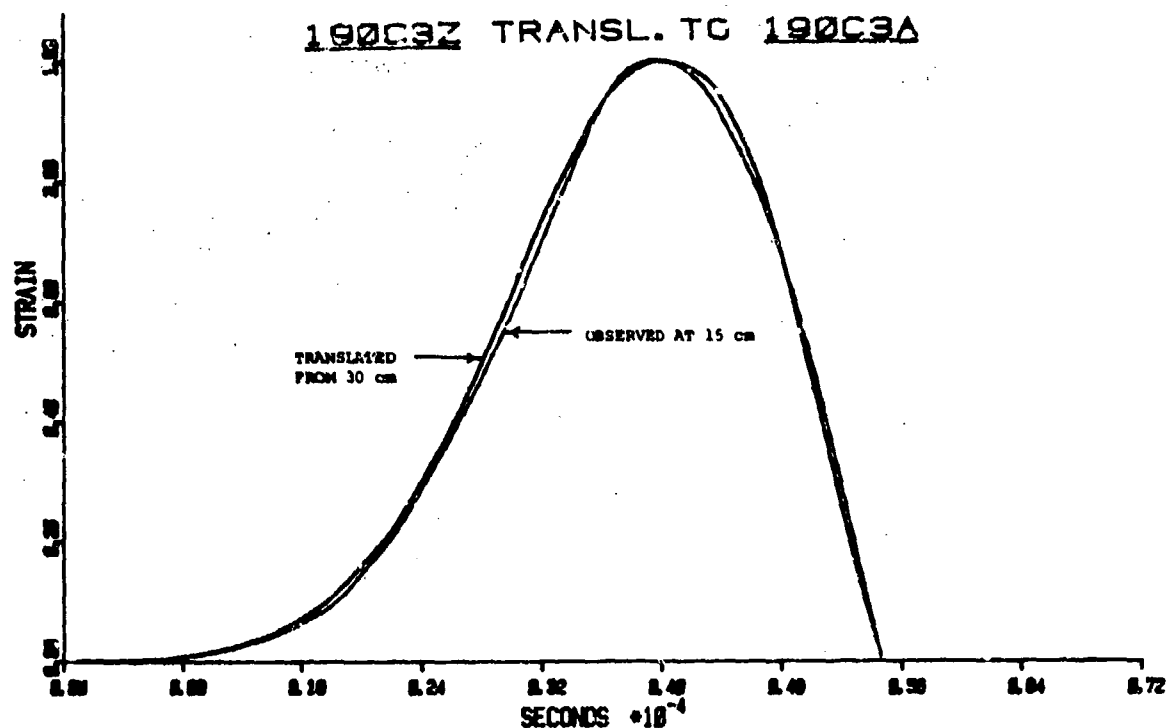


Fig. 5.5A. Computed translation of pulse from 30 cm to 15 cm gage position, for case of 221.5 m/s impact with PC specimen pulse after translation is shown compared pulse observed at 15 cm gage position.

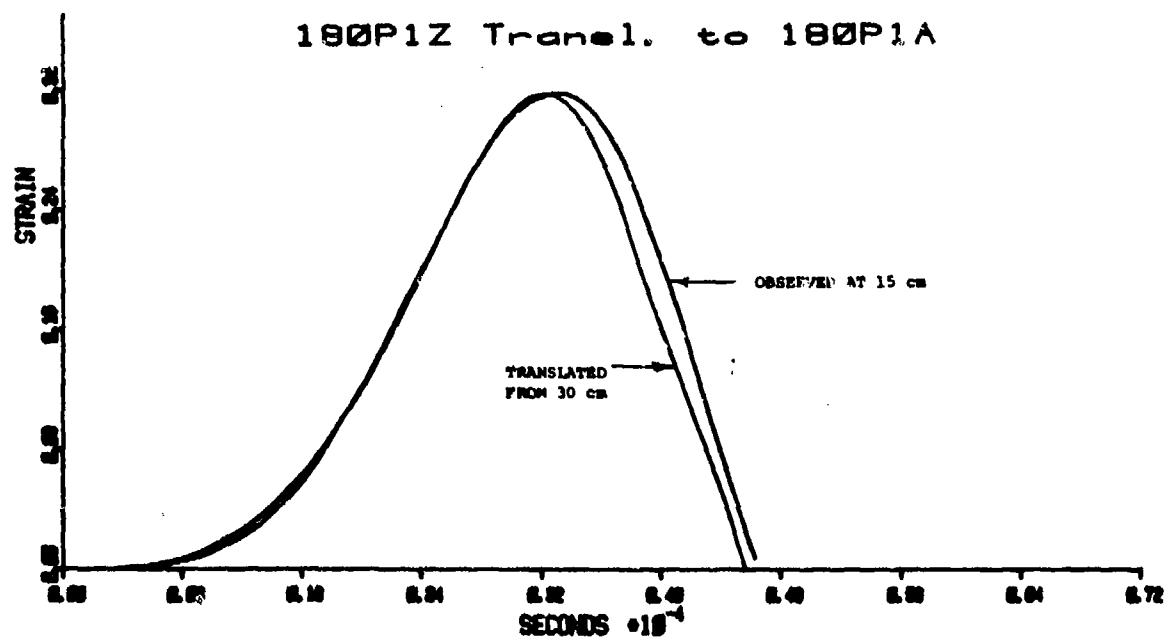


Fig. 5.5B. Computed translation of pulse from 30 cm to 15 cm gage position, for case of 126.2 m/s impact with PMMA specimen. Pulse after translation is shown compared pulse observed at 15 cm gage position.

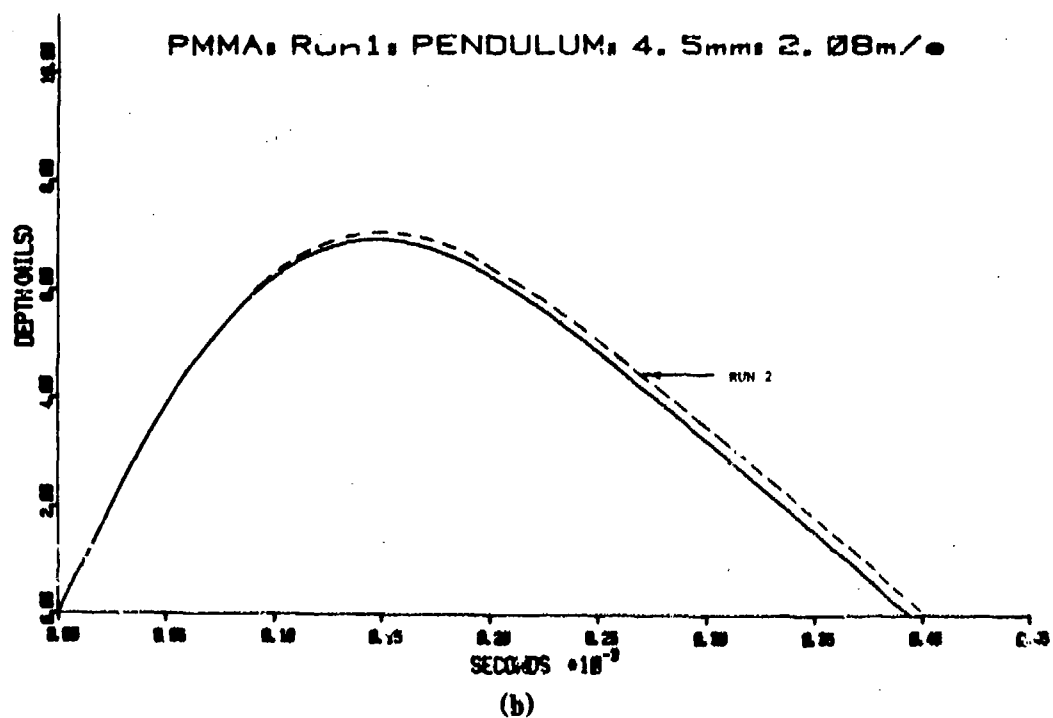
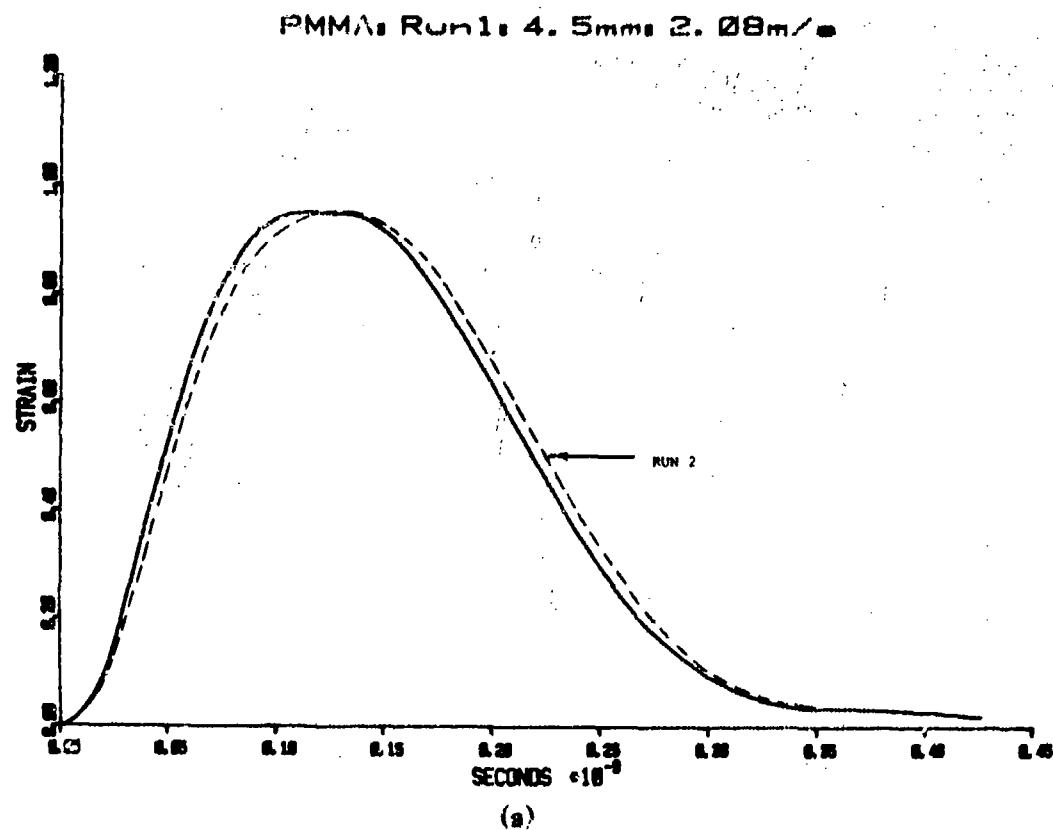


Fig. 6.1A (a) Corrected strain vs time for indicated impact,
(b) penetration depth vs time derived from above pulse.

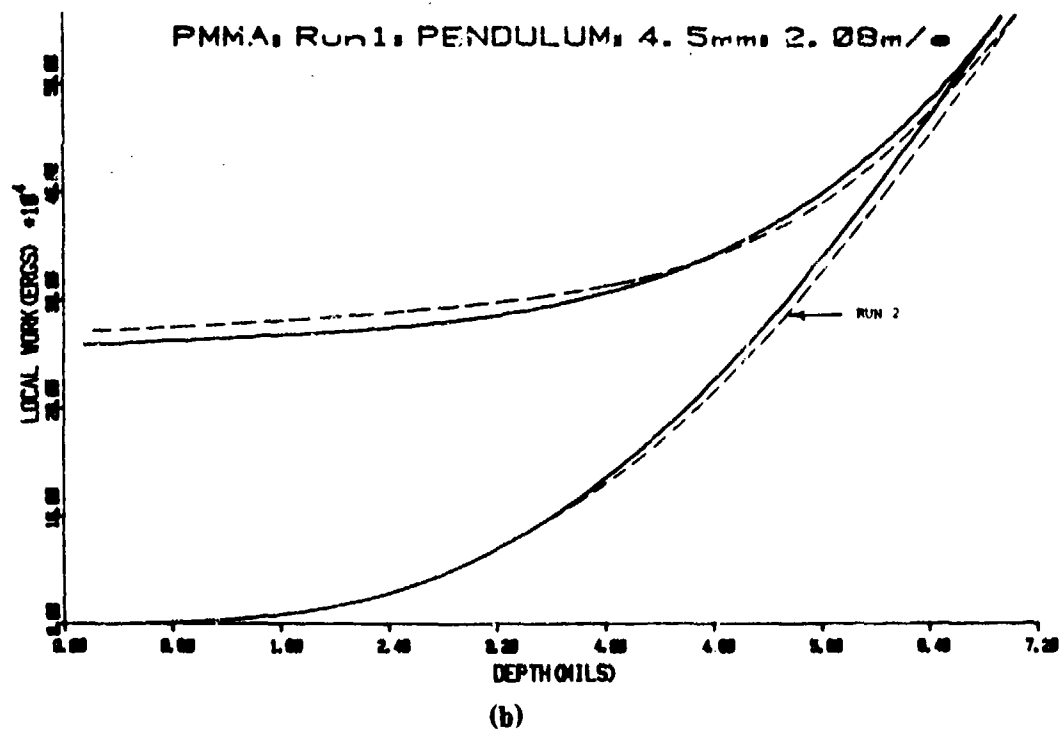
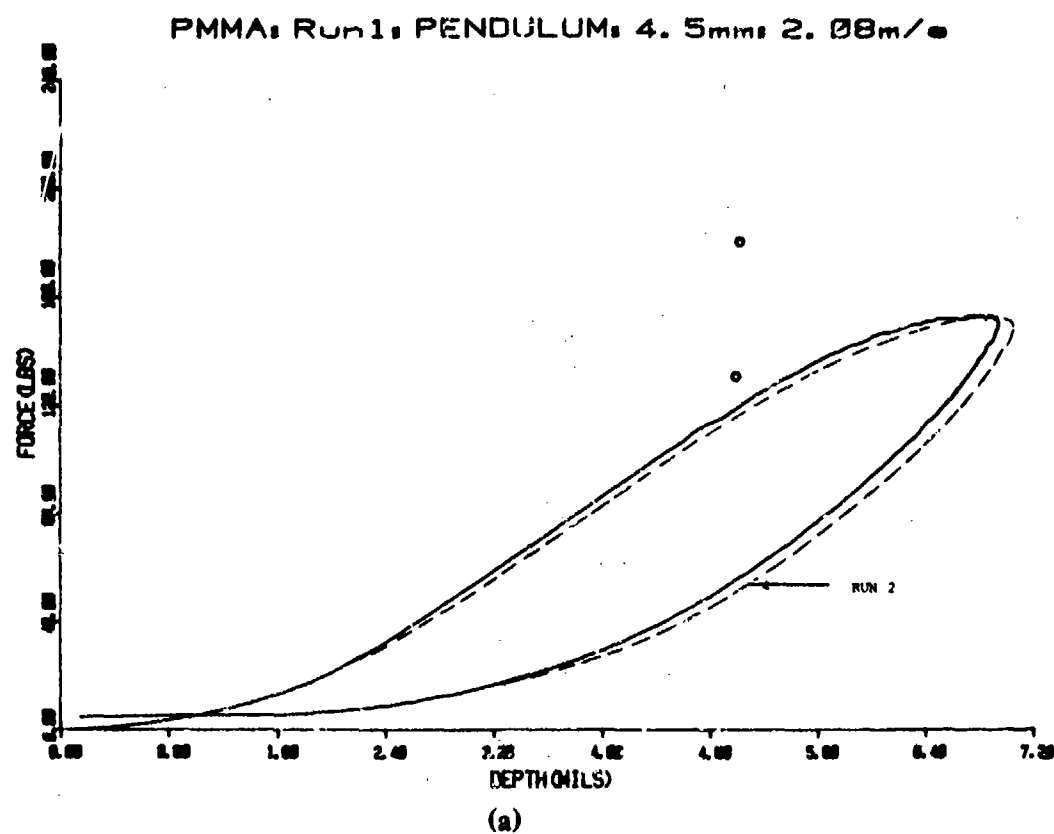
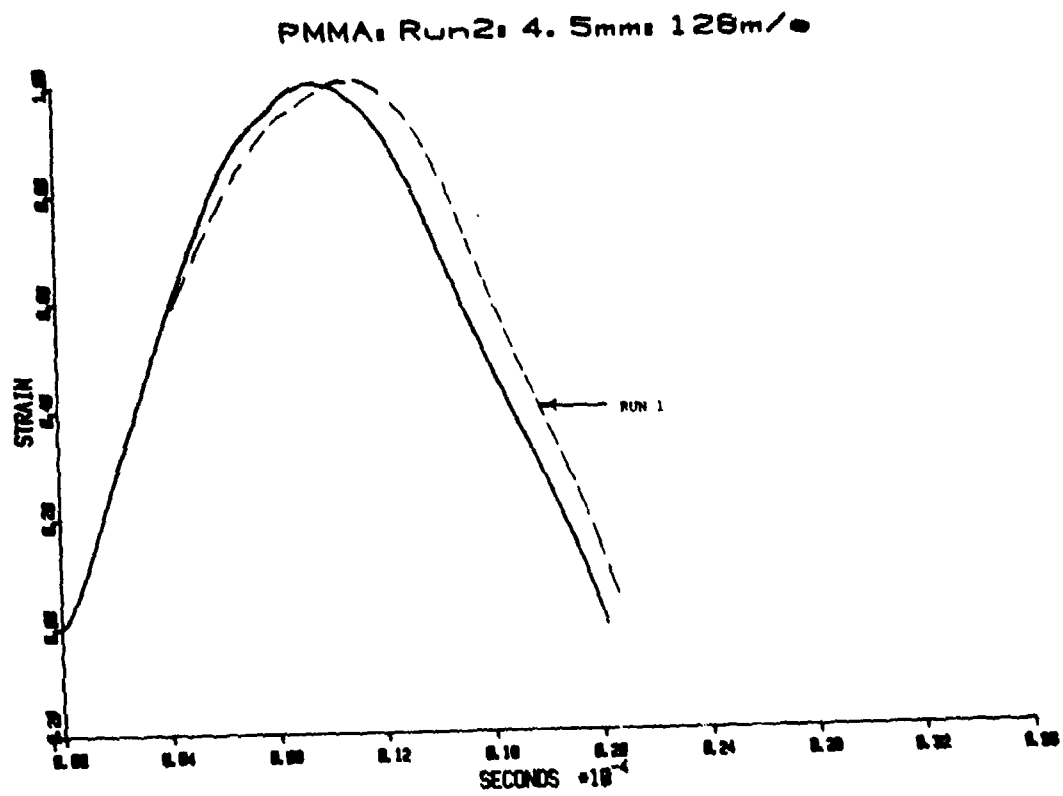
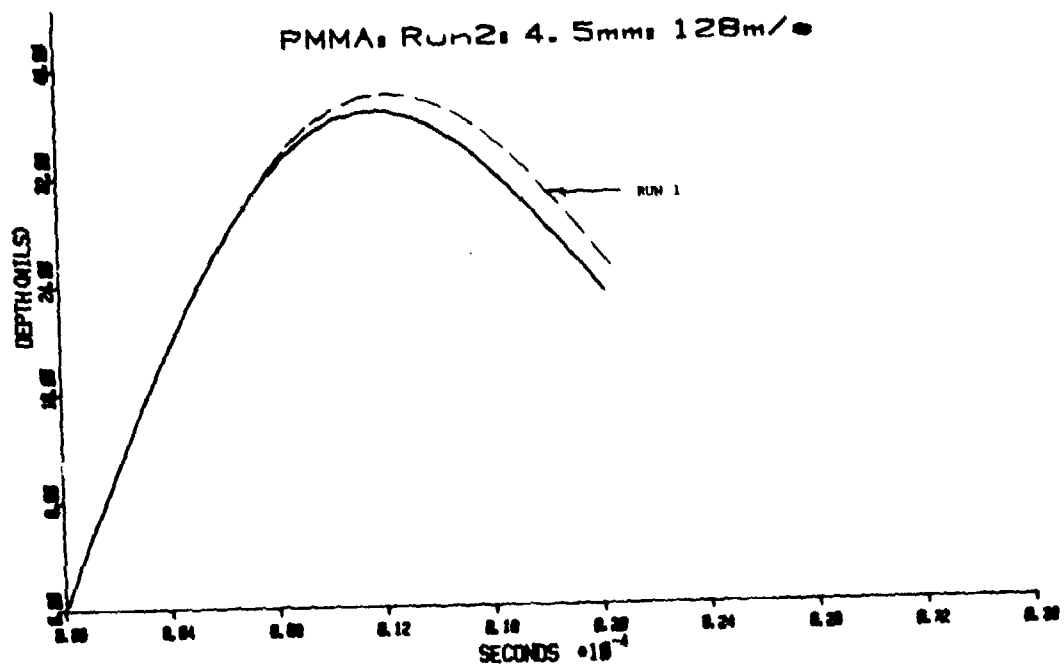


Fig. 6.1B. (a) Force vs depth as derived from preceding corrected pulse,
 (b) local energy absorbed by impact vs depth as derived from preceding
 corrected pulse.

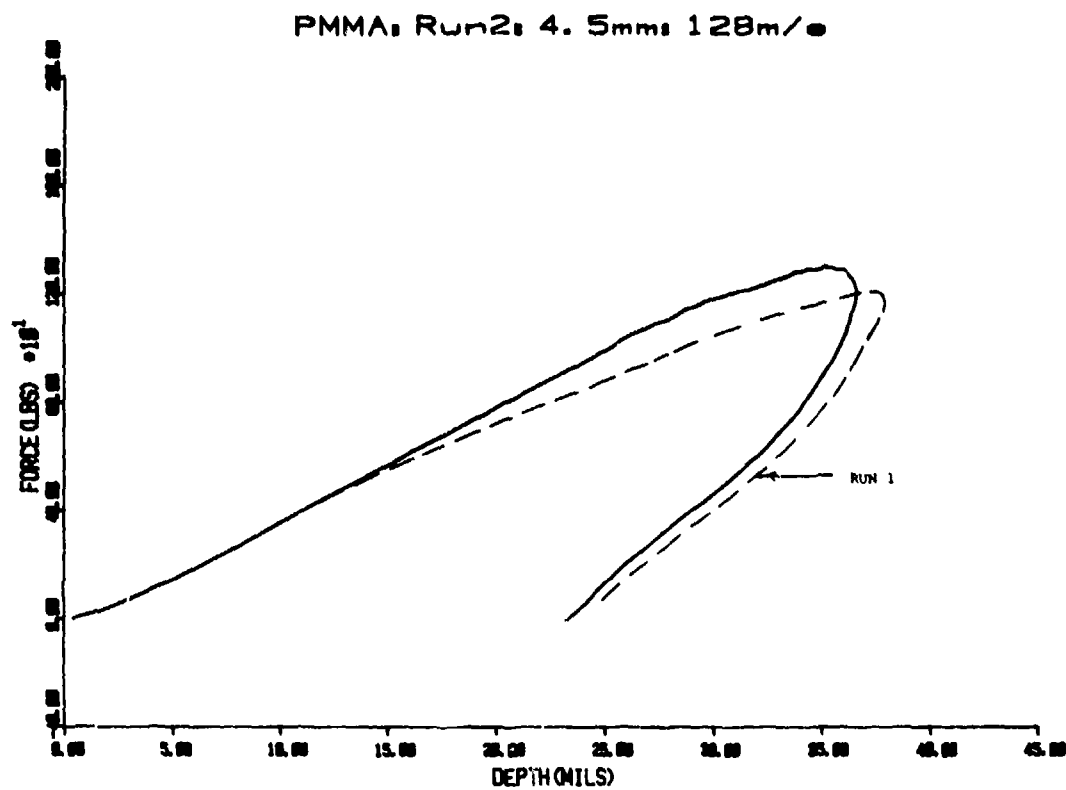


(a)

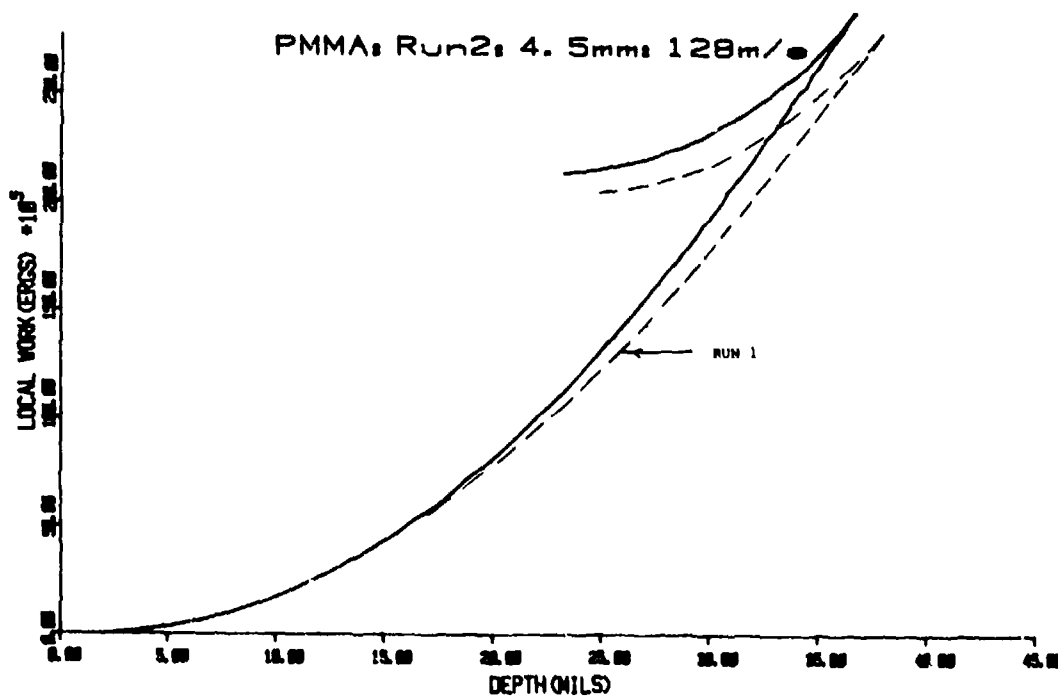


(b)

Fig. 6.1C. (a) Corrected strain vs time for indicated impact,
(b) penetration depth vs time derived from above pulse.

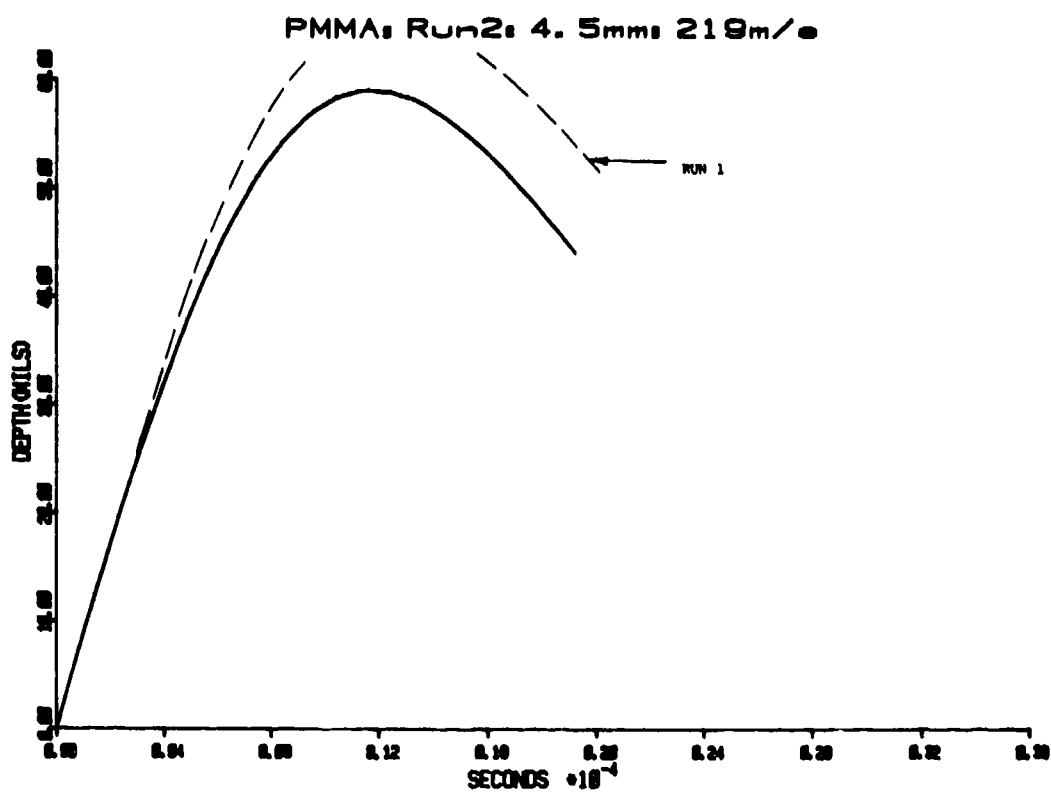


(a)

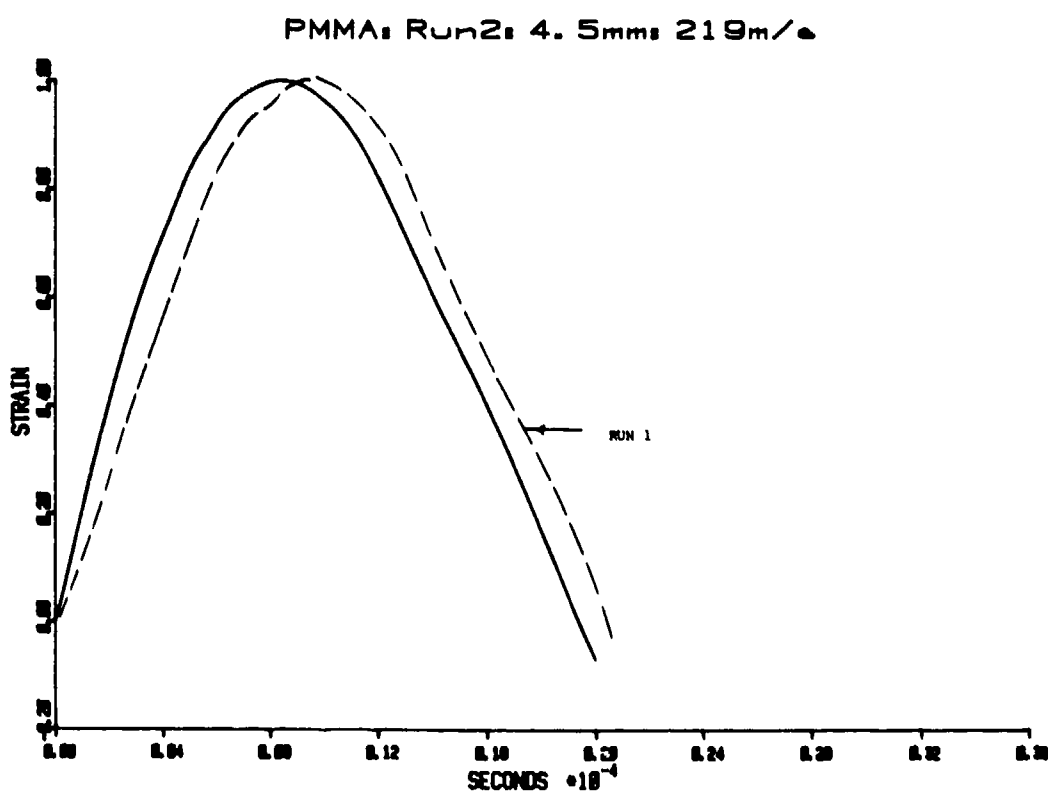


(b)

Fig. 6.1D. (a) Force vs depth as derived from preceding corrected pulse,
(b) local energy absorbed by impact vs depth as derived from preceding corrected pulse.



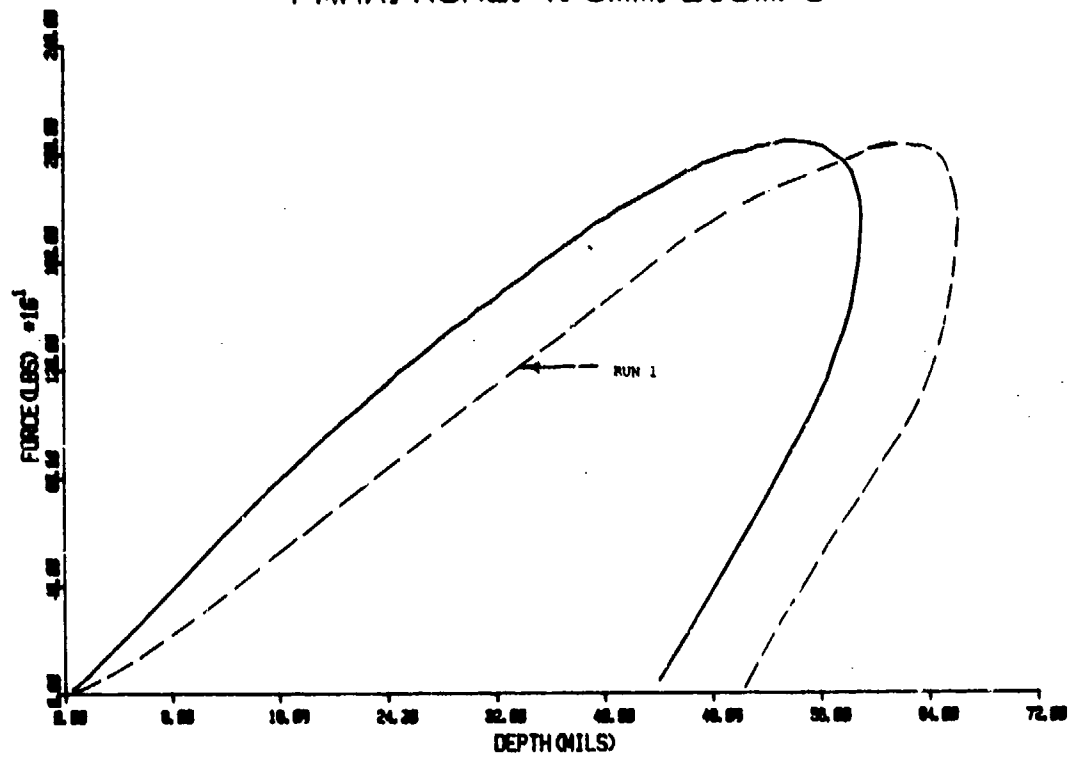
(a)



(b)

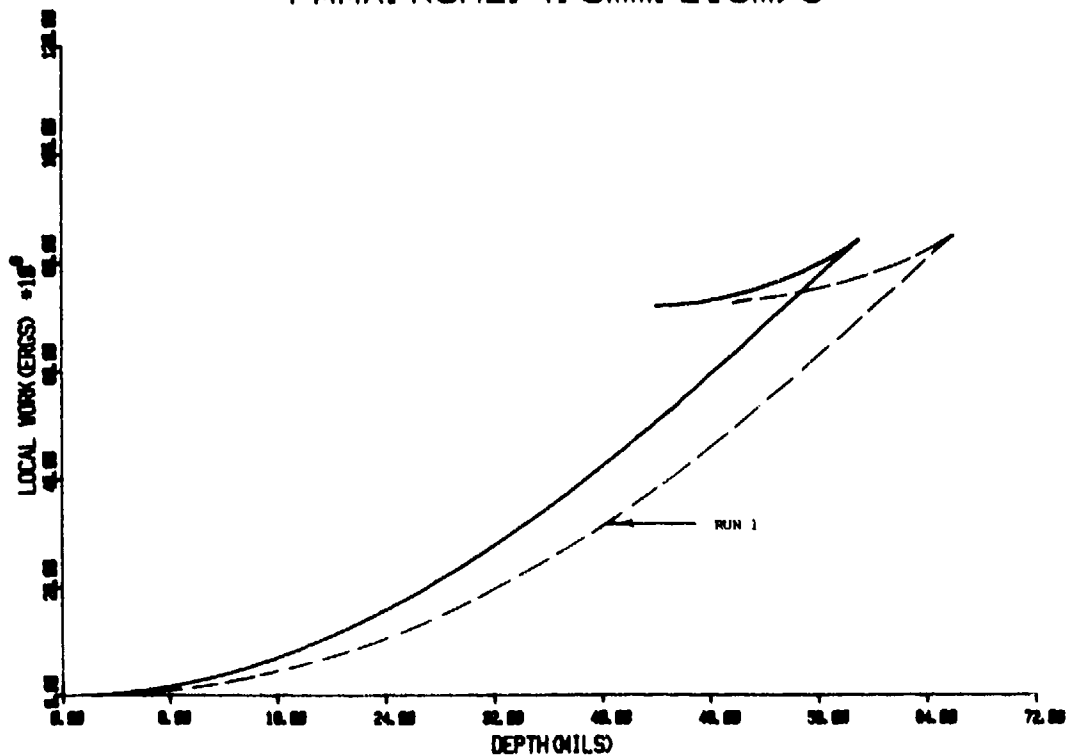
Fig. 6.1E. (a) Corrected strain vs time for indicated impact,
(b) penetration depth vs time derived from above pulse.

PMMA: Run2: 4.5mm: 219m/s



(a)

PMMA: Run2: 4.5mm: 219m/s



(b)

Fig. 6.1F. (a) Force vs depth as derived from preceding corrected pulse,
(b) local energy absorbed by impact vs depth as derived from preceding corrected pulse.

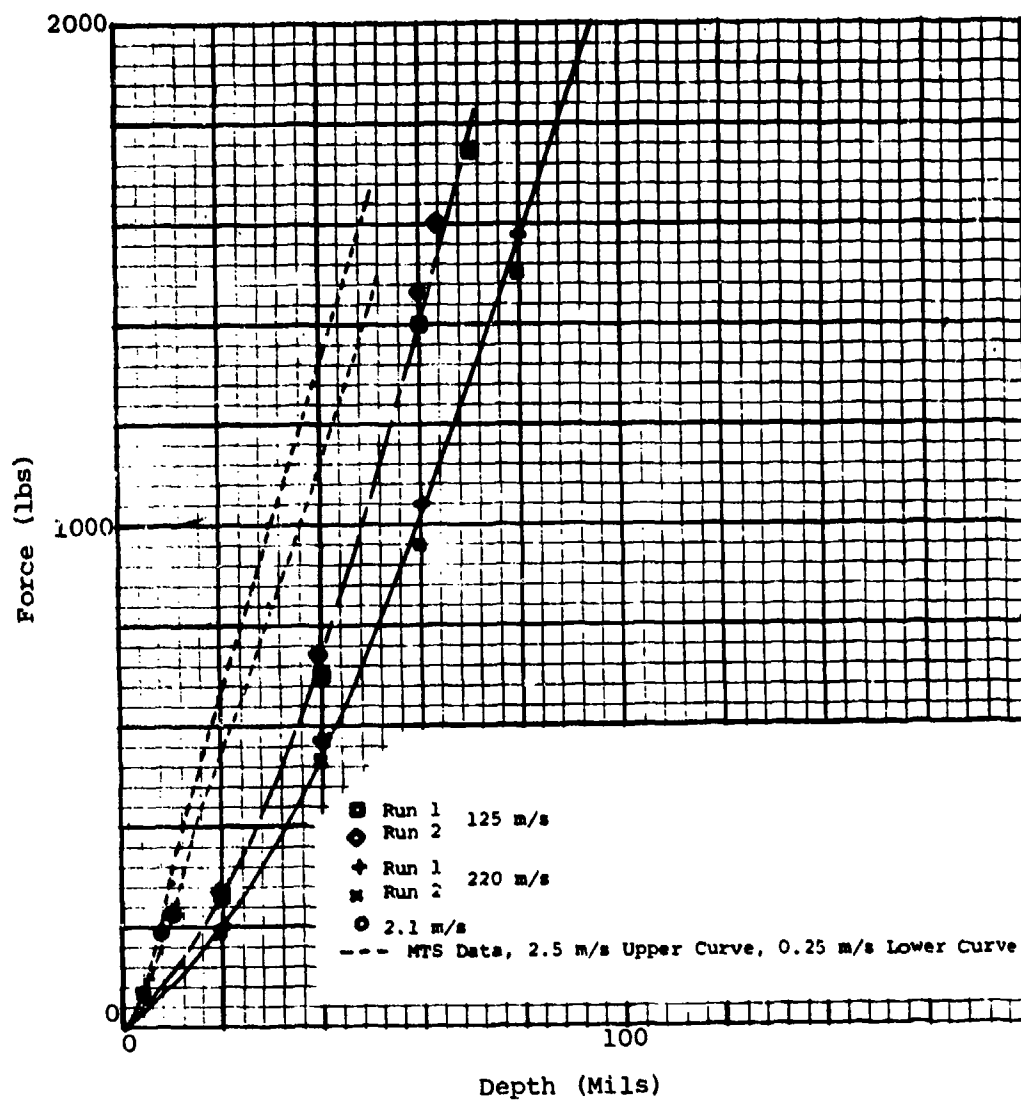


Fig. 6.1G. Force vs penetration depth for PMMA as a function of impact velocity and type of measurement.

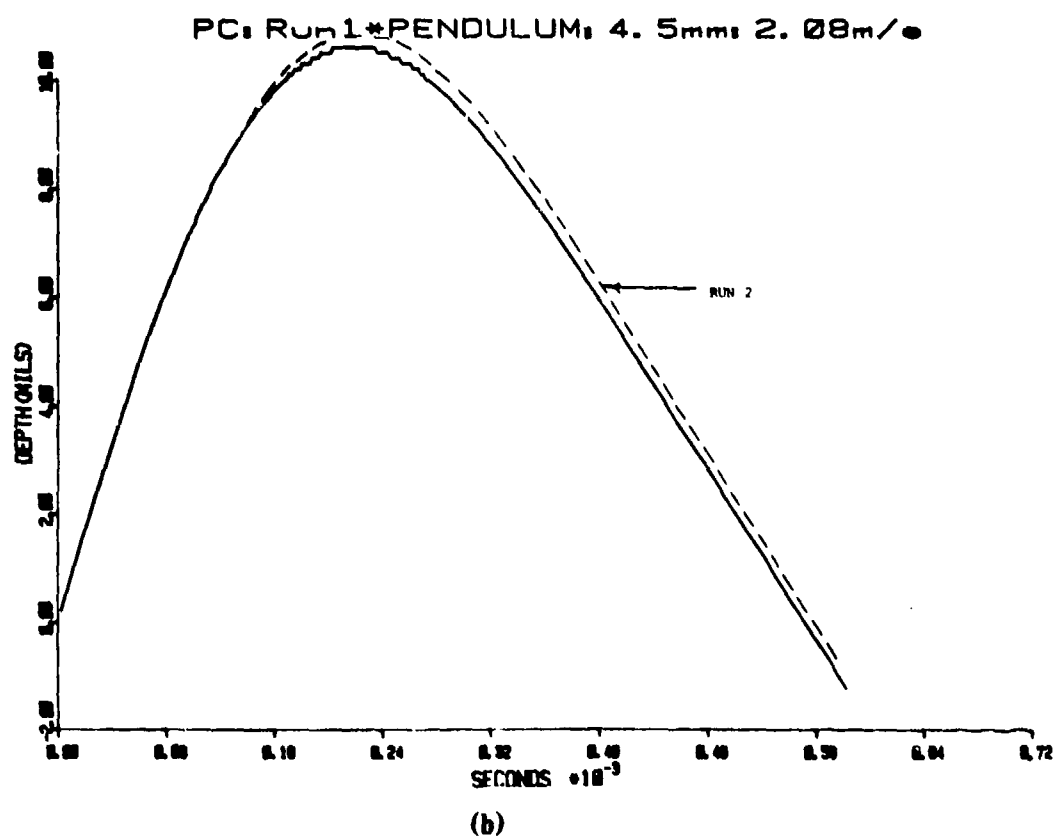
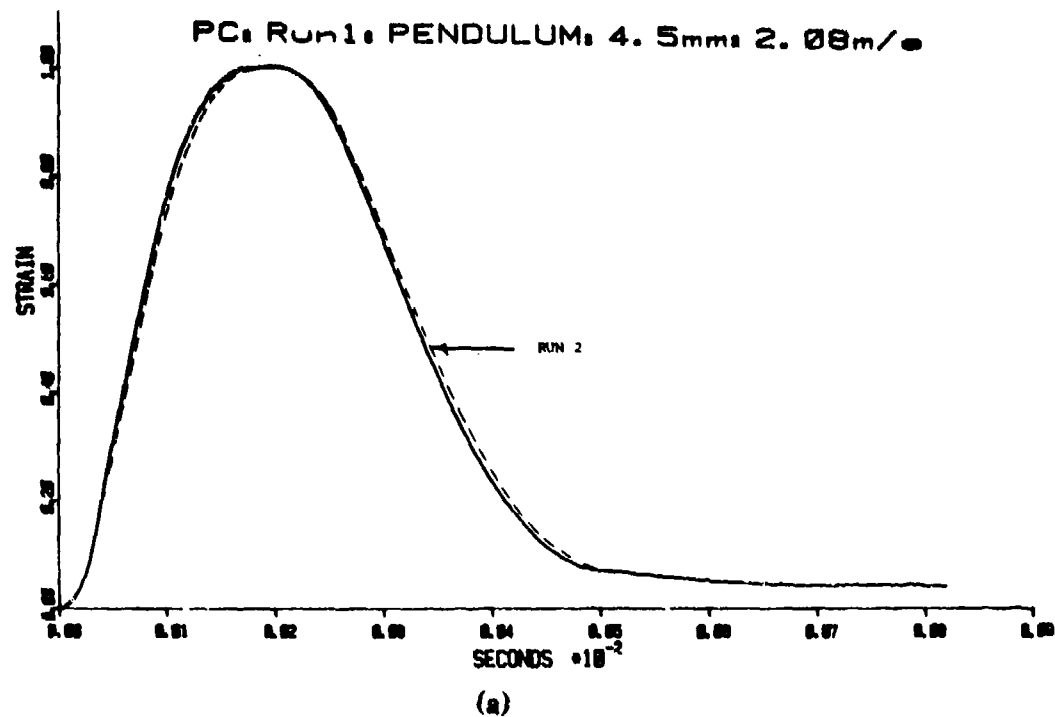
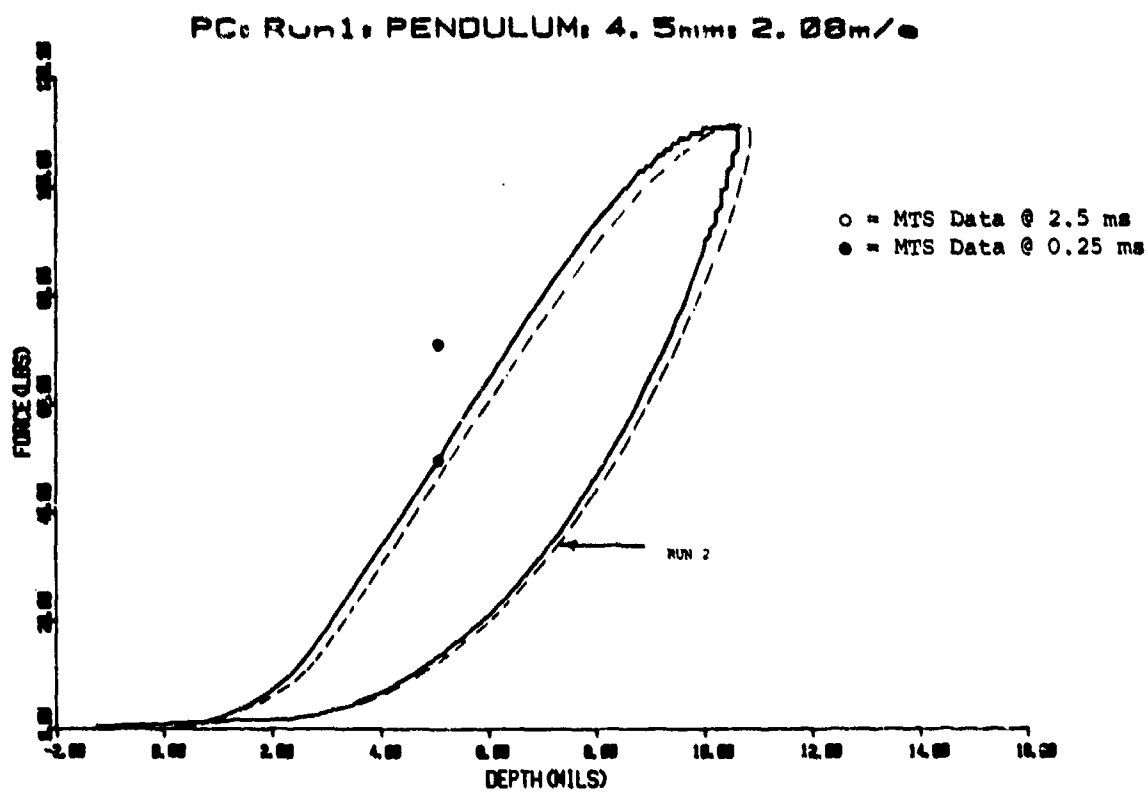
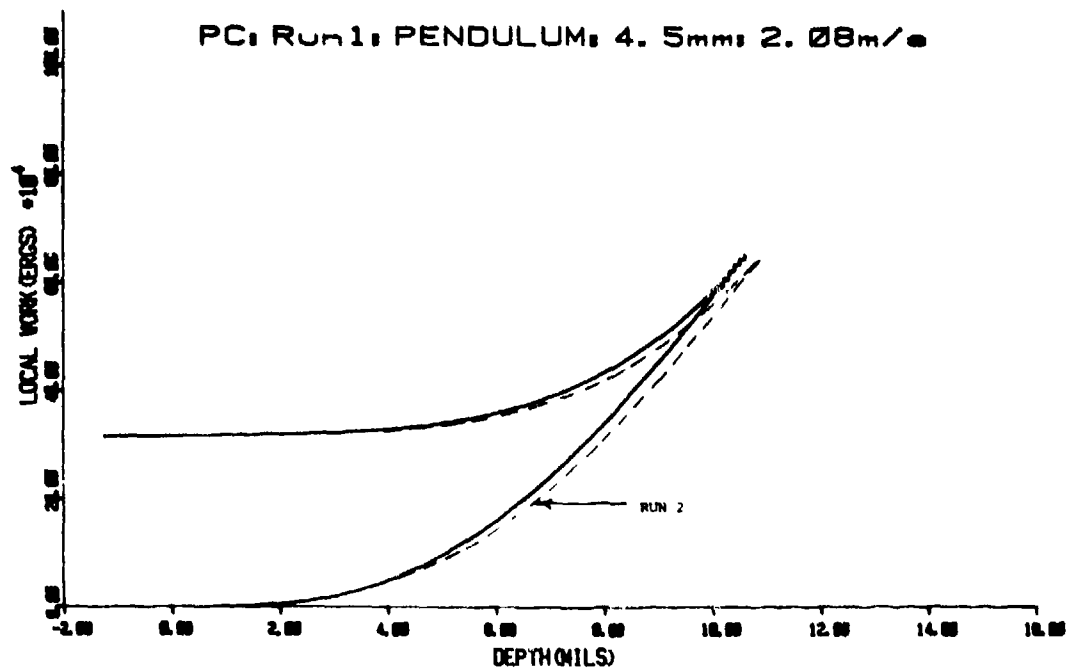


Fig. 6.2A. (a) Corrected strain vs time for indicated impact,
(b) penetration depth vs time derived from above pulse.

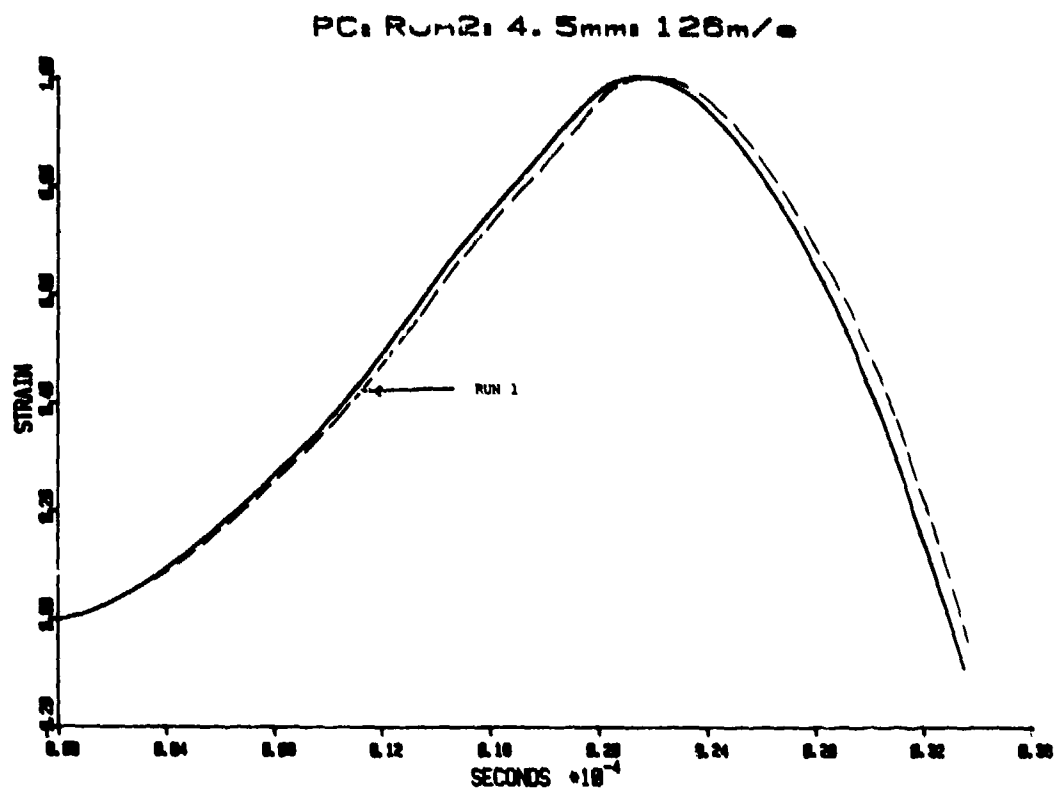


(a)

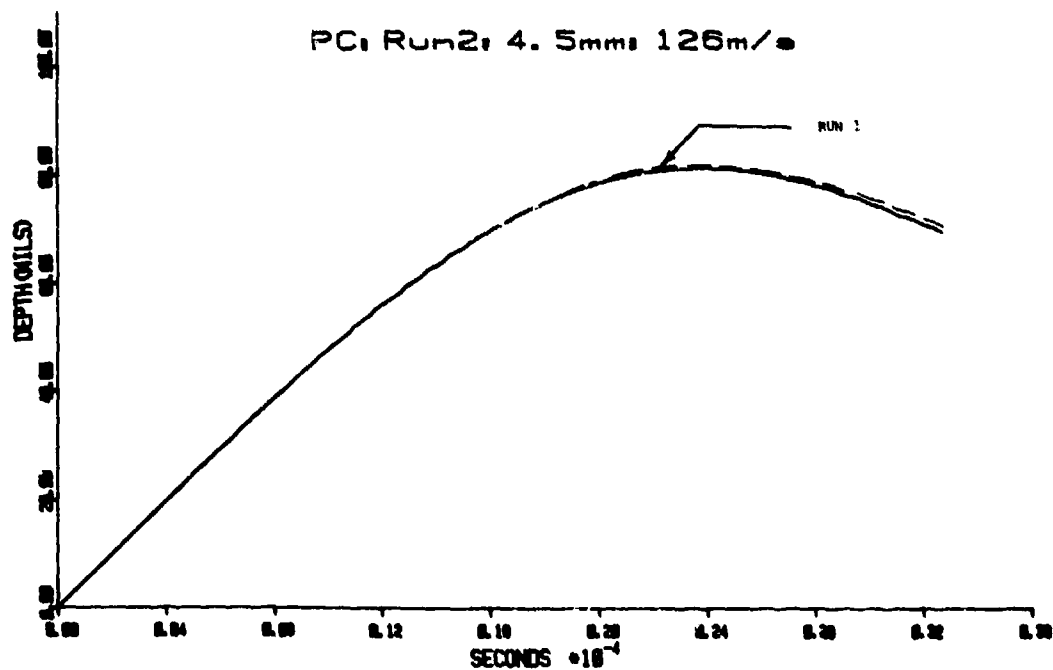


(b)

Fig. 6.2B. (a) Force vs depth as derived from preceding corrected pulse,
(b) local energy absorbed by impact vs depth as derived from preceding corrected pulse.

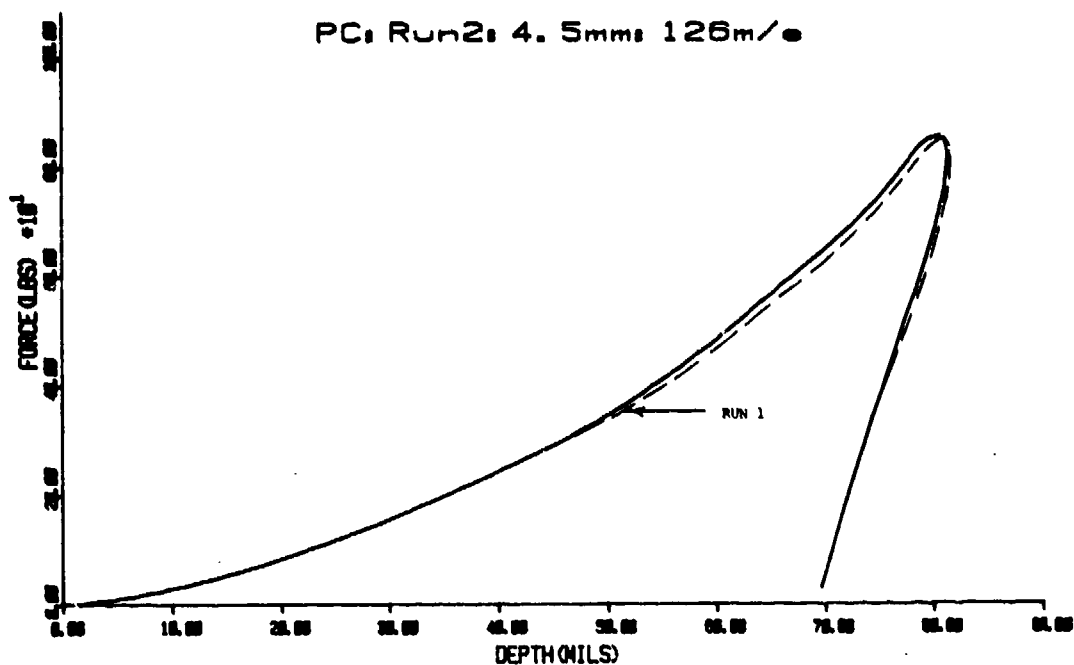


(a)

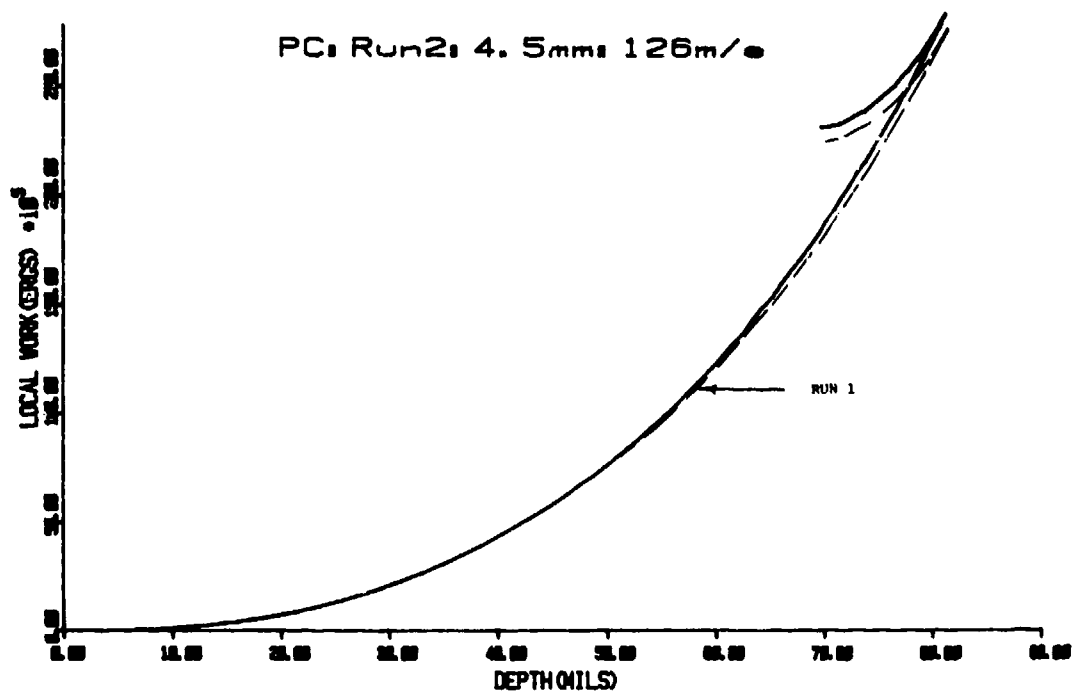


(b)

Fig. 6.2C. (a) Corrected strain vs time for indicated impact,
(b) penetration depth vs time derived from above pulse.

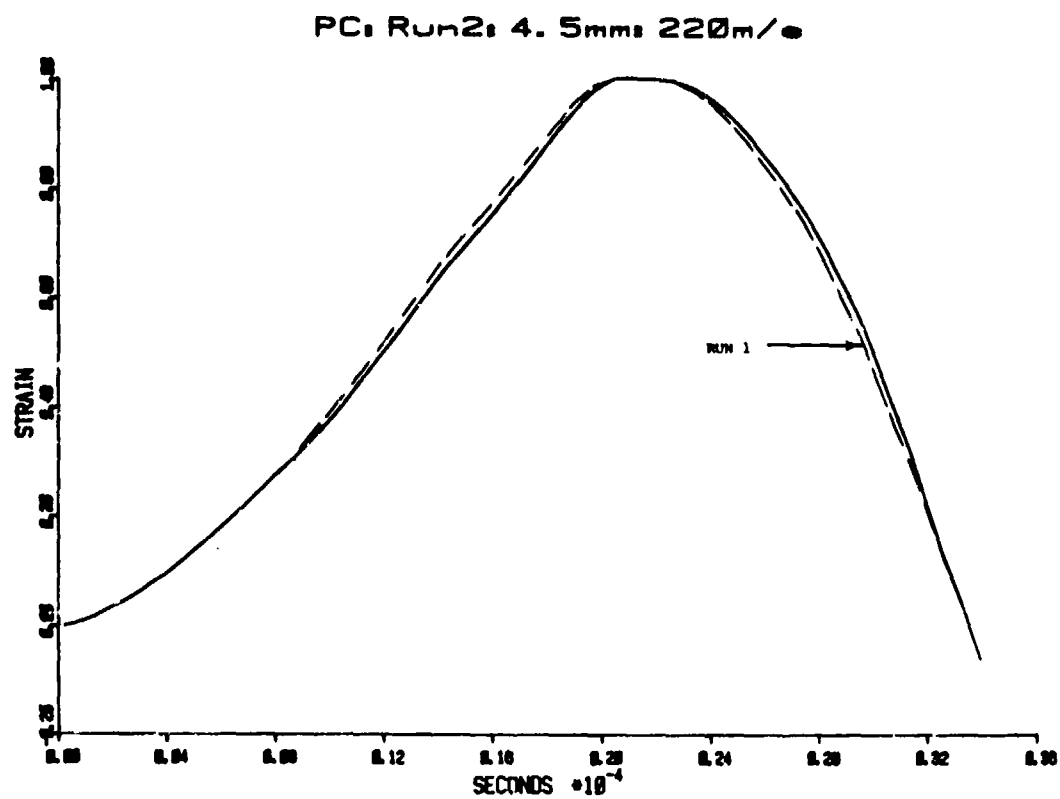


(a)

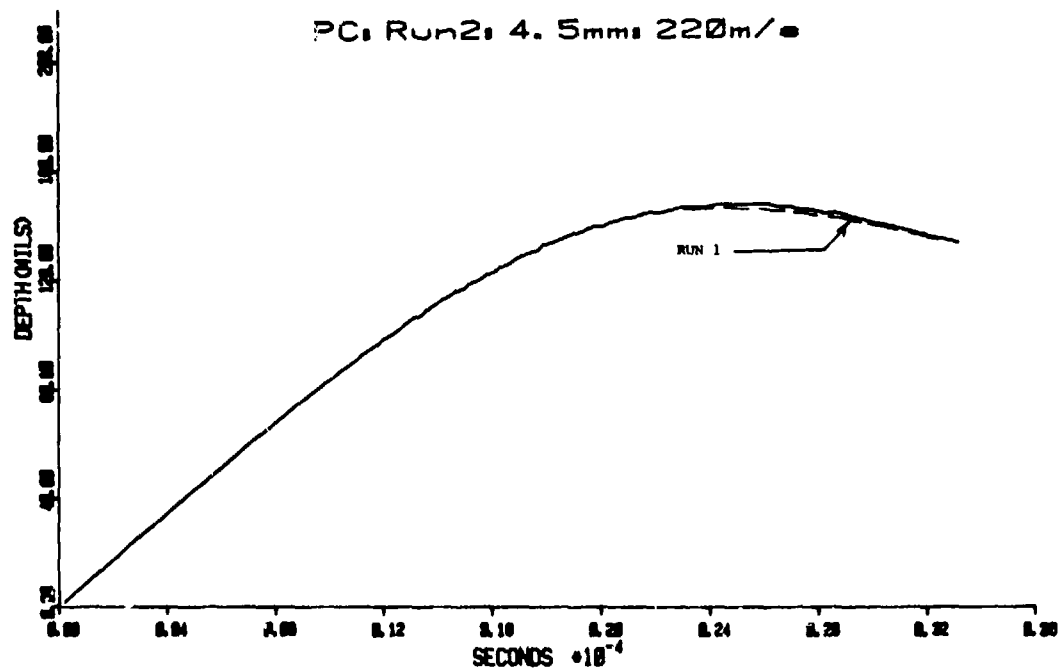


(b)

Fig. 6.2D. (a) Force vs depth as derived from preceding corrected pulse,
(b) local energy absorbed by impact vs depth as derived from preceding corrected pulse.

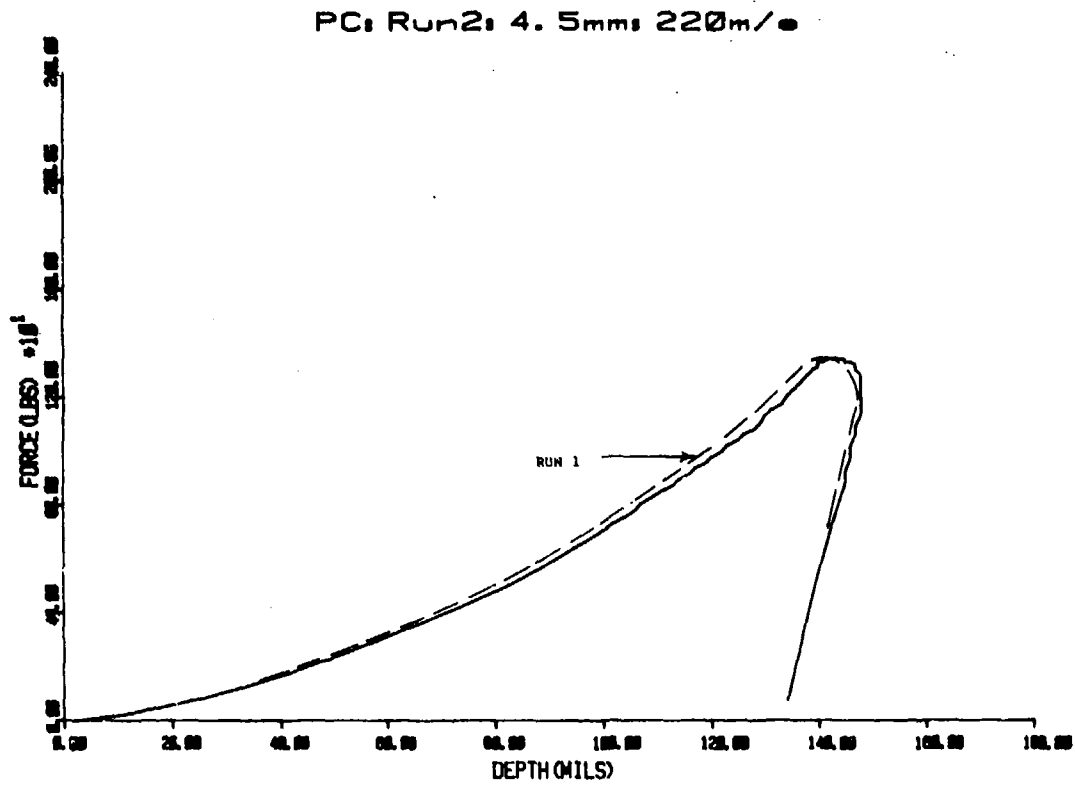


(a)

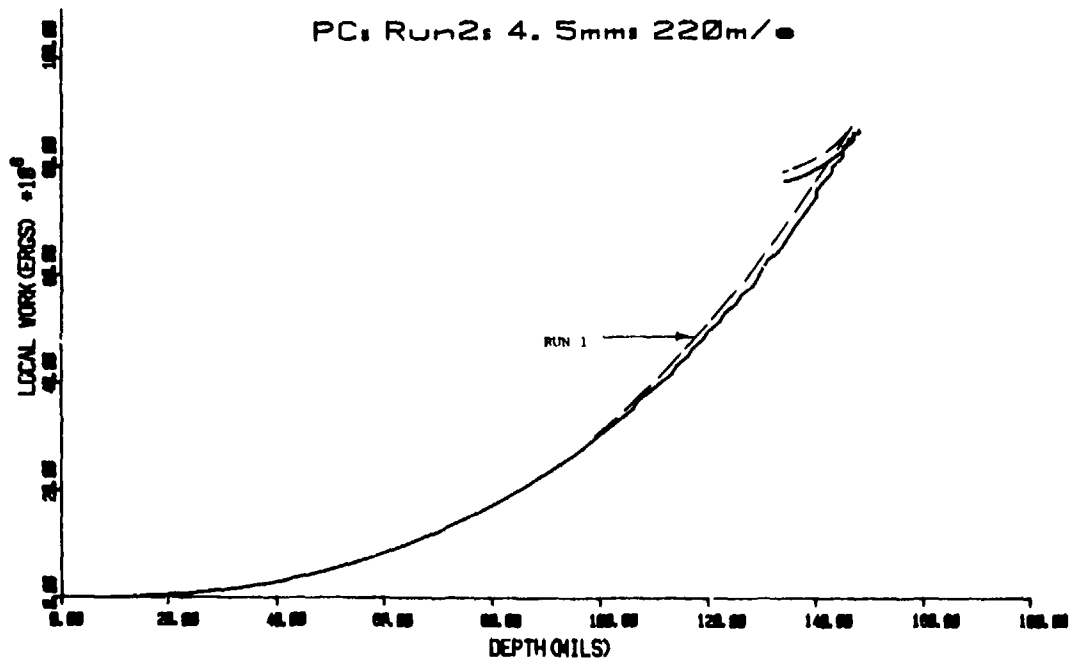


(b)

Fig. 6.2E. (a) Corrected strain vs time for indicated impact,
(b) penetration depth vs time derived from above pulse.



(a)



(b)

Fig. 6.2F. (a) Force vs depth as derived from preceding corrected pulse,
(b) local energy absorbed by impact vs depth as derived from preceding corrected pulse.

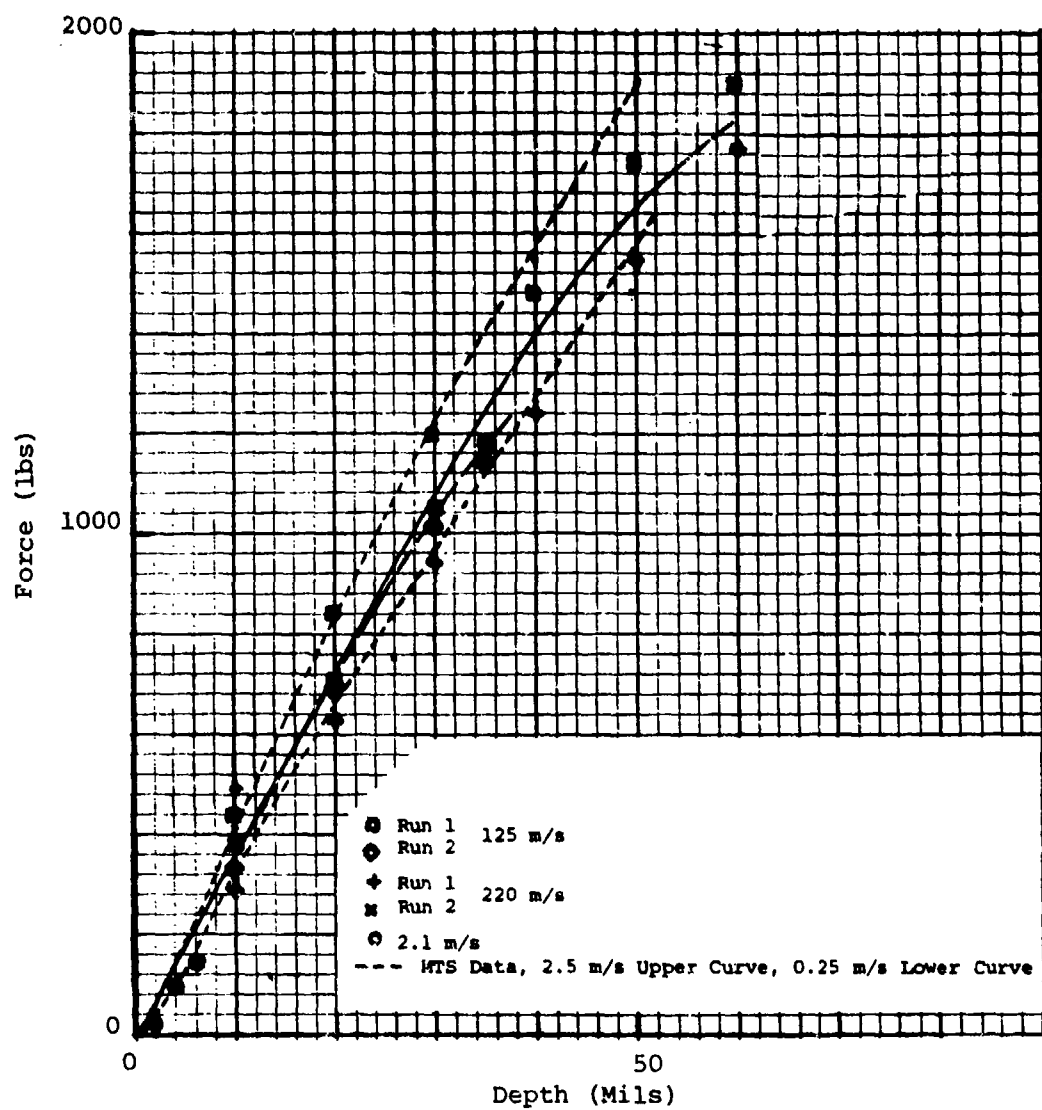


Fig. 6.2G. Force vs penetration depth for PC as a function of impact velocity and type of measurement.

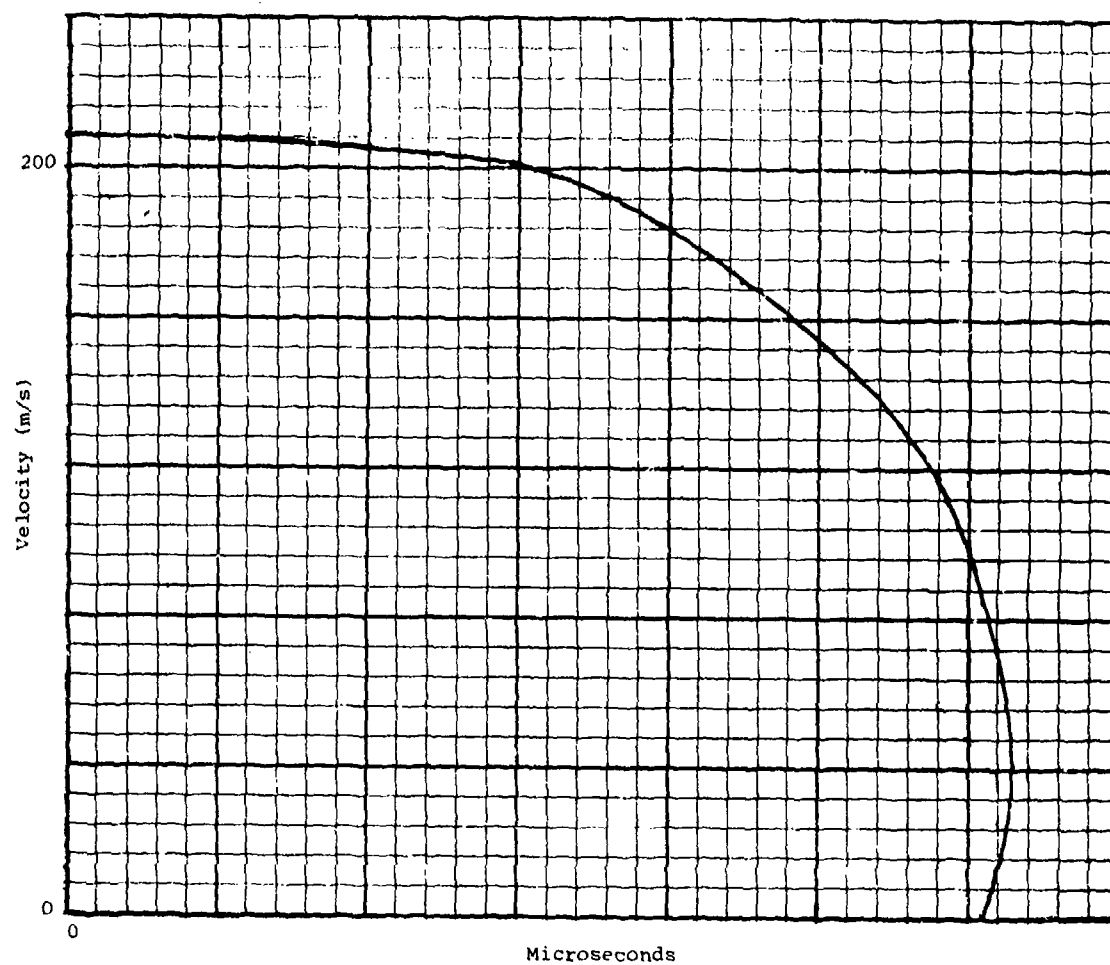


Fig. 6.3A. Penetration velocity vs time for impact of PC specimen by 4.5 mm steel ball at 220 m/s.

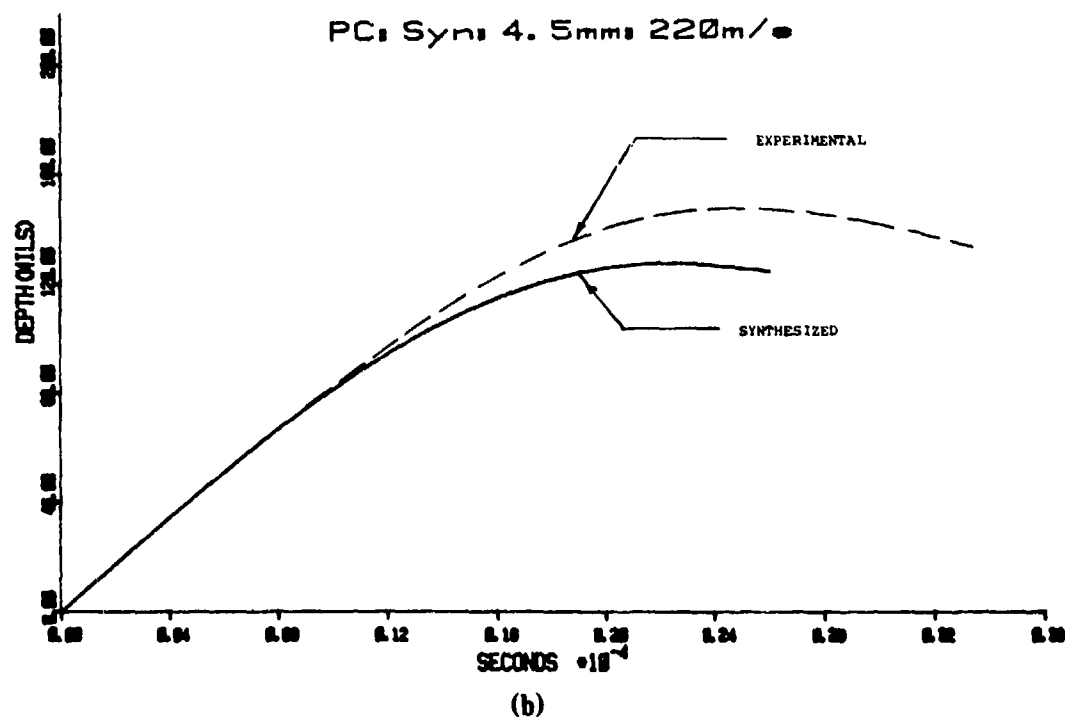
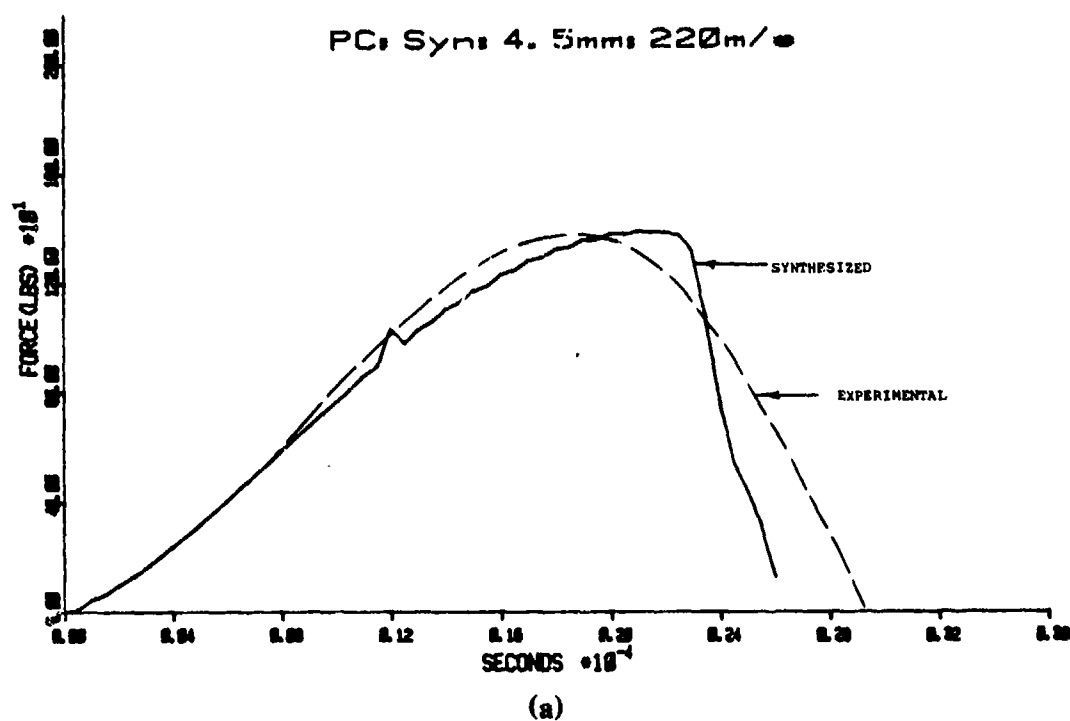
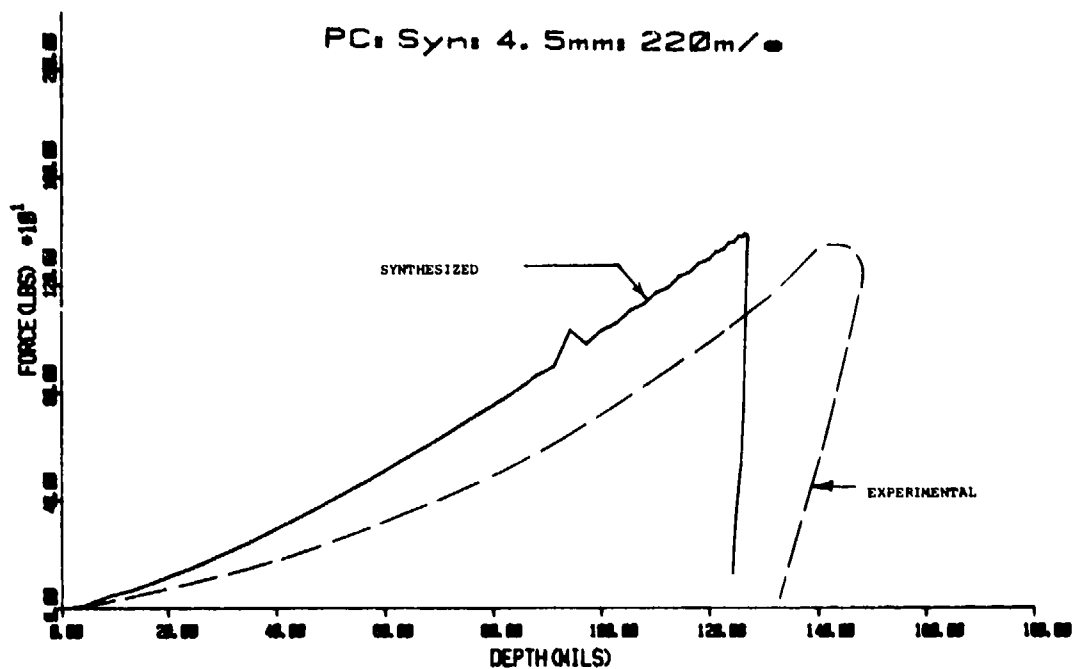
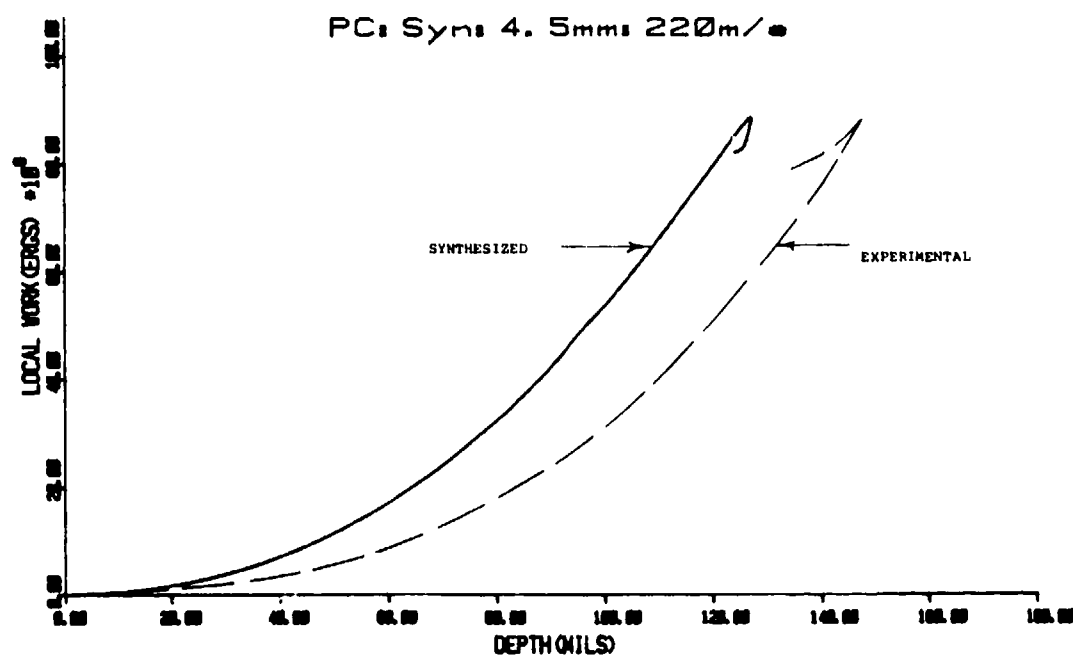


Fig. 7.4A. (a) Comparison of impact pulse synthesized from model with experimental pulse for 220 m/s impact against PC, (b) penetration depth vs time from above pulses.



(a)



(b)

Fig. 7.4B. (a) Force vs depth derived from preceding pulses,
(b) local energy absorbed by impact vs depth as derived from preceding pulses.

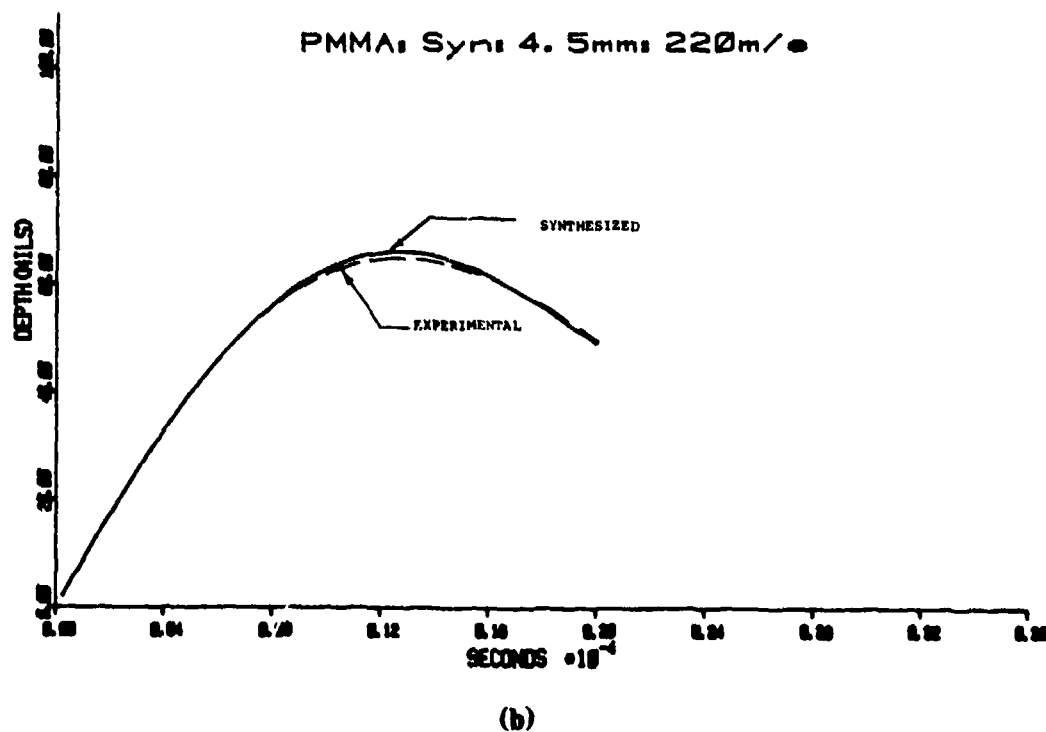
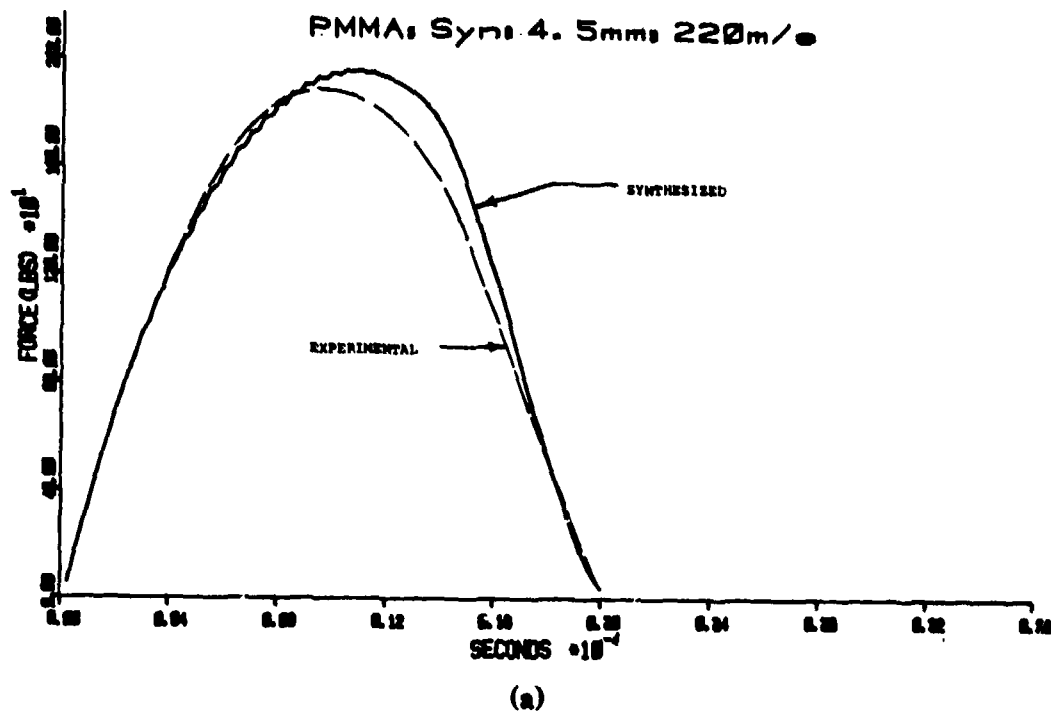
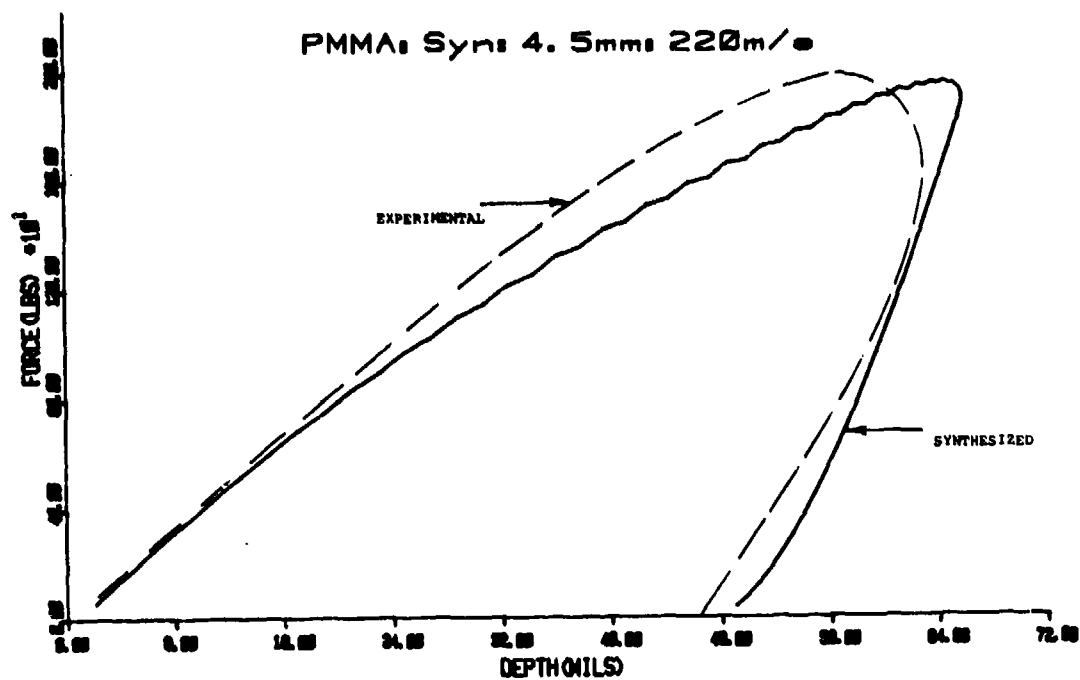
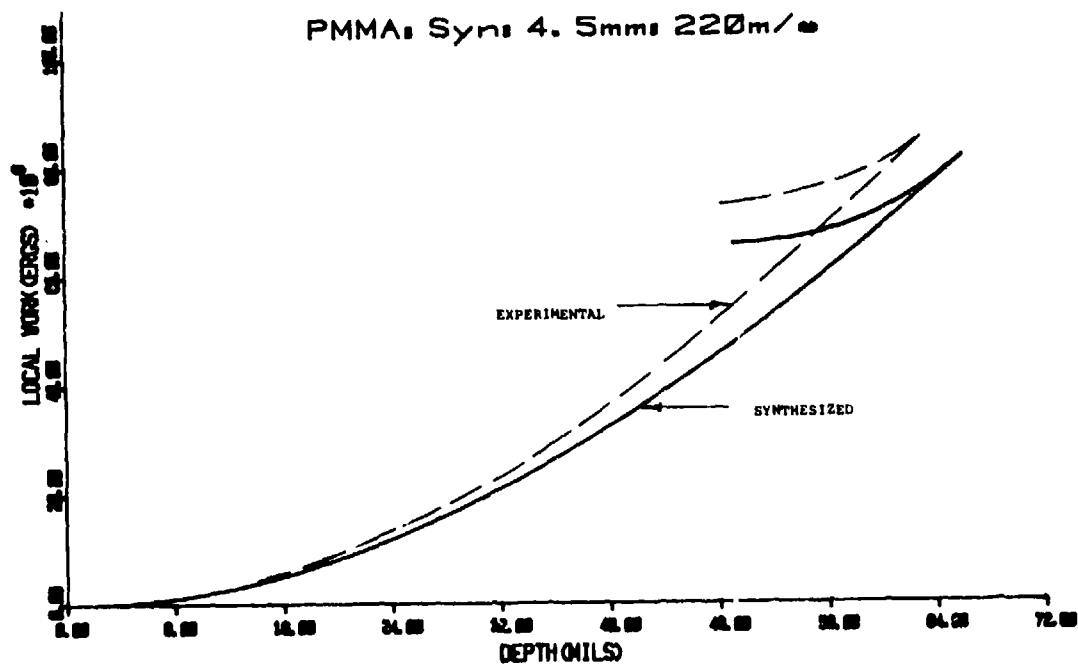


Fig. 7.4C. (a) Comparison of impact pulse synthesized from model with experimental pulse for 220 m/s impact against PMMA, (b) penetration depth vs time from above pulses.



(a)



(b)

Fig. 7.4D. (a) Force vs depth derived from preceding pulses,
(b) local energy absorbed by impact vs depth as derived from preceding pulses.

DISTRIBUTION LIST FOR N00019-79-C-0347

	<u>NO OF COPIES</u>
Commander	17
Naval Air Systems Command	
Washington, DC 20361	
Attention: AIR-00D4	11
AIR-320A	1
AIR-5163D4	5
Office of Naval Research	3
800 N. Quincy Street	
Arlington, VA 22217	
Attention: Code 471	1
Code 472	1
Code 473	1
Commander	1
Naval Surface Weapons Center	
White Oak	
Silver Spring, MD 20910	
Attention: Code R31	
Director	2
Naval Research Laboratory	
Washington, DC 20375	
Attention: Code 6360	1
Code 8433	1
Commanding Officer	1
David W. Taylor Naval Ship Research & Development Center	
Annapolis, MD 21412	
Attention: W. Smith, Code 2832	
Commander	1
Naval Ocean Systems Center	
San Diego, CA 92152	
Attention: Dr. J. Stachiw, Code-5204(B)	
Commander	1
Naval Air Development Center	
Warminster, PA 18974	
Attention: Code 606	
Officer in Charge of Construction	1
Civil Engineering Laboratory	
Naval Facility Engineering Command Detachment	
Naval Construction Battalion Center	
Port Hueneme, CA 93043	
Attention: Stan Black, Code L40	

	<u>NO OF COPIES</u>
Commander Air Force Wright Aeronautical Laboratories Wright-Patterson Air Force Base Dayton, OH 45433 Attention: S. Marolo MLSE 1 R. Speelman FIEA 1 T. Reinhart MLBC 1	3
Brookhaven National Laboratory Upton, NY 11973 Attention: Dr. D. Van Rooyen	1
Director Applied Technology Laboratory US Army Research & Technology Laboratories Fort Eustis, VA 23604 Attention: DAVDL-ATL-ATP (Mr. Pauze)	1
US Army Research Office Box CM, Duke Station Durham, NC 27706 Attention: CRCARD	1
US Army MERDC Fort Belvoir, VA 22060 Attention: SMEFB-EP (W. McGovern)	1
Army Materials and Mechanics Research Center Watertown, MA 02172 Attention: Dr. R. N. Katz 1 Dr. G. Thomas 1	2
US Army Armament Research & Development Command Plastics Technical Evaluation Center Dover, NJ 07801	1
NASA Headquarters Washington, DC 20546 Attention: C. F. Bersch, RTM-6	1
NASA Lewis Research Center 21000 Brookpark Road Cleveland, OH 44135 Attention: Dr. E. Zaretsky 1 W. A. Sanders (49-1) 1 and Dr. T. Hergel 1	2
Defense Advanced Research Project Office 1400 Wilson Blvd Arlington, VA 22209 Attention: Dr. Van Reuth	1

	<u>NO OF COPIES</u>
Inorganic Materials Division Institute for Materials Research National Bureau of Standard Washington, DC 20234	1
Department of Engineering University of California Los Angeles, CA 90024 Attention: Profs. J. W. Knapp and G. Sines	1
University of Dayton Library on Materials Research 300 College Park Avenue Dayton, OH 45409	1
Engineering Experiment Station Georgia Institute of Technology Atlanta, GA 30322 Attention: J. D. Walton	1
University of Illinois Urbana, IL 61801 Attention: Prof. H. T. Corten Department of Theoretical & Applied Mechanics	1
Department of Engineering Research North Carolina State University Raleigh, NC 27607 Attention: Dr. H. Palmour	1
Ceramic Science and Engineering Section Pennsylvania State University University Park, PA 16802 Attention: Dr. R. E. Tressler	1
Rensselaer Polytechnic Institute 110 Eighth Street Troy, NY 12181 Attention: Dr. S. S. Sternstein 1 Prof. R. Doremus 1	2
School of Ceramics Rutgers, The State University New Brunswick, NJ 08903	1
Virginia Polytechnic Institute Minerals Engineering Blacksburg, VA 20460 Attention: Dr. D. P. H. Hasselman	1

	<u>NO OF COPIES</u>
Advanced Mechanical Technology Inc. 141 California Street Newton, MA 02158 Attention: Dr. Walter D. Syniuta	1
Aerospace Corporation Materials Laboratory P. O. Box 95085 Los Angeles, CA 90045	1
Materials Development Center AVCO Systems Division Wilmington, MA 01887 Attention: Tom Vasilos	1
Lycoming Division AVCO Corporation Stratford, CT 06497 Attention: Mr. D. Wilson	1
Batelle Memorial Institute 505 King Avenue Columbus, OH 43201 Attention: Ceramics Department 1 Metal & Ceramic Information Center 1	2
Bell Helicopter Textron P. O. Box 482 Fort Worth, TX 76101 Attention: R. Battles	1
The Boeing Company Materials and Processes Laboratory Aerospace Group P. O. Box 3999 Seattle, WA 98124 Attention: J. VanWyk	1
Research and Development Division Carborundum Company Niagra Falls, NY 14302 Attention: Mr. C. McMurty	1
Ceramic Finishing Company Box 498 State College, PA 16801	1
Ceradyne Inc. Box 1103 Santa Ana, CA 92705	1

	<u>NO OF COPIES</u>
Coors Porcelain Company 600 Ninth Street Golden, CO 80401 Attention: Research Department	1
Dow Chemical Company Polymer Research Laboratory Midland, MI 48640	1
E. I. duPont deNemours & Company Plastics Department Wilmington, DE 19898	1
Fiber Materials, Inc. Biddeford Industrial Park Biddeford, ME 04005 Attention: Dr. H. Dean Batha	1
Product Development Group Ford Motor Company 20000 Rotunda Drive Dearborn, MI 28121 Attention: Mr. E. Fisher	1
Space Sciences Laboratory General Electric Company P. O. Box 8555 Philadelphia, PA 19101	1
NDH Division General Motors Corporation Hayes Street Subdusky, OH 44870 Attention: M. Woerhle	1
Goodyear Aerospace Corporation Litchfield Park, AZ 85340 Attention: Blenn E. Wintermute	1
Grumman Aerospace Corporation Bethpage, NY 11714 Attention: Dennis S. Riddle Structural Design, Engineering Department	1
Hughes Aircraft Company Culver City, CA 90230 Attention: M. N. Gardos	1
IIT Research Institute 10 West 35th Street Chicago, IL 60616 Attention: Ceramics Division	1

NO OF COPIES

Industrial Tectonics, Inc.
18301 Santa Fe Avenue
Compton, CA 90224
Attention: Hans R. Signer

1

Kaweki-Berylco Industry
Box 1462
Reading, PA 19603
Attention: Mr. R. J. Longnecker

1

Research and Development Division
Arthur D. Little Company
Acorn Park
Cambridge, MA 02140

1

Lockheed-California Company
Burbank, CA 91503
Attention: Jarvis Fargo

1

McDonnell Douglas Corporation
Douglas Aircraft Company
3855 Lakewood Blvd
Long Beach, CA 90846
Attention: Joe Kozmato 1
 Jim Lawrence 1

2

McDonnell Douglas Corporation
McDonnell Aircraft Company
P. O. Box 615
St. Louis, MO 63166
Attention: Ramsey Lammers III

1

Material Sciences Corporation
17777 Walton Road
Blue Bell, PA 19422

1

Mechanical Technology, Inc.
968 Albany-Shaker Road
Latham, NY 12110
Attention: Dr. E. F. Finkin

1

Norton Company
Industrial Ceramics Division
One New Bond Street
Worcester, MA 01606
Attention: Dr. M. Torti

1

North American Rockwell Science Center
P. O. Box 1085
Thousand Oaks, CA 91360

1

NO OF COPIES

PPG Industries, Inc. Central Bank Bldg Suite 771 Huntsville, AL 35801 Attention: Thomas Clark	1
PPG Industries, Inc. P. O. Box 11472 Pittsburgh, PA 15238 Attention: Jamers E. Mahaffey	1
Ceramic Division Sandia Corporation Albuquerque, NM 87101	1
Sierracin/Sylmar 12780 San Fernando Road Sylmar, CA 91342 Attention: David L. Voss	1
SKF Technology Services SKF Industries Inc. 1100 First Street P. O. Box 515 King Of Prussia, PA 19406 Attention: P. A. Madden	1
Solar Turbines International P. O. Box 80966 San Diego, CA 92138 Attention: G. W. Hosang	1
Southwest Research Institute P. O. Drawer 28510 San Antonio, TX 78228	1
Materials Sciences & Engineering Laboratory Stanford Research Institute Menlo Park, CA 94025 Attention: Dr. Cubiciotti	1
Swedlow, Inc. 12122 Western Avenue Garden Grove, CA 92645 Attention: N. G. Nixon	1
Union Carbide Corporation Parma Technical Center P. O. Box 6116 Cleveland, OH 44101	1

NO OF COPIES

Materials Sciences Laboratory
United Technologies
East Hartford, CT 06101
Attention: Dr. J. J. Brennan

1

United Technologies Research Center
East Hartford, CT 06108
Attention: F. L. Ver Snyder

1

Vought Corporation
P. O. Box 5901
Dallas, TX 75222
Attention: A. E. Hohman, Jr.

1

Astronuclear Laboratory
Westinghouse Electric Corporation
Box 10864
Pittsburgh, PA 15236

1

Westinghouse Research Laboratories
1310 Beulah Road
Churchill Borough
Pittsburgh, PA 15235
Attention: Dr. R. Bratton

1